

Fluorescence and Lasing in Dye-doped and Conjugated Polymer Microspheres

by

Kirsty Ann Gardner

A thesis submitted in partial fulfillment of the requirements for the degree
of

Doctor of Philosophy

Department of Physics

University of Alberta

© Kirsty Ann Gardner, 2020

Abstract

This thesis explores the optical and microstructural properties of fluorescent and lasing polymer microspheres, as well as methods for their fabrication and size control. I investigate the fluorescent and lasing behaviour of polymer-coated glass microspheres by a combination of evanescent coupling, and fluorescence and lasing measurements. Coated glass microspheres lack perfect spherical symmetry and have a dense forest of resonances such that lasing preferentially occurs where these modes are most densely spaced within the gain band of the lasing medium. Next, I discuss the benefits of conjugated polymers (CPs) over dye-doped polymers before demonstrating a fabrication method which produces large CP microspheres (up to 50 times larger than those produced by other methods) and which are 20 times brighter than conventional dye-doped microspheres. Finally I develop a simple microfluidics fabrication method which enables good size control, from which arrays of monodisperse microspheres were synthesised from three different CPs (red, green and blue emitters, *i.e.*, across the visible spectrum). The molecular weight of the CP as well as the choice of solvent and surfactant are shown to be important parameters in obtaining large ($>5 \mu\text{m}$) and relatively well formed microspheres. Conjugated polymer microspheres will be shown to have several advantages over conventional dye-doped particles for applications requiring a high emission intensity.

Preface

This thesis is an original work by me, Kirsty Gardner. Chapter 3 is a slightly modified version of research published in the Journal of the Optical Society of America B, 2017, 34, 2140 by K. Gardner, Y. Zhi, L. Tan, S. Lane, Y.-F. Xiao, and A. Meldrum. In Chapter 3, I am the main contributor and did most of the experimental work. Yanyan Zhi carried out the bare cavity measurements, Lige Tan provided assistance with the experimental work, Stephen Lane performed the simulations and took the SEM images, Y.-F. Xiao made enabling contributions to the project, and Al Meldrum led the analysis of the fluorescence, lasing, and transmission spectra. Chapter 4 is a slightly modified version of research published in Advanced Functional Materials, 2018, 28, 1802759 by K. Gardner, M. Aghajamali, S. Vagin, J. Pille, W. Morrish, J. G. C. Veinot, B. Rieger, and A. Meldrum. In Chapter 4, I am the main contributor and did most of the experimental work. Maryam Aghajamali assisted with the fabrication of the microspheres, Sergey Vagin fabricated the conjugated polymer, Jennifer Pille assisted with the experimental work, William Morrish performed the lifetime measurements, Jonathan Veinot and Bernhard Rieger made enabling contributions to the project, and Al Meldrum laid out the WGM theory. Chapter 5 is a preliminary draft of a paper we plan to submit in Spring 2020. In Chapter 5, I am the main contributor and did most of the experimental work, including building the microfluidics set up. Lijuan Zhang assisted with microsphere fabrication, Sergey Vagin fabricated the conjugated polymers, William Morrish helped with the experimental set-up, Peichun Tsai provided useful discussions about microfluidics, and Al Meldrum helped with experimental design and microsphere formation theory. My supervisor, Al Meldrum, contributed intellectually and to the writing and experimental concept of all publications.

Acknowledgements

Thank you to Al for being my supervisor throughout my graduate studies, for helping me become a better experimentalist and writer, and for encouraging me to aim higher and explore the opportunities that came my way. You've made the lab a fun and inclusive place to be and I've thoroughly enjoyed the time spent working with you.

Thank you, Mum, for making sure I got the chance to go to university, for always encouraging me to choose my own path, and for being happy for me even when I moved 7000 km across the ocean to Canada (of all places). To my brothers, Matthew, Carl and Craig, thank you for your e-mails and video calls which kept me connected to you. To Loz, the coolest family member, thank you for talking physics with me and for encouraging me to ask questions. To my grandparents, Christine and Ian, thank you for being proud of me and believing in me.

Thank you to Annika for always telling me that I could do this. Your understanding when I was struggling was always deeply appreciated and you were instrumental in helping me stay happy, healthy and active throughout this journey.

Thank you to my colleagues and friends: William, Stephen and Roshani, Rose, Hui, Lijuan, Maryam, Sergei, Andy and Heun-Jung, Holly and Peter, Ed and Memo, and everyone else who has shared coffee breaks with me, taken walks in the sunshine, and reminded me that at least half the point of a PhD is to have fun with what you're doing.

Thank you to John Davis and Mark Freeman for your insight, questions, and guidance throughout. Thank you to Jon Veinot for access to your lab and also for the support of ATUMS. To Greg Popowich and James Chaulk, thank you for fun conversations and helping me when I was stuck; you both rock. Thank you to AITF for funding me for most of my years in the program.

Thank you to Odin, Fossey and Fonzie, for being fluffy and cute in times of stress.

Contents

List of Figures	viii
1 Introduction	1
1.1 Optical resonances: the whispering gallery modes	1
1.1.1 Formation of WGMs	1
1.1.2 Mode numbers	2
1.1.3 FSR, mode volume and Q-factor	3
1.2 Spherical Microcavities	9
1.2.1 Coupling light in and out of microcavities	9
1.2.2 Applications of fluorescent microspheres	10
1.3 Polymers	11
1.3.1 Basic Description	11
1.3.2 Molecular weight and dispersity	12
1.3.3 Properties of polymers	13
1.4 Conjugated polymers	14
1.4.1 Structure	14
1.4.2 Optical properties and applications	18
1.5 Laser dyes and dye-doped polymers	19
1.5.1 Structure and optical properties of laser dyes	20
1.6 Fluorescence quenching and bleaching mechanisms	21
1.6.1 Concentration quenching	21
1.6.2 Triplets	22
1.6.3 Photobleaching	25
1.7 Lasing in polymer microspheres	26
2 Experimental Methods	29
2.1 Making microspheres	29
2.1.1 Glass microspheres	29
2.1.2 Polymer coatings on glass microspheres	33

2.1.3	Conjugated polymer microspheres - emulsification method	33
2.1.4	Conjugated polymer microspheres - microfluidics method	36
2.2	Fluorescence spectroscopy	39
2.2.1	Spectral Imaging	40
2.2.2	Solution-based fluorescence and absorption measurements	41
2.2.3	Fluorescence Lifetimes	42
3	Whispering Gallery Mode structure in polymer-coated lasing microspheres	43
3.1	Introduction	44
3.2	Experiment	45
3.3	Simulation	46
3.4	Results and Discussion	47
3.5	Interpretation and analysis	58
3.6	Conclusion	61
4	Ultrabright Fluorescent and Lasing Microspheres from a Conjugated Polymer	63
4.1	Introduction	63
4.2	Results and discussion	65
4.3	Conclusion	72
4.4	Experimental section	72
4.5	Supplementary information	76
5	Monodisperse arrays of large, high-brightness conjugated polymer microspheres	79
5.1	Introduction	79
5.2	Results and Discussion	81
5.3	List of Experiments to be completed	91

5.4 Experimental Section	92
6 Conclusion	98
References	102

List of Figures

- 1.1 Molecular structure diagrams for (a) PMMA and (b) PBzMA. In PBzMA, one CH₃ group is replaced with a benzene ring. 14
- 1.2 (a) Molecular structure diagram for polyacetylene. The repeat unit is shown enclosed in the yellow box and the alternating single-double bond backbone is represented by the alternating blue-green oblongs. (b) The 2p_z-orbitals are present on adjacent carbon atoms. (c) The p-orbitals overlap along the backbone of the polymer to form π-bonds. 16
- 1.3 Molecular structure diagrams for a) poly(para-phenylene) and b) poly(para-phenylenevinylene). The repeat unit for each is shown in the yellow rectangle, and the alternating single-double bond backbone is highlighted by the blue-green rectangles. 17
- 1.4 Structures of common families of laser dyes. (a) Rhodamine. (b) Fluoroscein. (c) Coumarin. (d) BODIPY. 20
- 1.5 Jablonski diagrams illustrating the energy levels in a fluorescent molecule. (a) An electron is optically excited from a vibrational mode of the ground singlet state S₀ to S₁, and then undergoes rapid internal conversion to the lowest level of S₁. It then emits a photon to return to a vibrational state of S₀, and relaxes again by internal conversion to the lowest level of S₀. (b) Spin-orbit coupling allows intersystem crossing from S₁ to T₁; the T₁ state is long-lived and the electron eventually emits a photon when it returns to S₀. 25
- 1.6 (a) Unoxidised PPV, with a conjugated backbone. (b) Oxidised PPV. The conjugation along the backbone is broken. 26

1.7	(a) A mode with a low Q shifts by $\Delta\lambda$; the intensity change at a fixed wavelength is small. (b) A mode with a higher Q shifts by the same $\Delta\lambda$; the intensity change at a fixed wavelength is much bigger.	27
2.1	Diagrams of the process used to make glass microspheres. (a) A weight is attached to the bottom of the fibre, which itself is attached with tape to the fibre holder. (b) The fibre holder is attached to a 3D positioning stage and the fibre is placed at the focus of a CO ₂ laser. (c) As the fibre is moved upwards, it melts and a tapered section forms. (d) The laser power is increased until the fibre breaks. (e) A sphere forms from the melted glass. (f) The fibre is moved downwards and the sphere increases in size; this continues until the sphere is attached to the fibre by a thin neck.	31
2.2	Top-down view of set-up.	32
2.3	Optical microscope image of a glass microsphere of diameter $\sim 50 \mu\text{m}$. The black line is the entrance slit of the spectrometer.	32
2.4	Diagram of PVA forming a layer around a droplet of polymer dissolved in chloroform, all in water.	34
2.5	Diagram of experimental set up.	37
2.6	(a) Photograph of a square capillary after the hole was drilled into the centre of one face. (b) Photograph of a circular capillary inserted into a square capillary, before glue was applied.	38
2.7	(a) Spectral image of lines from a neon calibration lamp, labelled with their pixel values and known wavelength in nm. (b) The calibration curve (line) obtained from the calibration spectral image.	41

3.1	Schematic of the optical setup used to collect and analyse the microsphere fluorescence (using a CW laser) or lasing (using a pulsed laser). The image lands on the slit and the part that goes through it enters the spectrometer.	46
3.2	Schematic (left) and secondary electron SEM image (right) of the multilayered microsphere.	48
3.3	TE-polarised fluorescence (red) and lasing (blue) spectra from a bilayer coated microsphere. The data has been scaled for clarity. Normalised to equivalent average pump powers the WGM spectrum was typically much weaker than the lasing one. The lasing threshold behaviour is shown in the inset. The excitation intensities (I_{ex}) were obtained using a variable neutral density filter (the transmission percentages are on the x-axis), with the highest value corresponding to $\sim 50 \mu\text{J}/\text{pulse}$	49
3.4	Transmission spectra taken for three different taper polarisations, showing differences in individual modes but the same overall pattern of larger combined “depressions” at ~ 635.1 , 636.6 , and 638.1 nm. The shaded blue lines highlight regions where the modes converged into the larger “dips” in each spectrum. The data are offset for clarity.	50
3.5	(a) Simulated mode structure for an $\sim 67 \mu\text{m}$ diameter microsphere with a polymer bilayer coating. (b) TE-polarised fluorescence and lasing WGMs (upper and lower red lines, offset for clarity), and a cold-cavity transmission spectrum (green) showing also a moving average (blue). (c) Zoom-in between 636.6 and 636.8 nm, showing the transmission spectrum (blue; moving average) and corresponding lasing mode (red). (d, e) Transmitted and lasing images of the same microsphere. The scale bar is $50 \mu\text{m}$	53

3.6	TE-polarised fluorescence and lasing spectra taken from the equator of the microsphere whose lasing image is shown in the inset. The lasing modes are more numerous and closely spaced than the fluorescence peaks.	55
3.7	FDTD resonance power image and spectrum for a TM polarised (radial E-field) cone emitter with the detector at the sphere's equator. In (a) the intensity of a TE mode (axial E-field) with $n = 1$ and $l = 26$ is shown in a plane that bisects the structure. The two strong antinodes at the tip of the sphere were frequently observed in samples showing this type of lasing spectrum. The inset depicts the same resonance in a cross section through the equator of the sphere. The TE-polarised spectrum is shown in (b); although the resonances are TE-polarised, smaller peaks are also observed at the expected TM resonant wavelengths.	57
3.8	Simulated fluorescence spectrum (blue line) obtained by convolving the spectral system response (inset) with the transmission data shown in Figure 3.5. The experimental data (red line) is shown for comparison.	59
4.1	Normalised absorbance and fluorescence spectra for solid MEH-PPV films (red) and for MEH-PPV dissolved in toluene (blue). The inset shows the fluorescence decays using the same colour scheme. The very slight "bump" at ≈ 2 ns is probably a weak afterpulse from the PMT.	66

4.2	a) Helium ion microscopy image of a single gold-coated MEH-PPV microsphere over 100 μm in diameter. b) Scanning helium microscope of a single sphere which has been sliced open by a focused ion beam. Three small voids are visible in the interior. c) A single large MEH-PPV microsphere containing a network of interpenetrating pores. d) Fluorescence image showing a small group of MEH-PPV microspheres. The violet background is from the excitation LED. e) Fluorescence image of two MEH-PPV microspheres of nearly the same size, resting in adjacent grid holes. Some smaller microspheres escaped the filtering procedure by sticking to the larger ones. f) Size distribution histogram for the sample shown in (d). The mean diameter is 14.3 μm . g) Fluorescence image showing a group of lasing MEH-PPV microspheres. The spectrometer entrance slit is visible running through the centre of the image.	68
4.3	a) TM-polarised fluorescence spectrum (blue dashed line) from a single 6.6 μm diameter microsphere, showing a complicated whispering gallery mode structure. When pumped above a threshold of $\approx 800 \mu\text{J cm}^{-2}$, the WGMs narrowed drastically, suggesting the onset of lasing. b) Polarisation effects in the lasing WGMs. Only the tangential and radial electric fields can propagate to the microscope objective, which is consistent with the change only in intensity but not in lasing wavelength as the polariser is rotated through 90° . The threshold behaviour of the lasing is shown in the inset. c) Evolution of the emission spectrum as a function of pump power. d) Lasing spectra for microspheres of differing diameters.	70

4.4	a,b) Grayscale images of a pair of Suncoast Yellow (SC) and slightly smaller MEH-PPV (ME) microspheres, respectively. Both the images were taken using a 405 nm LED operated under identical conditions. The image intensities have been scaled differently; otherwise the SC spheres are nearly impossible to see. c) Raw (unscaled) intensity profiles taken across the sphere pairs. The ME spheres, although smaller, have an integrated intensity 23 times greater than that of the SC microspheres.	71
4.5	Diagram of the optical set up used to excite fluorescence and collect spectra from the microsphere.	75
4.6	Sample ¹ H NMR spectra of the MEH-PPV with M _n ca. 11 kg/mol. The signals of the aldehyde groups are clearly seen in the region 9.5 – 11 ppm. Assuming they are end-groups of the polymer chains, an average polymerisation degree of 24 can be calculated, which leads to M _n = ca. 6 kg/mol. The overestimation of molecular weight by GPC measurements is due to the referencing to polystyrene (PS). Whereas PS tends to form a macro-conformation close to a random coil in chloroform solution, MEH-PPV macro-conformation is closer to linear, more like a rigid rod. Thus MEH-PPV macromolecules have lower molecular weight than PS with the same mean hydrodynamic radius. The peak at 5.3 ppm is not common for MEH-PPV and is not observed in the as-synthesised product. It is characteristic of a vic-diol functionality which comes from an unaccomplished cracking reaction (an oxidised but not yet cleaved double bond). This reduces the effective conjugation in the macromolecules and explains a shift of the polymer colour from red to orange-red compared to the samples with higher molecular weight.	76

4.7	Molecular weight distribution measured by gel permeation chromatography (see experimental section) in the as prepared MEH-PPV polymer, and after 24 or 72 hours cracking in toluene. The MEH-PPV as-synthesised has M_n ca. 110 kg/mol and M_w ca. 1000 kg/mol, after 24 hours cracking it yields M_n ca. 30 kg/mol and M_w ca. 140 kg/mol, and after 72 hours cracking: M_n ca. 11 kg/mol and M_w ca. 31 kg/mol. Note that the number-averaged (M_n) and weight-averaged (M_w) molecular weights are distinctly different from the peak values. . . .	77
4.8	High magnification view of an uncoated MEH-PPV microsphere. The field of view is 10 μm x 10 μm . Some cratering is apparent on the surface, likely due to the subsurface void structure as reported in the main MS. However, with this exception, the surface of the microsphere is much smoother than the wavelength of light and very few irregularities can be observed. Some material, possibly PVA, can be seen to form an attachment to a neighbouring microsphere.	78
5.1	Stick diagrams of the three synthesised polymers. (a) MEH-PPV (Red). (b) EH-P(PVPVP) (Green). (c) MEH-PPP (Blue).	82
5.2	Absorption and fluorescence spectra for the three polymers in films. Dashed lines represent absorbance, solid lines represent fluorescence.	83
5.3	Fluorescence images of patterned droplets. (a) MEH-PPP (b) EH-P(PVPVP) (c) MEH-PPV.	84
5.4	(a) Droplet lasing image. The yellow-green area is where the laser is incident on the spheres. (b) Image of multiple droplets. The position of the laser beam is indicated by the dashed yellow circle. Red equatorial bands can be seen even on microspheres that are not being directly pumped by the laser. (c) Droplet fluorescence and lasing spectra.	85

5.5	(a) Liquid droplets of the red polymer in a close-packed array. (b) Solid microspheres in a hexagonal pattern. (c) An overlay of images (a) and (b), showing that the solid microspheres form just below and to the right of the centre of the liquid droplets.	87
5.6	(a) Droplet diameter dependence on polymer flow rate. The diameter of the liquid droplets increases linearly with the MEH-PPV flow rate. (b) Solid microsphere diameter dependence on polymer flow rate. Although there are only three points, the diameter does not appear to increase linearly with flow rate. (c) Fluorescence images showing the 3 samples of differently sized PPV solid particles referred to in (b).	89
5.7	Fluorescence image showing green and blue monodisperse microspheres.	90
5.8	Scheme 1: Synthesis of MEH-PPP.	95
5.9	Scheme 2: Synthesis of the monomer precursor of EH-P(PVPVP).	95
5.10	Scheme 3: Synthesis of EH-P(PVPVP).	95

List of Abbreviations

3D	three dimensional
AWG	American wire gauge
BLA	bond length alternation
BODIPY	4,4-difluoro-4-bora-3a,4a-diaza-s-indacene
CP	conjugated polymer
CW	continous wave
DCM	4-(dicyanomethylene)-2-methyl-6-(4-dimethylaminostyryl)-4H-pyran
DI	deionised
DOO-PPV	poly(2,5-dioctyloxy-p-phenylenevinylene)
EH-P(PVPVP)	poly-((1E,1'E-(2,5-bis(2-ethylhexyloxy)-1,4-phenylene)-bis(ethene-2,1-diyl))bis(2,5-dimethoxybenzene)-4,4'-diyl)
FDTD	finite difference time domain
FIB	focused ion beam
FSR	free spectral range
FWHM	full-width at half-maximum
GPC	gel permeation chromatography
GRIM	Grignard metathesis
HDPE	high-density polyethylene

HOMO	highest occupied molecular orbital
IC	internal conversion
ISC	intersystem crossing
LDPE	low-density polyethylene
LED	light-emitting diode
LUMO	lowest unoccupied molecular orbital
MEH-PPV	poly(2-methoxy-5-(2-ethylhexyloxy)-1,4-phenylene-vinylene)
MEH-PPP	poly(2-methoxy-5-(2-ethylhexyloxy)-p-phenylene)
MW	molecular weight
NMR	nuclear magnetic resonance
OLED	organic light-emitting diode
PBzMA	poly(benzylmethacrylate)
PHMB	poly(hexamethylene biguanide)
PMMA	poly(methylmethacrylate)
PMT	photomultiplier tube
PP	polypropylene
PPP	poly(para-phenylene)
PPV	poly(para-phenylenevinylene)
PS	polystyrene

PTFE	polytetrafluoroethylene
PVA	poly(vinyl acetate)
PVP	poly(1-vinyl-2-pyrrolidone)
QE	quantum efficiency
R610	rhodamine 610
SEM	scanning electron microscope
SGS	self guided spectrograph
SMF	single mode fibre
SNR	signal-to-noise ratio
SOC	spin-orbit coupling
TE	transverse electric
THF	tetrahydrofuran
TIR	total internal reflection
TM	transverse magnetic
UV	ultraviolet
WGM	whispering gallery mode

Nomenclature

A	absorbance
a	radius
α	absorption coefficient
B	correlation length
c	speed of light in vacuum
\bar{D}	dispersity
D	diameter
$\Delta\lambda_{FSR}$	free spectral range in wavelength
$\Delta\lambda$	linewidth in wavelength
$\Delta\nu_{FSR}$	free spectral range in frequency
$\Delta\nu$	linewidth in frequency
$\Delta\omega$	linewidth in angular frequency
E_g	band gap
\vec{E}	electromagnetic field
e	eccentricity
ϵ	dielectric constant
η	coupling efficiency
h	Planck's constant
I	intensity

L	bond length
l	polar mode number
λ	wavelength
M_N	number average molecular weight
M_W	weight average molecular weight
M	integer
m	azimuthal mode number
μ	mean diameter
N_c	number of carbon atoms
N	refractive index
n	radial mode number
N_{az}	number of maxima in electric field distribution in azimuthal direction
N_p	number of maxima in electric field distribution in polar direction
ν	frequency
ω	angular frequency
ω_0	angular frequency of resonant mode
$P_\lambda(\lambda, T)$	intensity of blackbody spectrum
Q-factor	quality factor
S_0	ground singlet state

S_1	first excited spin singlet state
σ	root-mean-squared size or standard deviation
T_g	glass transition temperature
T	temperature
T_1	first triplet state
τ	time constant of energy decay
U	total energy of confined light field
U_0	initial total energy of confined light field
V	mode volume
w_i	weight fraction
x_i	mole fraction

1 Introduction

This thesis explores the optical and microstructural properties of fluorescent and lasing microspheres. The work is developed chronologically from my initial studies of the lasing modes in layered dye-doped polymer coatings on silica microspheres and ending with my latest investigations of size controlled and self-assembled conjugated polymer (CP) microspheres and microlasers.

I begin, therefore, with a short review on the whispering gallery modes of microspheres, including the basic resonance parameters and loss mechanisms. I then move to a brief review of conjugated polymers and their associated light emission mechanisms. Laser dyes and their typical quenching and bleaching mechanisms are also discussed in the context of the experiments on dye-doped lasing microspheres.

After this basic introduction, the thesis will describe the experimental work in more detail than is provided in the associated publications, in order to better serve as a jumping off point for future work. Then I move into the three “paper chapters” that are the main publications that came from my research. Two of these are published and one is in preparation, with expected completion of the experimental work as soon as possible after the COVID-19 pandemic. Finally, I make some general conclusions about the main contributions of this work and suggest possible future directions.

1.1 Optical resonances: the whispering gallery modes

1.1.1 Formation of WGMs

Electromagnetic waves can form resonant modes in a cavity with circular symmetry. These modes are known as whispering gallery modes (WGMs), named after the acoustic resonances reported in St Paul’s cathedral and explained by Lord Rayleigh in 1910 [1]. As the wavelength of light is approximately 10^6 times smaller than that of sound, the cavities in which WGMs can be readily observed are roughly 10^6 times smaller than the

original whispering gallery. Examples of such cavities include microdisks [2, 3], microtoroids [4, 5], microcylinders [6, 7], microrings [8, 9] and microspheres [10, 11, 12]. Under certain conditions, light circulates within the resonator and forms a closed path. For optical path lengths along the circumference equal to an integer number of wavelengths, an optical standing wave can form [13]. In the simplest geometric approximation, the resonant wavelengths are given by [14, 15]:

$$M\lambda = 2\pi aN \quad (1)$$

where M is an integer, λ is the wavelength of a resonant mode, a is the radius of the cavity, and N is the refractive index of the cavity.

The conditions that must be met for the development of WGMs include [16]:

1. The refractive index (N) of the dielectric must be greater than that of the surroundings, in order to have total internal reflection (TIR).
2. Light must be incident at a shallow angle with respect to the surface normal to permit total internal reflection.

1.1.2 Mode numbers

In a microsphere, modes are characterised by 3 mode numbers: a radial mode number, $n = 1, 2, 3 \dots$, a polar mode number, $l = 0, 1, 2 \dots$, and an azimuthal mode number, $m = -l \rightarrow +l$. The number of maxima in the electric field distribution in the polar direction is given by $N_p = l - m + 1$, and in the azimuthal direction by $N_{az} = 2m$. Modes with mode numbers m and $-m$ are counterpropagating modes, which give rise to an optical standing wave [17, 18]. In a perfectly spherical microsphere, modes of different $|m|$ are degenerate [19].

For each value of m there are many possible modes, each with different values of n . The “equatorial modes” are given by $m = l$ and $n = 1$. For these

modes, $N_p = 1$ and the modes are tightly bound to the equator of the microsphere and have the smallest mode volumes [4]. In addition to their mode numbers, the resonances are also characterised by the polarization, which can be either transverse electric (TE), where the electric field is perpendicular to the plane of propagation, or transverse magnetic (TM), where the electric field is radial to the equator.

1.1.3 FSR, mode volume and Q-factor

FSR The free spectral range (FSR) of a microresonator is the separation in frequency between adjacent modes. In microspheres the frequency separation, $\Delta\nu_{FSR}$, of modes with the same polarization and radial mode number, n , but differing by one mode number, l , is given by [16]:

$$\Delta\nu_{FSR} = \frac{c}{2\pi a N} \quad (2)$$

where c is the speed of light in vacuum, a is the microsphere radius, and N is the refractive index of the microsphere. When converted into wavelength, the FSR is not constant (as a function of the wavelength) and the wavelength separation $\Delta\lambda_{FSR}$ is given by [20]:

$$\Delta\lambda_{FSR} = \frac{\lambda^2}{2\pi a N} \quad (3)$$

where λ is the wavelength of the mode, a is the resonator radius, and N is the refractive index of the microsphere.

Mode Volume The mode volume of a microresonator can be thought of as the spatial confinement of the resonant electromagnetic field. The mode

volume is often defined as [17, 21, 22, 23]:

$$V = \frac{\text{stored energy in mode}}{\text{maximum energy density of mode}} = \frac{\int_V \epsilon(\mathbf{r}) \left| \vec{E}(\mathbf{r}) \right|^2 d^3r}{\max \left(\epsilon(\mathbf{r}) \left| \vec{E}(\mathbf{r}) \right|^2 \right)} \quad (4)$$

$$\epsilon(\mathbf{r}) = \begin{cases} N^2 & \text{for } r < a \\ N_{external}^2 & \text{otherwise} \end{cases} \quad (5)$$

where $\epsilon(\mathbf{r})$ is the dielectric constant of the material, $N_{external}$ is the refractive index of the surrounding medium, and $\vec{E}(\mathbf{r})$ is the electromagnetic field. It is usually desirable to have small mode volumes, particularly for applications such as lasing which require large photon densities [17, 21].

While commonly used, there are limitations to this equation. One is that the integral (and therefore the mode volume) diverges when evanescent fields are taken into account, unless an arbitrary cut-off for the evanescent field is introduced [22, 24]. Another is that for structures with complex permittivities, this equation can yield negative energy densities which are obviously unphysical [24, 25]. When this equation is applied to high-Q cavities, good agreement is found with the mode volumes that are estimated from experimental observations [26, 24]; however, it is not generally applicable to low-Q cavities or plasmonic systems.

Q-factor One important property of a microcavity is its quality factor (Q-factor). The Q-factor of a cavity is a measure of how well it stores energy [17], with larger Q-factors meaning that the cavity stores light for a longer time, *i.e.*, it is less lossy. For most applications, higher Q-factors are desirable. Lasing, for example, requires that the optical gain within the resonant cavity is greater than the losses, so a higher Q-factor (which implies lower losses) is desirable in lasing cavities [14]. In addition, the lasing threshold decreases

linearly with Q [27], and thus a high Q implies lasing with a lower power input.

The Q -factor is defined as the ratio of the time-averaged energy stored in the cavity to the energy loss per oscillation of the electromagnetic field [28]:

$$Q = \omega_0 \frac{\text{stored energy}}{\text{power loss}} \quad (6)$$

One can also write Equation 6 as [29]:

$$Q = \frac{U(t)}{-\left(\frac{dU(t)}{dt}\right)/\omega_0} \quad (7)$$

where $U(t)$ is the total energy of the confined light field, ω_0 is the angular frequency of the resonant mode, and $-\left(\frac{dU(t)}{dt}\right)/\omega_0$ represents the energy lost in each oscillation of the electromagnetic field. Rearranged, this gives the following differential equation:

$$\frac{dU(t)}{dt} = \left(\frac{-\omega_0}{Q}\right)U(t) \quad (8)$$

After assuming a trial solution of the form $U(t) = Ae^{-t/\tau}$ and imposing the condition that $U(t) = U_0$ when $t = 0$, we find that $A = U_0$ and $\tau = \frac{Q}{\omega_0}$. The solution to equation 8 is therefore:

$$U(t) = U_0 e^{(-\omega_0 t/Q)} \quad (9)$$

From this we see that the energy stored in a cavity decays exponentially over time with a time constant $\tau = \frac{Q}{\omega_0}$. As Q increases, the time constant increases and the stored energy decays more slowly.

To determine the resonant lineshape, we first note that $U(t) \propto E(t)^2$, where $E(t)$ is the electromagnetic field, so $E(t) = E_0 e^{-\omega_0 t/2Q} e^{-i|\omega|t}$. We use the Fourier transform between the time and frequency domains, according to $E(t) = \frac{1}{2\pi} \int_{-\infty}^{+\infty} E(\omega) e^{-i\omega t} d\omega$, and solve to find that the resonant lineshape

$E(\omega)$ is Lorentzian: [28, 29]:

$$|E(\omega)|^2 \propto \frac{1}{(\omega - \omega_0)^2 + (\omega_0/2Q)^2} \quad (10)$$

with a linewidth given by $\Delta\omega = \frac{\omega_0}{Q}$. Thus, $Q = \frac{\omega_0}{\Delta\omega} = \frac{\nu_0}{\Delta\nu} = \frac{\lambda_0}{\Delta\lambda}$, where ν is the frequency and λ is the wavelength, any of which can be directly measured experimentally from the cavity spectrum.

At this point, we should consider the factors which determine the Q-factor of a cavity. To do this, we must consider the sources of loss in microcavities, which include radiation losses, scattering losses, and absorption losses. Each of these contributes to the overall Q-factor and thus we can define Q in terms of these separate losses [30]:

$$\frac{1}{Q} = \frac{1}{Q_{\text{radiation}}} + \frac{1}{Q_{\text{scattering}}} + \frac{1}{Q_{\text{absorption}}} \quad (11)$$

Radiation loss is due to the curvature of the resonator surface. The evanescent field of a WGM extends outside the microsphere, and the further away the light is from the centre of the microsphere, the longer the distance it must travel in one trip around the microsphere. The result is that light further away from the center of the microsphere lags behind and is lost [31]. It has been observed that $Q_{\text{radiation}}$ increases exponentially with increasing diameter (D) [10, 23, 32, 33]. As the diameter increases, radiation losses become less important [34] and for large microresonators defined as $\frac{D}{\lambda} \geq 15$ [10], $Q_{\text{radiation}}$ becomes so large that the losses due to radiation can be neglected [10]. Typical values for microspheres used in this work are $D \sim 10 - 50 \mu\text{m}$ and $\lambda \sim 550 \text{ nm}$, giving $D/\lambda \sim 20 - 90$, within the regime where radiation losses are negligible [10].

Attenuation of light in the microresonator is another important source of loss. $Q_{\text{absorption}}$ depends on the absorption coefficient, α , and refractive

index, N , of the material [10]:

$$Q_{absorption} = \frac{2\pi N}{\alpha\lambda} \quad (12)$$

Polymer refractive indices are typically between $N=1.4$ and 1.6 [35] for light in the visible wavelength range. Optically transparent polymers such as poly(methylmethacrylate) (PMMA) and polystyrene (PS) have absorption coefficients of around $2 \times 10^{-4} \text{ cm}^{-1}$ at 488 nm and $5 \times 10^{-4} \text{ cm}^{-1}$ at 647 nm [36], giving $Q_{absorption} \sim 10^8$ over this wavelength range, which is considered to be reasonably high [21, 37].

However, the inclusion of laser dyes into these polymers can drastically increase the absorption coefficient. Takeda et al measured the absorption coefficient of PS doped with Nile Red at a concentration of $\sim 5 \times 10^{-3} \text{ mol/L}$; at 588 nm , they found that the absorption coefficient was around 100 cm^{-1} , giving $Q_{absorption} \sim 10^3$ [38]. Similar results were found for conjugated (non-transparent) polymers. For example, the absorption coefficient of poly(2,5-dioctyloxy-p-phenylenevinylene) (DOO-PPV) was measured to be 30 cm^{-1} at 630 nm , giving $Q_{absorption}$ of 10^3 [39, 40]. The use of a fluorescent, absorbing material clearly limits the maximum achievable Q-factor in fluorescent polymer microspheres.

Scattering is another source of loss. It is mainly due to surface roughness which causes light to scatter out of the resonator; smoother microcavity surfaces (less scattering) result in higher Q-factors. The scattering-related Q factor can be described as [10]:

$$Q_{scattering} = \frac{\lambda^2 D}{2\pi^2 \sigma^2 B} \quad (13)$$

where λ is the wavelength of the mode, D is the diameter of the resonator, σ is the root-mean-squared (rms) size of the surface features and B is the correlation length of the surface features (an indication of their average separation [41]). The values of σ and B are often difficult to measure ex-

perimentally but one can estimate the upper limit of $Q_{scattering}$ by looking at silica microspheres, which represent some of the smoothest (solid) microspheres. For silica microspheres, values as low as $\sigma = 2$ nm and $B = 5$ nm are possible [42]. Taking $\lambda = 550$ nm, $D = 50$ μ m (representative values for the wavelength of light and diameter of microspheres used in this work) $Q_{scattering} \sim 10^8$ would be obtained.

Microcavities made from polymers often have rougher surfaces than those which can be achieved in silica microspheres, and the maximum obtainable Q-factors in polymer microcavities are correspondingly lower. In one experiment using microrings made from poly(1-vinyl-2-pyrrolidone) (PVP), $Q_{scattering}$ was found to be 2.5×10^3 [43]. In another work using 10 μ m PS microspheres, $Q_{scattering}$ was calculated to be around 10^4 [38]. The case is better for polymer-coated silica microspheres, which can have higher Q-factors than all-polymer microspheres due to the smoothness obtainable in silica microspheres. As long as the polymer concentration is chosen so that inhomogeneities in the polymer coating are avoided, the final coated structure can have a smoothness similar to the silica microsphere beneath. In one experiment where a silica microsphere was coated with a thin layer of DOO-PPV, the Q-factor of the microsphere decreased only slightly from $Q_{uncoated} = 1.3 \times 10^7$ to $Q_{coated} = 1.2 \times 10^7$ [44]; in another, the Q-factor before coating was around 10^7 and decreased to 10^6 after a polymer coating was added [45].

In cases where the surface of the polymer is rough after fabrication, post-fabrication annealing techniques can be used to decrease the surface roughness and increase $Q_{scattering}$ [46]. One technique is solvent-vapour annealing, which involves exposing polymer films to vapours of a solvent. The solvent is absorbed by the polymer, lowering the polymer's glass transition temperature (T_g) below room temperature and allowing the polymer chains to reorganise and adopt a lower-energy configuration [47]. This can result in a smoother surface and a higher value of $Q_{scattering}$. Another technique is thermal reflow, where a solid polymer is heated to ~ 20 $^\circ$ C below its T_g , decreasing its

viscosity so that surface tension causes the surface to become smoother [48]. This has been shown to increase the Q-factor of polystyrene microrings by an order of magnitude, from $Q=5 \times 10^3$ to $Q=2 \times 10^4$ [49].

In conclusion, for fluorescent polymer microspheres in the size regime of $D/\lambda \geq 15$ (as is the case for the microspheres fabricated in this work), radiation losses can be neglected [10] and the Q-factor is largely determined by absorption and scattering. For all-polymer microspheres, $Q_{\text{absorption}}$ and $Q_{\text{scattering}}$ are estimated to be on the order of 10^3 to 10^4 , whereas for polymer-coated microspheres a higher value of $Q_{\text{scattering}}$ is possible.

1.2 Spherical Microcavities

1.2.1 Coupling light in and out of microcavities

In order to observe the optical resonances in microcavities, one must first couple light into the cavity. The easiest but least efficient coupling method is free space coupling. Here, light (*e.g.*, a laser beam) is incident from free space onto the resonator, possibly after being loosely focused by one or more lenses. While experimentally simple, this method is inefficient because it relies on the radiative coupling of free space light with a microsphere WGM [50]. The coupling efficiency (η) can be estimated using generalised Lorentz-Mie scattering theory [50] and is given by $\eta < (\lambda/a)^2$ [17, 34]. For a sphere of radius 50 μm and a pump wavelength of 500 nm, this would give $\eta < 0.01\%$.

Evanescent coupling offers much better coupling efficiency but is more experimentally complicated. A coupler such as a prism or tapered fibre is brought close (within a few hundred nm [51, 52, 53]) to the microcavity so that the evanescent field of the pump light in the coupler overlaps with the evanescent field of a WGM in the microresonator [17, 54]. Coupling efficiencies of up to 80% can be achieved with prisms [54] and more than 99% with tapered fibres [55, 56], although in this overcoupled regime the Q-factor is reduced due to the losses from the microsphere back into the

coupler [57]. In addition, tapered fibres are mechanically fragile and are prone to degradation from surface contaminants such as dust and water vapour.

Fluorescent coupling is another coupling method which is experimentally simple. The microsphere is doped with a fluorescent material which is then excited through free space by a pump beam. The fluorescent material emits at a broad range of wavelengths; those wavelengths which coincide with a WGM appear as sharp peaks in the fluorescence spectrum. Due to the broad emission spectra, multiple WGMs can be simultaneously excited with this method. The mode visibility (mode visibility = $\frac{I_{max}-I_{min}}{I_{max}+I_{min}}$, where I is the intensity) is a measure of how visible the modes are, with visibilities near one indicating that the background fluorescence is minimal, and lower visibilities indicating that the background fluorescence is higher. Mode visibility depends on Q-factor, where for lower Q-factors a fraction of the fluorescence can scatter out of the cavity before interacting significantly with the mode, leading to a higher background "uncoupled" fluorescence. In addition, if low-Q modes are sufficiently close together then the modes can overlap to some degree which also leads to a non-zero background and a lower mode visibility.

1.2.2 Applications of fluorescent microspheres

Fluorescent microspheres have potential applications in sensing, including refractive index sensing [11, 58, 59], biosensing [60, 61], force sensing [62], temperature sensing [63], and humidity sensing [64]. Sensing is possible because WGMs propagating around the microsphere have an evanescent field which extends outside of the sphere by approximately 100 nm [11] and thus the resonances are sensitive to any external changes in refractive index. A change in refractive index - which can be due to a change in external medium or due to molecules binding to the surface of the microsphere - causes the effective optical path length to change and the mode positions to shift correspondingly. This shift in wavelength can be used as the detection mechanism.

Microspheres are also used for bioimaging [65], where the fluorescent microspheres are taken up by a cell, and as visible carriers for drug delivery [65, 66], where the microsphere contains a drug which is released over time. In both of these latter applications, size control of the microsphere is important. Some macrophage cells can internalize particles up to 10 μm in diameter [67], while other types of cell - such as human cervical carcinoma epithelial cells which are commonly used in cancer research - can only internalize particles less than 3 μm in diameter [68]. For drug delivery, where the microsphere is not taken up by the cell, larger microspheres of 10-50 μm can be used [65]. Other applications for microspheres include flow cytometry [69] biomedical diagnostics [70], tracking contamination and leaks in drilling operations [71], cell tagging and tracking [67], and for studies of fluid flow [72].

1.3 Polymers

1.3.1 Basic Description

Polymers are long chain-like molecules made up of a repeat unit (monomer) which links to other monomer units [73]. Many synthetic polymers (including polycarbonates, polymethacrylates, polystyrene and conjugated polymers with alkyl side chains [74, 75]), are soluble in common organic solvents and are thus solution-processable. Solution-processable polymers are compatible with simple, inexpensive deposition techniques such as spin-coating, drop-casting and ink-jet printing. Other polymers, such as polyethylene, are insoluble in organic solvents [76] and need to be heated, melted and moulded into the desired shape; these polymers are used in applications where chemical resistance is required. Naturally occurring polymers such as collagen, silk and keratin tend to be insoluble in water and organic solvents [77].

1.3.2 Molecular weight and dispersity

The molecular weight (MW) is one important property used to characterise polymers. Broadly speaking, a polymer with a higher molecular weight has longer (heavier) chains. There are two definitions of molecular weight. The “weight average molecular weight”, M_W , is defined as [78]:

$$M_W = \sum_{i=1}^N w_i MW_i \quad (14)$$

where w_i is the weight fraction of polymer chains with a molecular weight of MW_i . Longer (heavier) chains contribute more to the M_W than shorter chains do.

The “number average molecular weight”, M_N , is defined as [78]:

$$M_N = \sum_{i=1}^N x_i MW_i \quad (15)$$

where x_i is the mole fraction of polymer chains with a molecular weight of MW_i . Here, each chain contributes equally to M_N regardless of chain length. In all cases, $M_N < M_W$ because higher MW chains contribute more to M_W than to M_N .

The dispersity, \bar{D} , of a polymer is given by $\bar{D} = M_W/M_N$. In the best-controlled synthetically-produced polymers used for calibration standards (*e.g.*, calibration of gel permeation chromatography systems), $\bar{D} = 1.02$ to 1.10 [78]. Polymers not intended to be used as calibration standards have higher dispersities, $\bar{D} \geq 1.5$.

The MW of a polymer is related to its physical properties. A higher MW leads to a higher tensile strength, increased resistance to deformation under impact [79], improved chemical resistance, and a higher glass transition temperature [80]. However, polymers with a higher MW tend to be less soluble [78, 81]. For applications requiring solution processing, a balance must

be struck; the MW must be high enough that the polymer is mechanically stable [82] (has a high enough T_g to remain rigid at room temperature), but low enough that it can be readily dissolved in the required solvent.

1.3.3 Properties of polymers

Polymers such as polystyrene (PS), polypropylene (PP), high- and low-density polyethylene (HDPE and LDPE), and poly(methylmethacrylate) (PMMA) have densities between 0.9 and 1.3 gcm⁻³ [83, 84]. The Young's modulus - which measures stiffness - of polymers is typically on the order of 0.1 - 3 GPa [84], which is two orders of magnitude lower than those of glass and metals [85]. The low density and relative flexibility of polymer films has led to their uses in smart textiles [86], wearable biosensors [86, 87, 88], flexible solar cells [89], flexible LEDs for displays [90], flexible field-effect-transistor memory devices [91], and large-area flexible thermal and pressure sensors that act as "electronic skins" [92, 93, 94].

The refractive indices of polymers can range from at least as low as 1.29 for Teflon AF 1600 (a fluorinated polymer) [95], up to 1.7 for conventional optically transparent polymers such as PMMA and PS, and up to 2.2 for some conjugated polymers (CPs) [96]. The refractive index can be modified by altering the side groups and substituents [97]. The refractive index of a polymer depends on the molecular polarisability of its repeat units, with a higher molecular polarisability causing a higher refractive index [96, 98]. For example, PMMA has a refractive index of around 1.5 but poly(benzylmethacrylate) (PBzMA) - which is PMMA where one CH₃ group is replaced with a benzene ring (see Figure 1.1) - has a significantly higher refractive index of 1.63 [83, 84] due to the increased polarisability of the benzene group [98]. Other optical properties can be modified in the same way; for example, absorbance at telecommunications wavelengths can be reduced by replacing C-H groups in polymers with C-F groups, which absorb much less strongly at these wavelengths [99, 100, 101]. The ability to tailor

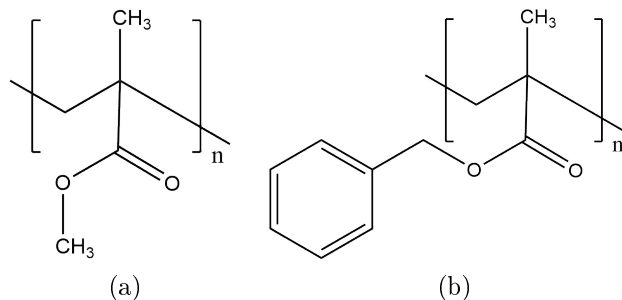


Figure 1.1: Molecular structure diagrams for (a) PMMA and (b) PBzMA. In PBzMA, one CH_3 group is replaced with a benzene ring.

the optical properties of polymers means that they are used in applications where precise control over refractive index and absorption is required, such as waveguides and evanescent waveguide sensors, lenses, and antireflective coatings [98, 102, 103, 104].

1.4 Conjugated polymers

Conjugated polymers (CPs) are a class of synthetic polymers with optical and electronic properties similar to that of semiconductors, making them inherently fluorescent. Because there is no need for dye-doping, the process of finding a common solvent is avoided. Additionally, CPs are much less affected by concentration quenching than dye-doped polymers are, as long side-chains can be added to the polymer to reduce quenching (this will be explained in more detail in Section 1.6.1). Thus, CPs present several potential advantages over conventional dye-doped polymers for the fabrication of fluorescent or potentially lasing microspheres.

1.4.1 Structure

The backbone of a conjugated polymer is comprised of alternating single-double bonds, as seen in Figures 1.2 and 1.3. The resulting electron con-

figuration consists of sp_2 hybridised carbon atoms, which leads to 3 σ -bonding electrons (in the 2s, $2p_x$ and $2p_y$ orbitals) and one p_z orbital per carbon atom, perpendicular to the plane of the molecule, as shown in Figure 1.2 [73, 105, 106, 107, 108]. To see how this gives rise to semiconductor-like properties, we first consider the simplest case of a single molecule. Across a double bond, the two degenerate p_z states overlap and interact, splitting into a bonding π -orbital and anti-bonding π^* -orbital [107]. The π -orbital is the highest occupied molecular orbital (HOMO) and the π^* -orbital is the lowest unoccupied molecular orbital (LUMO).

In a conjugated polymer, there are many repeat units and the π -orbitals overlap along the backbone of the polymer, leading to electron delocalisation. The interactions between all of these degenerate pi-bonds further split the π - and π^* levels into many closely-spaced energy levels, which we consider as energy bands [107]. Conjugated polymers have a π -band which is fully occupied (*i.e.*, a valence band), which is separated by an energy gap from a higher energy π^* -band, which is normally empty (*i.e.*, a conduction band) [108].

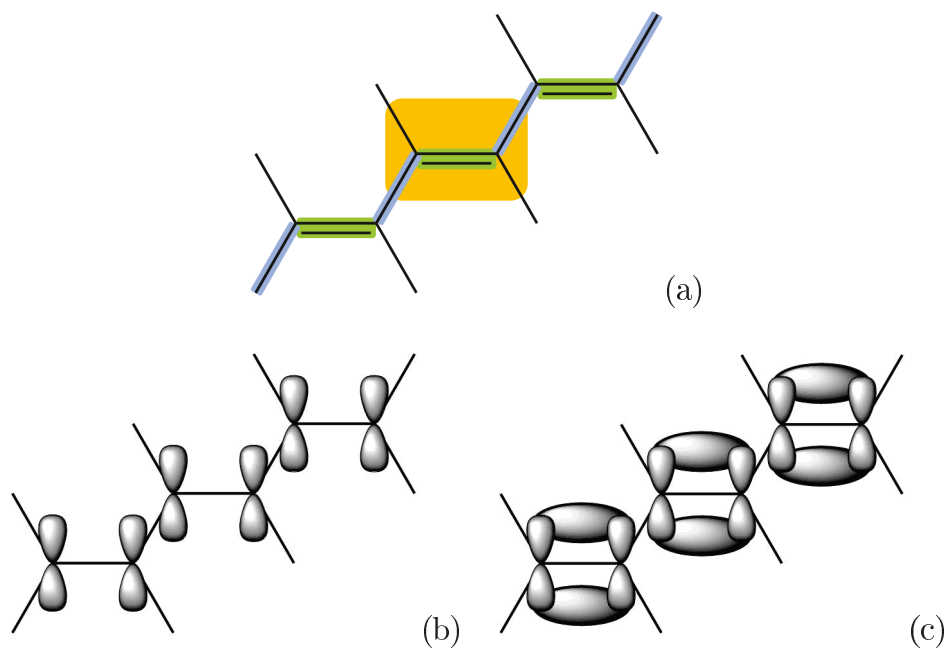


Figure 1.2: (a) Molecular structure diagram for polyacetylene. The repeat unit is shown enclosed in the yellow box and the alternating single-double bond backbone is represented by the alternating blue-green oblongs. (b) The $2p_z$ -orbitals are present on adjacent carbon atoms. (c) The p-orbitals overlap along the backbone of the polymer to form π -bonds.

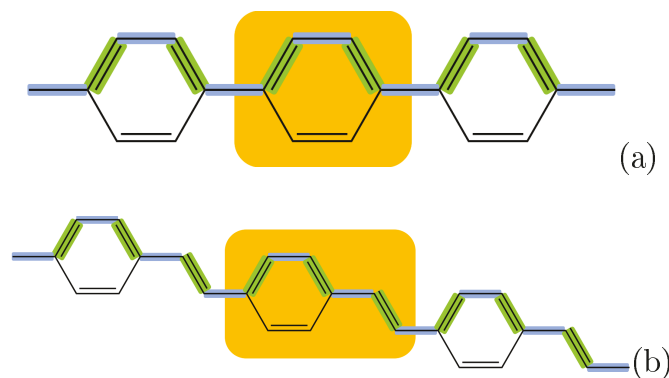


Figure 1.3: Molecular structure diagrams for a) poly(para-phenylene) and b) poly(para-phenylenevinylene). The repeat unit for each is shown in the yellow rectangle, and the alternating single-double bond backbone is highlighted by the blue-green rectangles.

If all the C-C bonds in CPs were the same length, the electrons would be truly delocalised along the whole chain. In this situation, the π - and π^* -bands would be degenerate and there would be no energy gap between them [109]. Such a molecule would behave as a metal in which N carbon atoms contribute N p_z electrons to a band that can hold $2N$ electrons, and thus the band would be half-full [109]. However, such a structure is unstable; instead the molecule adopts a configuration where adjacent bonds alternate between shorter “double” bonds and longer “single” bonds. This is known as the Peierl’s effect, and this “bond length alternation” (BLA) (the difference between the length of the long bonds, L_{long} , and the length of the short bonds, L_{short}) [110, 111]) gives rise to a band gap as the π - and π^* - bands are not degenerate in this case [108, 109, 112]. Broadly speaking, the larger the BLA, the larger the band gap [113], although there are other contributions to the band gap which will be discussed further below.

To summarise, the electronic structure of conjugated polymers consists of two bands, a lower energy π -band which contains N p_z electrons and is full, and a higher energy π^* -band which is empty. The π - and π^* bands are

separated by an bandgap, E_g , which is proportional to the BLA of the CP. This is equivalent to the electronic structure of a semiconductor and is the source of the semiconducting properties of CPs, including their fluorescence.

1.4.2 Optical properties and applications

Many conjugated polymers have bandgaps of around 1 or 2 eV [107]. As discussed in the previous section, the bandgap depends primarily on the degree of BLA in the polymer. However, there are other contributions to the bandgap such as conjugation length, the presence of aromatic rings, and the addition of electron donating or withdrawing side groups.

Conjugation length is the number of carbon atoms, N_c , over which the electrons are delocalised, and it is approximately related to the bandgap by $E_g \propto \frac{1}{N_c}$ [113]. (Note that if CP chains were “perfect”, *i.e.*, had no twists or kinks, then the conjugation length would depend on chain length, or molecular weight. However, defects in the chains result in a conjugation length that is often less than the polymer chain length [106, 114].) A longer conjugation leads to a lower E_g [107, 115].

Aromatic rings tend to confine electrons to the ring, leading to less electron delocalisation along the CP chain and therefore a larger bandgap [111, 116]. The structures of poly(para-phenylene) (PPP) and poly(para-phenylenevinylene) (PPV), derivatives of which are used extensively in the work of this thesis, are shown in Figure 1.3; PPP has more aromatic rings along its chain than PPV and has a larger bandgap [111].

Side groups or chains can also be used to modify the bandgap; electron-donating groups donate electron density to the CP backbone, which raises the HOMO, and electron-withdrawing groups remove electron density from the CP backbone, lowering the LUMO [75, 112]. As the bandgap is the energy difference between the HOMO and LUMO, both of these effects reduce E_g . Conjugation length, aromatic rings and side groups therefore all present simple methods of tuning the bandgap of conjugated polymers.

Many of the optical properties of conjugated polymers are advantageous for fabrication of organic light-emitting diodes (OLEDs), solid state plastic lasers, and photovoltaic cells [117]. In CPs, self-absorption is limited because the Stokes shift is often large enough to ensure that the emission and absorption do not greatly overlap [73, 117]. CPs tend to have high absorption coefficients, $\alpha \approx 10^5$, which means even a thin CP film can absorb a large fraction of the photons from an incident light source [118], allowing the possibility of compact optically pumped lasers and thin solar cells [73, 119]. In addition, fluorescence quantum efficiencies (where quantum efficiency = $\frac{\text{number of emitted photons}}{\text{number of absorbed photons}}$) are often between 10% and 50% depending on the polymer [120, 121].

1.5 Laser dyes and dye-doped polymers

Unlike the case for CPs, common (unconjugated) polymers are not inherently fluorescent. To make a fluorescent polymer solution or film from these materials, a fluorescent dye must be incorporated into the polymer, a process known as “dye-doping”. One method of dye-doping is to first fabricate the polymer microstructures as desired, then use an entrapment method to introduce the dye into the polymer [122]. In the entrapment method, the microstructures are dispersed in an aqueous solution and a hydrophobic laser dye is dissolved in a solvent that is immiscible with water. The microstructure and dye solutions are mixed together until the dye solvent has evaporated. The hydrophobicity of the dye means that it has limited solubility in water; as the solvent evaporates, the dye diffuses into the polymer. The amount of laser dye in the polymer can be controlled by the initial concentration of dye in solution.

Another method of dye doping is to dissolve both the polymer and laser dye in a solvent that is common to both. While this method does require that the polymer and laser dye share a common solvent, it has the advantage that the laser dye is embedded in the polymer matrix throughout the

entire material rather than being limited to the surface as in the entrapment method. The range of available laser dyes is huge [123, 124] and it is usually easy to find a dye at the desired wavelength which is soluble in the required solvent.

1.5.1 Structure and optical properties of laser dyes

Laser dyes are small organic molecules which have been used in dye lasers for decades owing to their high quantum efficiency and range of available emission wavelengths [125]. Examples of laser dye families are the rhodamines, fluoresceins, coumarins, and the 4,4-difluoro-4-bora-3a,4a-diaza-s-indacene family of dyes (known by the trademark name BODIPYs) [126]. Their structures are shown as examples in Figure 1.4. We can see that laser dyes have the same alternating single-double bond structure as conjugated polymers, which is the origin of their band gap structure and fluorescence [126, 127].

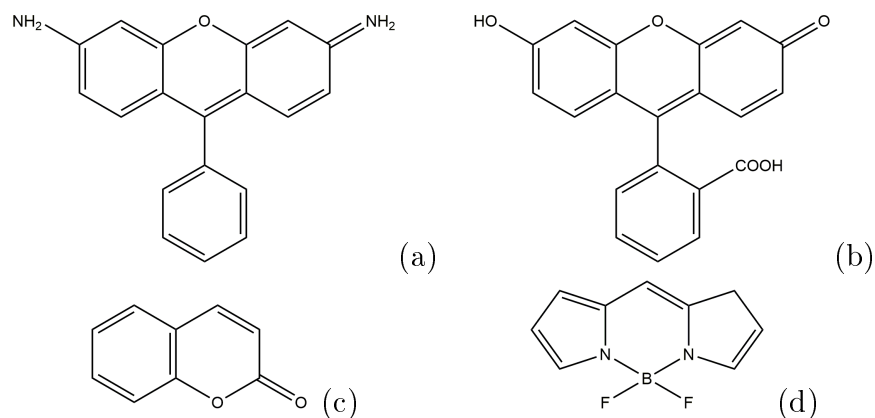


Figure 1.4: Structures of common families of laser dyes. (a) Rhodamine. (b) Fluorescein. (c) Coumarin. (d) BODIPY.

Laser dyes have high quantum efficiencies ranging between 0.5 and 0.95 [128, 129, 130], and exhibit strong absorption due to their large transition moment between the ground state S_0 and the first excited state S_1 . This combination of high quantum efficiency and strong absorption means

that laser dyes can have high emission intensity. In addition, lasing is easily achieved in laser dye solutions as the energy levels of laser dyes allow them to behave as 4-level systems [126].

1.6 Fluorescence quenching and bleaching mechanisms

Laser dyes and conjugated polymers are susceptible to a number of processes which reduce their fluorescence quantum efficiency. These processes can be broadly divided into two categories: bleaching processes, which are irreversible, and quenching processes, which are reversible. The mechanisms for these processes will be explained in the following subsections, with a focus on the processes which are of particular importance in organic fluorophores.

1.6.1 Concentration quenching

For high concentrations of a laser dye, the fluorescence quantum efficiency decreases compared to the case for lower concentrations [131, 132, 133, 134]. This process is known as concentration quenching, or self-quenching. Concentration quenching is problematic because it limits the maximum fluorescence intensity of a solution or film. Initially, increasing the dye concentration results in a brighter solution or film due to the increased number of fluorophores, but above a certain concentration the intensity then decreases due to concentration quenching.

In both solutions and films, the formation of dimers is responsible for concentration quenching [135, 136, 137]. A dimer is an aggregate of two molecules and has a ground state and an excited state; when an excited fluorophore is aggregated with a ground state fluorophore, this excited dimer is referred to as an excimer [135]. Excimers often do not emit at the same wavelength as the original isolated fluorophores and they have lower quantum efficiencies [138]. Formation of excimers thus results in an undesirable decrease in intensity at the original fluorophore wavelength and a decrease in

quantum efficiency. The higher the concentration of the fluorophore, the higher the possibility of aggregation and formation of dimers.

In dye-doped polymer films, concentration quenching is typically observed at around 2-5 wt% (for the common laser dye DCM doped into PMMA), although molecules with bulky side groups can be doped into polymers at concentrations as high as 10 wt% before concentration quenching is observed [131, 139]. In solutions, concentration quenching becomes apparent at concentrations around 2 mM [140]. It is therefore difficult to make a fluorescent, lasing solid film that has a high concentration of laser dye, as concentration quenching renders such films only weakly fluorescent.

One major advantage of conjugated polymers over dye-doped polymers is that CPs are not subject to the same degree of concentration quenching as dyes [141, 142]. While some quenching can still occur if CP molecules aggregate [142], CPs can be made with long side chains that increase interchain spacing [143], decreasing aggregation and limiting energy transfer between chains. This allows films and solid microcavities of pure CPs to be made, which have higher chromophore densities than those made of dye-doped polymers. The increased chromophore density is of particular use when making lasing devices, as it implies that the lasing threshold in CP devices can potentially be lower than in dye-doped polymer films [73, 141].

1.6.2 Triplets

Fluorescence occurs when an electron decays from the first excited spin singlet state S_1 to the ground singlet state S_0 , emitting a photon of energy $h\nu = S_1 - S_0$ (see Figure 1.5). Quenching occurs when instead of decaying from S_1 to S_0 , the electron instead undergoes radiationless intersystem crossing (ISC) from S_1 to a triplet state of lower energy T_1 (see Figure 1.5). While ISC is forbidden due to spin-selection rules [115], the transition is weakly allowed if spin-orbit coupling (SOC) mixes the singlet and triplet states [144, 145]. The strength of the SOC determines how likely the transition between sing-

let and triplet states is, with stronger SOC leading to a higher probability of ISC and thus more quenching. SOC strength increases with atomic number [145], so the presence of heavier atoms in a fluorescent molecule results in more triplet-related fluorescence quenching.

The presence of molecular oxygen in solutions of fluorescent molecules is also well known to generate triplet states [146, 147]. Oxygen is almost always present in solutions and films unless special care is taken to remove it, and its small size allows it to easily diffuse through the solution or film and interact with the fluorescent molecules [148]. When molecular oxygen (which is a triplet in its ground state and a singlet in its excited state) collides with an excited fluorescent molecule, charge transfer can occur. This charge transfer excites oxygen to its singlet state and as a result, the fluorescent molecule is quenched to its triplet state [146, 147]:



where 3O_2 represents the ground (triplet) state of oxygen and ${}^1O_2^*$ represents the excited (singlet) state of oxygen.

Regardless of the mechanism by which triplet states are generated, the low probability of the transition between triplet and singlet states implies that triplet states are long lived [149]; an electron in the T_1 state takes a long time to decay back to S_0 by emission of a photon because this transition is forbidden by spin-coupling rules and is only weakly allowed by SOC. This long-lifetime emission is known as phosphorescence. As the T_1 state tends to be at a lower energy than the S_1 state, phosphorescence usually occurs at longer wavelengths than fluorescence. Because phosphorescence competes with fluorescence, the formation of triplets decreases the quantum efficiency [144] (although in some systems, thermal energy can cause the electron to be excited from the T_1 state back to the S_1 state, resulting in delayed fluorescence rather than phosphorescence [150]).

The accumulation of electrons in triplet states halts lasing action and should be avoided in organic gain media. This can be seen from the Jablonski diagrams shown in Figure 1.5. Organic molecules are effectively 4 level systems owing to the vibrational modes which are present in molecules (see Figure 1.5 a). Optical pumping excites an electron from S_0 to a vibrational mode of S_1 . Internal conversion (IC) rapidly occurs and the electron relaxes to the lowest level of S_1 in less than a picosecond [126]. Emission then occurs from S_1 to a vibrational mode of S_0 , followed by rapid IC to the ground state of S_0 . The rapid IC allows a population inversion to be established at the lowest level of S_1 , necessary for lasing. However, under continuous pumping, electrons accumulate in T_1 states (there is only a small probability of ISC but because the state is long-lived, electrons stay there for a long time). With more electrons in triplet states, population inversion cannot be achieved and lasing stops [126]. To avoid the build up of triplet states, organic dyes are pumped by pulsed lasers rather than continuous wave lasers. Between pulses, enough time elapses for electrons to decay back to S_0 , so the molecule can again fluoresce or lase.

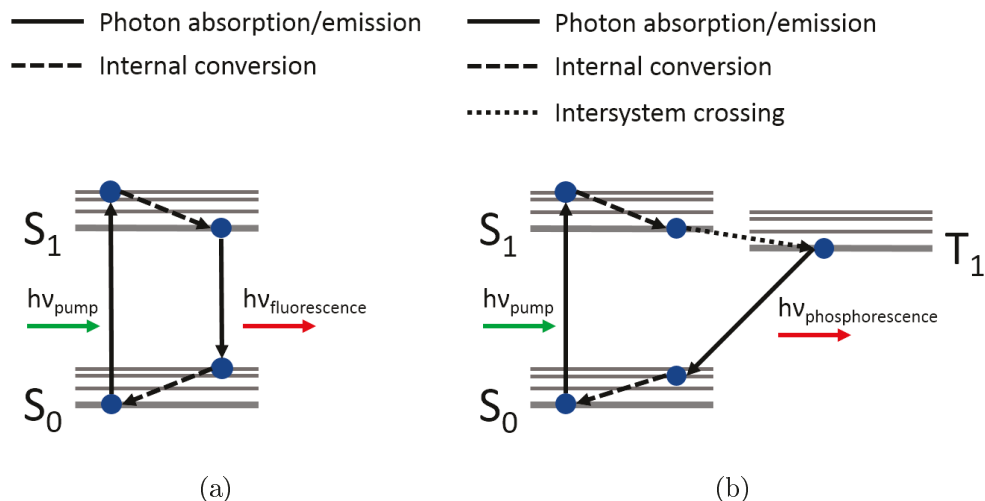


Figure 1.5: Jablonski diagrams illustrating the energy levels in a fluorescent molecule. (a) An electron is optically excited from a vibrational mode of the ground singlet state S_0 to S_1 , and then undergoes rapid internal conversion to the lowest level of S_1 . It then emits a photon to return to a vibrational state of S_0 , and relaxes again by internal conversion to the lowest level of S_0 . (b) Spin-orbit coupling allows intersystem crossing from S_1 to T_1 ; the T_1 state is long-lived and the electron eventually emits a photon when it returns to S_0 .

1.6.3 Photobleaching

Bleaching is described as the irreversible conversion of a fluorescent molecule to a non-fluorescent molecule. When this conversion is due to photoexcitation, the process is known as photobleaching [151]. Oxygen (O_2) is known to be a significant cause of photobleaching at room temperature, and the term photo-oxidation is applied to oxygen-assisted photobleaching processes [151].

As discussed in the previous section, singlet oxygen is often generated in charge transfer interactions with excited fluorescent molecules. Singlet oxygen is highly reactive and can easily oxidise the active species. This

results in double bonds being cleaved, rendering the fluorescent molecule non-fluorescent [152]. An oxidised structure is illustrated in Figure 1.6.

Eliminating oxygen from the fluorescent solution or film is therefore important to prevent permanent degradation of the dye or conjugated polymer molecules. One method of doing so is to put the fluorescent or lasing device in an atmosphere of an inert gas such as nitrogen. Another method is to choose a polymer matrix that is impermeable to oxygen, so that only surface dye molecules are exposed to oxygen and the rest are protected. Finally, a protective layer can be added on top of the fluorescent layer to prevent oxygen from interacting with the fluorescent dye molecules, as we do in Chapter 3.

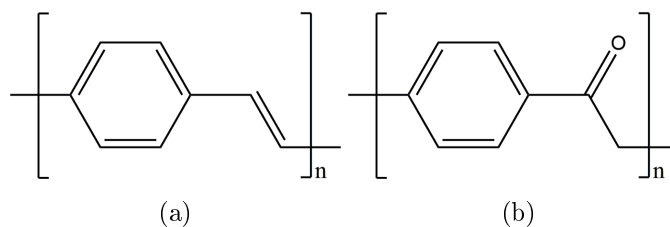


Figure 1.6: (a) Unoxidised PPV, with a conjugated backbone. (b) Oxidised PPV. The conjugation along the backbone is broken.

1.7 Lasing in polymer microspheres

While fluorescent microspheres have been extensively used for sensing applications, background fluorescence can overwhelm the signal, particularly in biomedical applications where many other fluorescent molecules are present [153, 154]. This problem can be overcome by operating the microsphere above its lasing threshold, where the signal-to-noise ratio (SNR) is increased and the emission is easier to detect above the background [67, 153].

Operating in the lasing regime offers other advantages which improve sensor performance. One is that the lasing threshold is sensitive to small changes in the environment (such as refractive index changes as a result

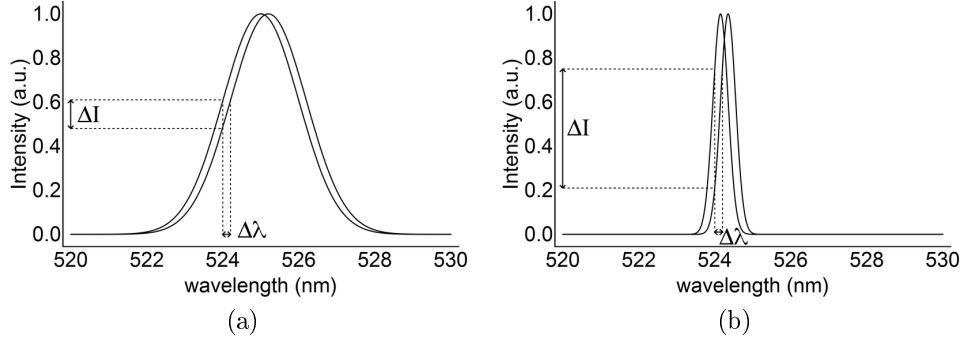


Figure 1.7: (a) A mode with a low Q shifts by $\Delta\lambda$; the intensity change at a fixed wavelength is small. (b) A mode with a higher Q shifts by the same $\Delta\lambda$; the intensity change at a fixed wavelength is much bigger.

of biological processes, or molecules adhering to the surface of the resonator) [153, 155, 156]. Another is that the high Q-factors of lasing modes enables the use of the “intensity variation” sensing scheme. The intensity variation scheme consists of monitoring the intensity at the full-width at half-maximum (FWHM) of a WGM; changes in the external environment cause only a small red- or blue-shift of the resonant mode, but owing to the steep slope of a high-Q mode, the intensity change is much larger than the wavelength shift [157], as shown in Figure 1.7. Finally, the high SNR of lasing WGMs also makes them useful for bioimaging and cell tracking [67], where again fluorescence-based methods have the downside of being overwhelmed by background fluorescence.

For lasing, a high Q-factor is beneficial, which necessitates a smooth surface and a large refractive index contrast between the polymer microsphere and the surrounding medium [158]. The size of the polymer microsphere is also important because at small diameters, radiative losses become significant and reduce the Q-factor enough to prevent lasing. In air, a diameter of at least 5 μm was shown to be required for lasing in dye-doped PS microspheres [38], and in water the diameter should be at least 10 μm for PS microspheres [122].

Lasing dye-doped polymer microspheres have interesting biomedical applications. For example, microspheres of approximately 10 μm diameter can be readily taken up by living cells to become intracellular lasers and their high Q-factor means that they can lase at pump powers low enough to avoid damage to the cells [154]. As previously discussed, the exact spectrum (mode position and intensity of each mode) of a microsphere depends on the microsphere diameter as well as the environment [124, 155]. These properties have been used to distinguish individual cells from one another by their “fingerprint” spectra, allowing them to be tracked as they move [124, 155].

Lasing in CP microspheres has only recently been realised, as the crystallinity of CPs generally leads to microspheres with rough surfaces [159] and correspondingly low Q-factors. In 2017, lasing microspheres were successfully fabricated from several different CPs [160], although the largest was only 5 μm in diameter. (The fact that CP microspheres of diameters smaller than 5 μm can lase can probably be attributed to the slightly higher refractive index of the CPs used in that work [161] as compared to PS [122].) Also in 2017, slightly larger CP microspheres were produced (4 - 11 μm diameter) and used to sense acetone vapour [162]. Both of these examples demonstrated relatively small microspheres, as the rigid CP backbones tend to prevent their formation into large, smooth spherical structures [163].

To conclude, this introduction summarised some of the important concepts directly applicable to the rest of this thesis. After an initial description of the whispering gallery modes in spherical resonators, I moved to a brief overview of polymers, conjugated polymers, and organic dyes. The luminescence and quenching mechanisms were outlined in order to illustrate some of the challenges in the fabrication of lasing microspheres made from these materials.

2 Experimental Methods

2.1 Making microspheres

Over the course of this work, microspheres were fabricated in three different ways, which are detailed below.

2.1.1 Glass microspheres

Glass microspheres can be made by melting and then tapering one end of an optical fibre to form a microsphere attached to a fibre by a glass stem. Such microspheres are easily manipulated and can be dip-coated with fluorescent solutions. The procedure used to make glass microspheres is described as follows:

1. A ~ 10 cm section of standard SMF-28 optical fibre was cut and the jacket and cladding were stripped from it, leaving behind a bare silica fibre with a diameter of $125\ \mu\text{m}$. The bare fibre was rinsed with methanol to remove any dust and debris.
2. The top ~ 1 cm of the bare fibre was taped to a holder so that the rest of the fibre hung down vertically (see Figure 2.1a). A small washer weighing 0.35 g was attached to the bottom of the fibre with 1 cm of sticky tape.
3. This holder was attached to a 3D positioning stage to allow fine control of the fibre's position. The fibre was held vertically such that the midpoint of the fibre was at the focal point of a CO_2 laser ($\lambda=10.6\ \mu\text{m}$, maximum power 10 W), as seen in Figure 2.1b.
4. A flashlight was positioned 40 cm in front of the fibre and turned on, and a webcam was positioned behind a 10 X objective lens which was 1 cm behind the fibre, so that a magnified image of the fibre was displayed on a computer screen. This set-up is shown in Figure 2.2.

5. The duty cycle of the CO₂ laser was turned up to 20-30% of maximum, corresponding to a power sufficient to soften the fibre. As the fibre softened, the weight at the end of the fibre caused the softened section to stretch and thin to a diameter of about 10-20 μm. The 3D positioning stage was used to move the fibre upwards and fabricate a ~2 cm long section of thinned fibre, as shown in Figure 2.1c.
6. The duty cycle of the CO₂ laser was turned up to about 60-70% of maximum. At this power, the glass fibre melted and the bottom section fell off due to the attached weight (see Figure 2.1d).
7. The melted glass at the bottom of the tapered section formed a sphere by surface tension, as shown in Figure 2.1e. The fibre was then moved slowly down and the microsphere grew in size as more of the tapered section was melted.
8. The laser was turned off when the microsphere was attached to the fibre by a thin neck, as shown in Figure 2.1f.

The end result was a microsphere of diameter 50-60 μm which was attached to a glass fibre via a narrow neck as shown in Figure 2.3. The neck needed to be thick enough to support the microsphere without being too fragile, but thin enough to optically isolate the microsphere from the fibre. The size of the microsphere formed by this method could be controlled by making the tapered section longer or shorter in step 5 - a longer section contains more glass and leads to a bigger sphere.

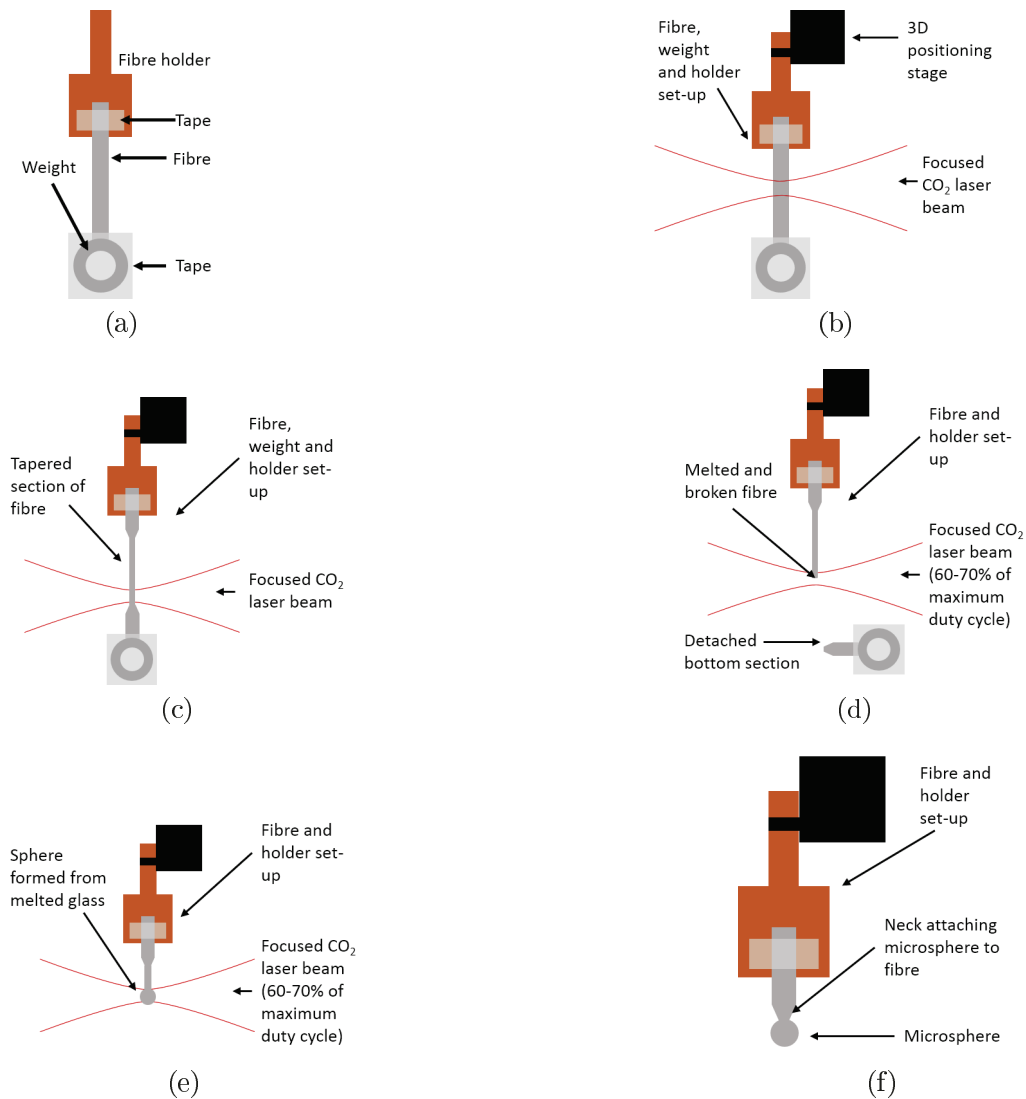


Figure 2.1: Diagrams of the process used to make glass microspheres. (a) A weight is attached to the bottom of the fibre, which itself is attached with tape to the fibre holder. (b) The fibre holder is attached to a 3D positioning stage and the fibre is placed at the focus of a CO₂ laser. (c) As the fibre is moved upwards, it melts and a tapered section forms. (d) The laser power is increased until the fibre breaks. (e) A sphere forms from the melted glass. (f) The fibre is moved downwards and the sphere increases in size; this continues until the sphere is attached to the fibre by a thin neck.

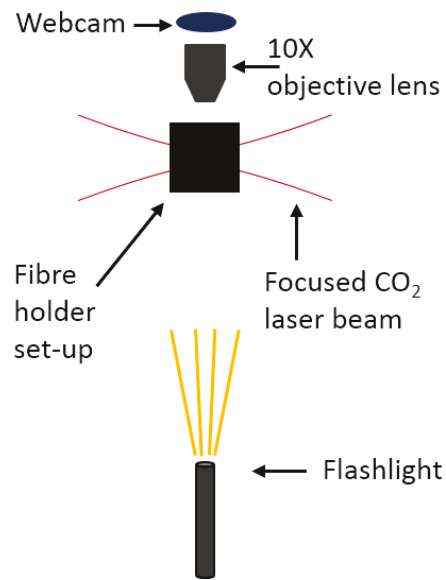


Figure 2.2: Top-down view of set-up.

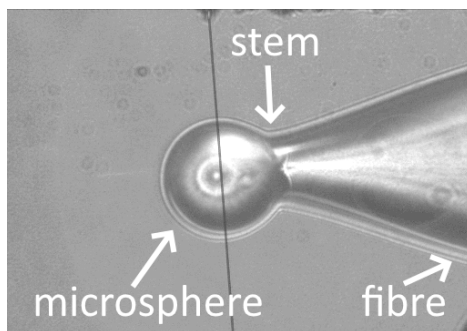


Figure 2.3: Optical microscope image of a glass microsphere of diameter ~ 50 μm . The black line is the entrance slit of the spectrometer.

2.1.2 Polymer coatings on glass microspheres

After fabricating the glass microspheres, they were then coated with a dye-doped polymer. The dye used was rhodamine 610 (R610), which was chosen due to its high quantum efficiency (QE) [128] and its solubility in both methanol and water. For the polymer matrix we chose poly(hexamethylene biguanide) (PHMB) which is also soluble in water.

The PHMB was supplied as a 20% weight/volume solution in water. To concentrate the solution to 40% wt/vol, a small vial of 20% PHMB was left exposed to air for \sim 24 hours until half the volume of water had evaporated. The higher concentration was required to produce a uniform coating on the microsphere. R610 was then dissolved in the 40% PHMB solution at a concentration of 10 mM.

The bare glass microspheres were first rinsed in methanol to remove any dust and were then dipped into the solution of 10 mM R610 dissolved in 40% PHMB in water. After being retracted from the solution, the microspheres were held vertically in air for 15 minutes to allow the water to evaporate, leaving behind a solid film of PHMB with R610 dispersed in it.

Rhodamine dyes are subject to photobleaching by oxidation [164] so a protective layer of poly(methylmethacrylate) (PMMA) was added by dipping the R610/PHMB-coated microsphere into a 5% by weight solution of PMMA in 1,4-dioxane. The initial R610/PHMB layer was unaffected by this second dip-coating as PHMB and R610 are insoluble in 1,4-dioxane. The same drying procedure was followed and the end result was a glass microsphere coated in an inner layer of R610/PHMB and a protective top layer of PMMA.

2.1.3 Conjugated polymer microspheres - emulsification method

Conjugated polymer microspheres were fabricated with an oil-in-water emulsification method. Oil-in-water emulsification refers to mixing a small amount of hydrophobic solution into an aqueous solution and stirring. Upon

stirring, the hydrophobic solution forms spherical droplets within the aqueous solution, which is referred to as the continuous phase [65].

A surfactant was added to the aqueous solution to stabilise the liquid droplets, *i.e.*, prevent them from coalescing. Surfactants are amphiphilic molecules which collect at the droplet interface, with the hydrophobic part of the molecule in contact with the oily droplet, and the hydrophilic part in the aqueous solution [165]. Surfactants can be ionic, in which case charge repulsion keeps the liquid droplets apart [166], or steric, in which case steric hindrance prevents coalescence [167]. The higher the surfactant concentration, the more complete the protective layer is around the oily droplet and the less chance there is of droplets coalescing. In our work, we used poly(vinyl acetate) (PVA) - chemical formula $[-\text{CH}_2\text{CHOH-}]_n$ - which is a steric stabiliser. The structure of the polymer droplets with PVA surrounding them is illustrated in Figure 2.4.

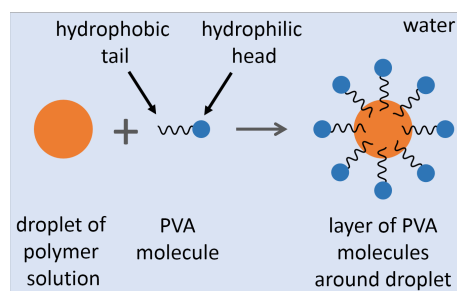


Figure 2.4: Diagram of PVA forming a layer around a droplet of polymer dissolved in chloroform, all in water.

To form solid microspheres from liquid droplets in the emulsion, the liquid droplets must be a solution of solute dissolved in solvent, and solvent evaporation must take place. In my work, the solvent was chloroform and I used three different conjugated polymers which were fabricated at the Technical University of Munich using methods described in the following papers and supporting information. The three conjugated polymers were: red: poly[2-methoxy-5-(2-ethylhexyloxy)-1,4-phenylene-vinylene], MEH-PPV);

green: suggested IUPAC name poly-((1E,1'E-(2,5-bis(2-ethylhexyloxy)-1,4-phenylene)bis(ethene-2,1-diyl))bis(2,5-dimethoxybenzene)-4,4'-diyl), EH-P(PVPVP); and blue: poly[2-methoxy-5-(2-ethylhexyloxy)-p-phenylene], MEH-PPP.

The first step in solvent evaporation is diffusion of the solvent from the liquid droplets into the aqueous phase. The solvent then diffuses through the aqueous phase to evaporate at the water-air interface at the top of the beaker. As the solvent diffuses out of the liquid spheres, the concentration of the remaining solution increases and the spheres become more viscous. The more solvent evaporates, the smaller and more viscous the droplets become, until all the solvent has diffused out and only solid microspheres remain, dispersed in aqueous solution [168].

The solvent evaporation step is often slow as the hydrophobic solvent is not soluble in water, and thus the rate of diffusion into the aqueous phase is low. This rate can be increased by the addition of another liquid, in which the solvent is more soluble, into the aqueous phase. The rate of diffusion of the solvent into the aqueous phase will then increase and sphere solidification will be faster. As this work uses chloroform as the solvent, which is immiscible with water [169], 1-propanol was added to the aqueous phase. Chloroform is miscible with 1-propanol [169] so the addition of 1-propanol should decrease the sphere solidification time.

The procedure used to make solid conjugated polymer microspheres using the oil-in-water emulsification method was then as follows:

1. PVA, M_w 13,000-23,000, 98% hydrolysed, was dissolved in deionised (DI) water at a concentration of 5% by weight. 10 mL of PVA/water solution was added to a small vial and stirred at 400 rpm. This stirring speed was used throughout the rest of the procedure.
2. 0.5 mL of 1-propanol was added to the PVA solution and stirred for 1 minute to ensure complete mixing.

3. The CP was dissolved in chloroform at a concentration of 20 mg/mL and was loaded into a 3 mL Becton Dickinson syringe with a 30 gauge needle. The syringe was then attached to a syringe pump to ensure that the CP solution could be delivered into the PVA solution at a controlled rate.
4. 15 cm of 30 gauge PTFE tubing was attached to the needle. The open end of the tubing was inserted into the PVA/water/propanol solution, about 1 cm above the stirrer bar. The syringe pump was set to pump the CP solution into the aqueous solution at a rate of 0.5 mL/min, for a total time of 1 minute.
5. The resulting dispersion of CP droplets in aqueous solution was stirred for 30 minutes, after which time all the chloroform had evaporated.
6. The stirrer bar was removed. The dispersion was left for about 1 hour so that the solid CP spheres settled at the bottom of the vial. To rinse the PVA off the spheres, the PVA/water solution was pipetted out and replaced with DI water. To ensure that all PVA was removed, this rinsing procedure was repeated 3 times, resulting in a dispersion of CP spheres in DI water.

2.1.4 Conjugated polymer microspheres - microfluidics method

To achieve size control of the CP microspheres, a simple microfluidics method was developed. In microfluidics, two immiscible solutions are carried in two separate microchannels which meet at a junction. At the junction, droplets of one of the solutions (the “dispersed phase”) form inside a continuous flow of the other solution (the “continuous phase”), and the two phases flow together as shown in Figure 2.5. The size of the droplets formed depends on the flow rates of both phases and the size of microchannels used.

The microchannels were made of two capillaries which met at a T-junction (see Figure 2.6). One capillary was circular in cross-section with an inner

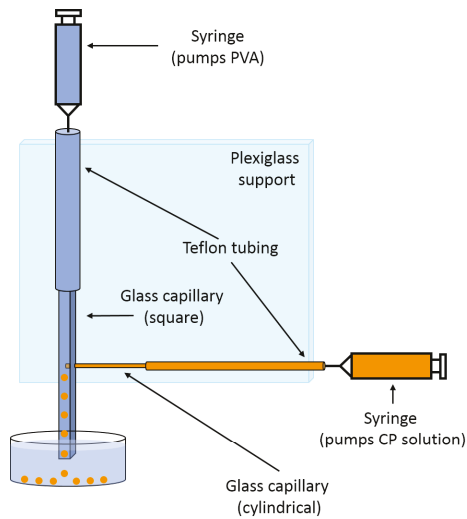


Figure 2.5: Diagram of experimental set up.

diameter of $100\ \mu\text{m}$ and an outer diameter of $140\ \mu\text{m}$. The other capillary was square in cross-section, with an inner diameter of $300\ \mu\text{m}$ and an outer diameter of $600\ \mu\text{m}$. In the square capillary, a hole of diameter $160\ \mu\text{m}$ was drilled (using a drill press and a #96 carbide drill bit) in the centre of one wall. The cylindrical capillary was then inserted into this hole to create the T-junction and was glued in place using Norland Optical 76, a UV-curable adhesive. The two capillaries were then glued to a sheet of plexiglass to keep them secure and prevent any movement.

Teflon tubing (Cole-Parmer, AWG #30) was then glued to the open end of the cylindrical capillary, and more Teflon tubing (Cole-Parmer, AWG #20) to one end of the square capillary. The tubing was also attached to the plexiglass sheet in multiple places so that if any tension was applied to the tubing during experiments, it would not pull on either capillary and potentially break them. The tubing was required to enable pumping of the two solutions using a syringe pump, syringe (3 mL plastic Becton Dickinson), and needle (27G and 19G), as the needle could not be directly inserted into the capillary. Finally, the sheet of plexiglass was mounted vertically so that the square capillary

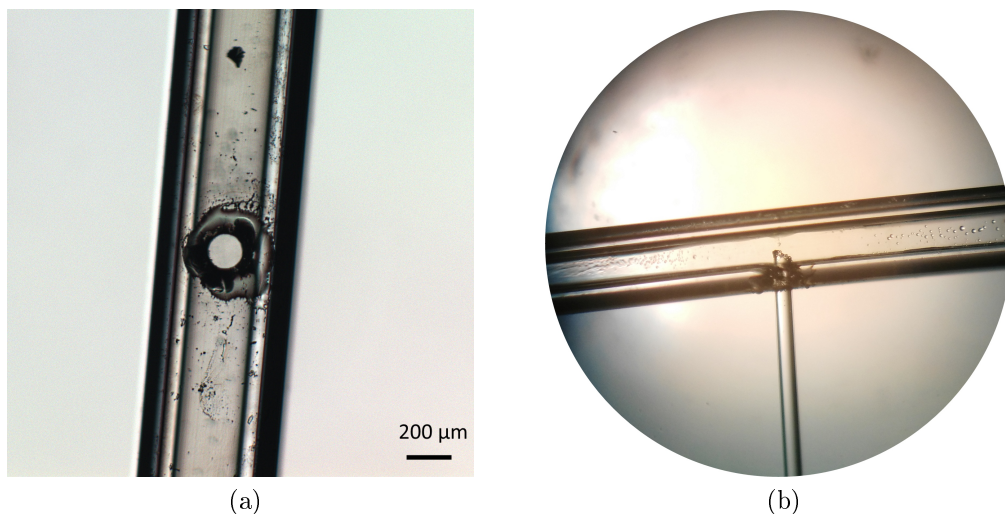


Figure 2.6: (a) Photograph of a square capillary after the hole was drilled into the centre of one face. (b) Photograph of a circular capillary inserted into a square capillary, before glue was applied.

was also vertical, and its output pointing downwards, enabling collection of the droplets into a flat-bottomed glass beaker below.

The continuous phase was a solution of 5% by weight of PVA in water, with 1-propanol added at 5% by volume. The dispersed phase was a solution of conjugated polymer - either MEH-PPV, EH-P(PVPVP), or MEH-PPP, depending on the desired microspheres - in chloroform. These solutions were each loaded into a syringe, which was attached to the Teflon tubing and controlled by the syringe pump. In addition, 60 mL of the PVA-propanol-water mixture was put into the glass beaker. The beaker was placed below the output of the microfluidics system and raised using a lab jack until the output tip of the square capillary was about 2 mm below the surface of the PVA-propanol-water mixture (see Figure 2.5).

The PVA-propanol-water mixture in the syringe was pumped through the tubing first, until it was flowing out of the output capillary into the beaker. Then the CP solution was pumped through the tubing. The order of these

two steps is important; I observed that when the CP solution was instead pumped before the PVA-water-propanol mixture, the CP solution did not break up into uniform sized droplets. Rather, it formed ~ 1 cm long extended droplets inside the square capillary and made large spheres of varying sizes when in the beaker. Additionally, the CP solution stuck to the walls of the glass capillary if the PVA-propanol-water solution was not already flowing.

After 15 minutes of flowing the two solutions, the syringe pump controlling the CP solution was stopped first, then the syringe pump controlling the PVA-propanol-water solution was stopped. The beaker was carefully transferred to a flat surface and left for 48 hours to let the microspheres solidify. The solid microspheres were then removed with a glass pipette and placed in a vial. Some PVA-propanol-water solution was necessarily transferred as well. After the microspheres had settled at the bottom of the vial, this PVA solution was withdrawn with a pipette and replaced with DI water. This rinsing process was repeated 3 times to ensure that the PVA was completely removed and could not stick to the surface of the microspheres.

2.2 Fluorescence spectroscopy

Various lasers and LEDs were used for fluorescence measurements, depending on the polymer or laser dye to be excited. The lasers and their specifications are listed below; the appropriate laser was chosen for each experiment based on the fluorophore absorption spectrum.

- Nitrogen laser, pulsed, 337 nm, average power ~ 1 mW, 3 - 20 Hz variable repetition rate, ~ 1 ns pulse duration
- Alphas laser, pulsed, 405 nm, average power ~ 0.5 mW, 20 MHz maximum repetition rate, ~ 40 ps pulse duration
- Pulsed dye laser, 500 nm, average (maximum) power ~ 1 mW, 3 - 20 Hz repetition rate, ~ 1 ns pulse duration

- Continuous-wave diode laser, 532 nm, power 5 mW
- LED, 365 nm, variable power
- LED, 405 nm, variable power

2.2.1 Spectral Imaging

For fluorescence measurements of single microspheres, light from a laser or LED was loosely focused onto the microsphere and the fluorescence was collected through a 20X objective lens with a numerical aperture of 0.40. A Santa Barbara Instruments Group SGS imaging spectrograph was used to collect spatial and spectral images. In this system, a slit mirror is used to perform simultaneous imaging and spectroscopy, such that the light from a single pixel in the image could be sent for spectral analysis. For analysing WGM spectra, light scattered from the equator of the microsphere was chosen for analysis since the WGM mode field is strongest at these locations.

Wavelength calibration of the collected images was performed by taking a spectral image of a neon calibration lamp and interpolating a pixel-to-wavelength calibration based on the known wavelengths of the calibration lamp (see Figure 2.7). No intensity calibration was performed when studying WGMs because they are narrow spectral features.

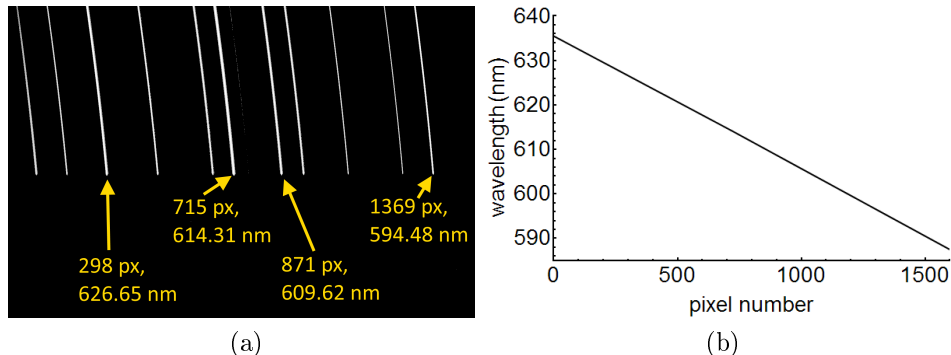


Figure 2.7: (a) Spectral image of lines from a neon calibration lamp, labelled with their pixel values and known wavelength in nm. (b) The calibration curve (line) obtained from the calibration spectral image.

2.2.2 Solution-based fluorescence and absorption measurements

To measure solution fluorescence, the solutions were put into a 3 mL fused-quartz cuvette which was held in a 3D printed cuvette holder. A laser was shone through free space onto one face of the cuvette. Fluorescence was then collected by an optical fibre which was connected to an Ocean Optics spectrometer. An appropriate long pass filter was used to block the laser light and allow only the emitted fluorescence into the spectrometer. Ocean Optics spectrometers are wavelength calibrated at the time of manufacture so only an intensity calibration is necessary. This is done by firstly taking a dark spectrum, then taking a known reference spectrum, and storing both in the Spectra Suite software used for these measurements. The software automatically subtracts the dark spectrum and applies the appropriate intensity correction to spectra that are taken following this calibration. In the case of a blackbody reference, the intensity correction is given by $I_\lambda = P_\lambda(\lambda, T) \frac{I_{S,\lambda} - I_{D,\lambda}}{I_{R,\lambda} - I_{D,\lambda}}$, where I_λ is the intensity at wavelength λ , the subscripts S , R and D refer to sample, reference and dark respectively, and the intensity of the blackbody reference spectrum at temperature T is given by the Planck radiation law $P_\lambda(\lambda, T) = \frac{2hc^2}{\lambda^5} \frac{1}{e^{hc/(\lambda k_b T)} - 1}$.

Absorption measurements of dyes and polymers were taken using the same 3 mL fused-quartz cuvette filled with solution. Firstly, a blank spectrum was taken: a deuterium-tungsten lamp was shone through an optical fibre onto a cuvette containing only the solvent, and the spectrum of the lamp after it had passed through the solvent was recorded. Next, the cuvette was filled with the dye or polymer dissolved in the same solvent. The lamp was again shone through the optical fibre onto the cuvette, and the spectrum after it had passed through the dye or polymer solution was recorded. Any intensity differences between the blank spectrum (solvent only) and sample spectrum (solvent with dissolved dye or polymer) are due to absorption of the dye or polymer. The absorbance of the dye or polymer at a wavelength λ is given by $A(\lambda) = \log_{10} \left(\frac{I_{B,\lambda} - I_{D,\lambda}}{I_{S,\lambda} - I_{D,\lambda}} \right)$, where I_λ is the intensity at wavelength λ and the subscripts B , D and S refer to blank, dark and sample respectively.

2.2.3 Fluorescence Lifetimes

Fluorescence lifetimes were collected using an Alphas pico-power pulsed laser at a wavelength of 405 nm. The pulse lengths are nominally 40 ps. The luminescence was collected with an optical fibre, passed through a longpass filter, and then entered a Becker-Hickl HPM-150 PMT (response time ~ 150 ps). 5-metre fibres were used to minimise reflection-related interferences in the decay traces. The repetition rate was typically 1 MHz but slightly higher rates were sometimes used in order to decrease the data collection time. Care was taken to use low signal intensities in order to avoid “pile-up” and other sources of distortion in the decay traces.

3 Whispering Gallery Mode structure in polymer-coated lasing microspheres

A slightly different version of this chapter was published in Journal of the Optical Society of America B, 2017, 34, 2140 by K. Gardner, Y. Zhi, L. Tan, S. Lane, Y.-F. Xiao, and A. Meldrum. In the version presented in this thesis, all instances of “Fig.” have been changed to “Figure” for consistency with the rest of the thesis, and the references have been renumbered also for consistency.

Abstract

Whispering gallery modes (WGMs) are frequently observed in the emission spectrum of a fluorophore coupled to a dielectric microsphere. If the fluorophore is excited strongly enough the WGMs can become lasing modes, producing a much higher signal-to-noise ratio and higher Q-factors. These favourable properties have led to recent demonstrations of biochemical sensing with lasing WGMs; however, as we show here, the underlying cavity structure that leads to lasing can be highly complicated and the lasing spectrum can result from a large number of closely spaced or overlapping modes. In silica spheres coated with a dye-doped polymer bilayer, hints of underlying complexity are already indicated by the skewed shape of the fluorescence WGMs. Under lasing conditions, a more complicated structure was observed with Q-factors over 10 times higher than observed in fluorescence, while transmission measurements showed a dense forest of resonances due to m -order degeneracy breaking from a lack of perfect spherical symmetry. Lasing preferentially occurs at wavelengths where these modes tended to be most densely spaced. The tapered part of the fibre to which the microsphere is attached can also have a strong effect on the lasing spectrum, leading to significant differences between the fluorescence and lasing resonances.

3.1 Introduction

The whispering gallery modes (WGMs) of single dielectric microspheres have been investigated in recent years for chemical and biosensing applications [58, 60, 61, 170, 171], and they also demonstrate sensitive force [62], temperature [63], and humidity [64] sensing capability. The best biochemical sensitivities, down to the level of single molecules [172] or nanoparticles [173], have been reported by evanescently coupling light from a tunable laser into a microsphere via a tapered fibre or prism and measuring the transmission spectrum. However, evanescent coupling usually requires a rather high level of experimental precision and is nontrivial to fabricate and package.

Fluorescent microspheres do not require an evanescent coupling apparatus. If pumped above their lasing threshold, they can provide high Q-factors and an excellent signal-to-noise ratio [174]. Lasing microspheres are often made from freestanding polymer spheres [38], but these are difficult to manipulate individually (methods include attaching a freestanding microsphere into the holes of a microstructured optical fibre [175] or the use of optical tweezers to position a sphere for analysis [176]). One of the more common methods is to melt the tip of an optical fibre to form a glass microsphere that can be manipulated and positioned close to the necessary sensor elements.

In the case of fluorescent glass microspheres, previous results have sometimes shown rather uniform fluorescence WGMs [177], whereas other results have reported a much more complicated emission spectrum [178]. Similarly complicated patterns have been reported from lasing WGMs as well [38]. While many different types of fluorescent and lasing microspheres have been produced (*e.g.*, see [17, 124]), there are few previous studies that have examined the mode structure by a combination of evanescent coupling, fluorescence, and lasing investigations over a wide spectral bandwidth corresponding to several times the free spectral range.

By forming a lasing microsphere on the end of a tapered fibre that can be easily manipulated, we compare all three types of WGM spectra from a

single glass microsphere coated with a lasing gain medium. Indeed, a key question has to do with the fundamental cavity mode structure that leads to WGM lasing in solid microspheres that lack perfect spherical symmetry, which may often be the case for spheres fabricated by fibre taper melting and re-solidification. The results may thus be of significance for the origin of lasing in microspheres generally, since the lasing behaviour can be expected to depend quite sensitively on the fundamental mode structure.

3.2 Experiment

Samples were fabricated by stripping the jacket from conventional SMF-28 optical fibre, cleaning it with acetone and methanol, and then melting the end of the fibre using a CO₂ laser. This method produced spheres of the order of 60 μm in diameter that remained attached to the tapered fibre through a connecting neck. The spheres were then dipped vertically into a solution consisting of 10 mM rhodamine 610 dissolved in 40% by weight of polyhexamethylene biguanide (PHMB) in water. The microspheres were then retracted from the solution and held for about 15 min in the same position to allow the solvent to evaporate. The spheres were subsequently dipped into a solution of 5% by weight polymethyl methacrylate (PMMA) in dissolved in 1,4-dioxane, followed by the same drying procedure. The PMMA layer was intended to protect the active dye-doped PHMB layer against oxidation/aging and also to reduce the photobleaching of the dye during lasing experiments. The two polymers and their solutions are insoluble and can thus lead to the formation of a stable bilayer.

Fluorescence WGMs were excited using a 5 mW continuous wave 532 nm diode laser loosely focused onto the microsphere. The microsphere lasing was excited by using a dye laser operated at a wavelength of 550 nm. This laser has an ~ 800 ps pulse duration and a 20 Hz repetition rate, yielding an average (maximum) power of ~ 1 mW (50 $\mu\text{J}/\text{pulse}$) that could be focused to an area about 10 times larger than the microsphere cross section. Lower

powers were obtained by first passing the beam through an adjustable neutral density filter. The emission was collected through a 20x objective with a numerical aperture of 0.40 and sent to a Santa Barbara Instruments Group imaging spectrometer for analysis. A diagram of the experimental setup is shown in Figure 3.1; essentially the image lands on the slit such that only the part of the image that intersects the slit is analysed (using the imaging spectrograph).

Finally, bare cavity measurements were taken in a different setup, in which a fibre tapered to $\sim 1 \mu\text{m}$ in diameter was brought in contact with the microsphere. A Newfocus TLB-6700 laser (150 kHz bandwidth) was used to scan between 635 and 639 nm, which is a range of wavelengths over which the polymer-embedded R610 dye was able to lase. In this way, the cavity resonances could be directly compared to the spectra observed in the fluorescence and lasing modes.

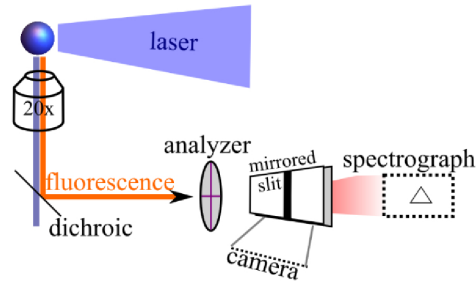


Figure 3.1: Schematic of the optical setup used to collect and analyse the microsphere fluorescence (using a CW laser) or lasing (using a pulsed laser). The image lands on the slit and the part that goes through it enters the spectrometer.

3.3 Simulation

The experimental results were compared to theory by employing a unified multilayer transfer matrix model developed in detail in [179], from which the

emitted power spectrum can be calculated. This model establishes the structural resonances via matching boundary conditions for a multilayered sphere and calculates the wavelength dependence of the radiated power assuming a randomly oriented dipole layer, as in the current experiments. We use four layers: silica, PHMB, PMMA, and air, with refractive indices of 1.45, 1.56 [180], 1.49, and 1.00, respectively.

As will be discussed further below, the tapered region of the fibre from which the spheres were fabricated was found to play a significant role in the lasing spectra. This situation was modelled using a 3D finite-element time-domain simulation that was effectively a miniature version of the actual sample shape. The grid spacing was 30 nm and perfectly matched layers were employed to eliminate reflections at the simulation boundaries. A dipole emitter was placed either partway inside the taper region or on the sphere equator, and the detector was placed on the microsphere equator. The calculations were run for up to 20 ps simulation time, depending on the resolution required. To complete the simulation in a reasonable period, the dimensions of the simulated sample were shrunk by a factor of 10 while retaining the original shape and wavelengths; this miniaturisation shortened the computation time to ~ 8 h on a 16 core 2.8 GHz desktop PC. The smaller size also leads to a wider free spectral range (FSR) and lower-Q modes, but it was believed to adequately illustrate the general effects of the taper and neck on the optical resonances. It provided good qualitative agreement with the experiment, but cannot be thought of as an exact replication of the experiment due to the necessity to shrink the scale, as required to achieve feasible computation time.

3.4 Results and Discussion

The bilayer-coated microspheres appeared fairly smooth and uniform (Figure 3.2); however, some texturing was observed on the surface. These features had a scale of ~ 5 nm and were not present on a plain uncoated sphere. The

polymer layers appeared thickest and least uniform in the region of the taper leading to the neck, probably due to the vertical dipping and drying technique during which there is viscous flow due to gravity. This would cause an excess of material to become trapped as it flows toward the “pinched” region at the taper-sphere contact leading to a buildup of polymer in these regions.

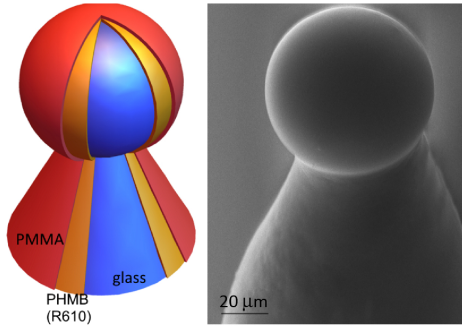


Figure 3.2: Schematic (left) and secondary electron SEM image (right) of the multilayered microsphere.

Under CW excitation, the spheres showed an orange luminescence featuring a set of broad peaks with Q-factors of ~ 500 (Figure 3.3, upper curve). The free spectral range of these WGMs was ~ 1.4 nm, in agreement with the above-mentioned model calculations for a sphere of this size and with the ray approximation given by $\Delta\lambda = \lambda^2/(2\pi aN) = 1.34$ nm for a uniform refractive index of 1.45 (where a is the sphere radius and N is its index of refraction). Under pulsed excitation, however, a set of much narrower modes occurred throughout the spectrum. These modes appeared above a threshold of typically $20 \mu\text{J}/\text{pulse}$ (Figure 3.3, inset). They were more intense than the fluorescence WGMs that occurred under CW pumping for an equivalent average pump power. We interpret these as lasing modes (lower spectrum in Figure 3.3). Rather than a 1:1 correspondence between fluorescence and lasing WGMs, a group of at least several lasing lines appeared to be present

within each fluorescence WGM and the greater spectral density of lasing lines extended in some places outside the main fluorescence peak.

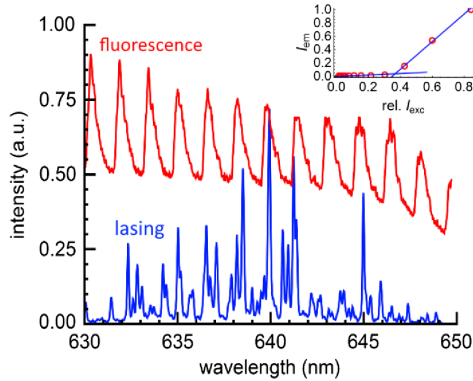


Figure 3.3: TE-polarised fluorescence (red) and lasing (blue) spectra from a bilayer coated microsphere. The data has been scaled for clarity. Normalised to equivalent average pump powers the WGM spectrum was typically much weaker than the lasing one. The lasing threshold behaviour is shown in the inset. The excitation intensities (I_{ex}) were obtained using a variable neutral density filter (the transmission percentages are on the x-axis), with the highest value corresponding to $\sim 50 \mu\text{J}/\text{pulse}$.

The transmission spectrum from a double-coated sphere (Figure 3.4) shows a dense forest of modes with Q-factors of $\sim 10^5$ (Figure 3.4). These modes merge into broader dips in regions indicated by the shaded vertical lines. An uncoated microsphere measured under the same conditions gave Q-factors up to 10^7 , indicating that Q is limited by the sphere structure (*e.g.*, roughness-induced scattering from the polymer films) and not to the presence of the taper. These modes are far too spectrally dense to be different radial (n) or angular (l) mode orders. Instead, we believe the density of modes is due primarily to degeneracy breaking of the m -orders (*i.e.*, modes with a polar component) due to slight ellipticity of the sphere [19]. Even a

small ellipticity can drastically increase the number of polar resonances that appear in a microsphere transmission spectrum [181].

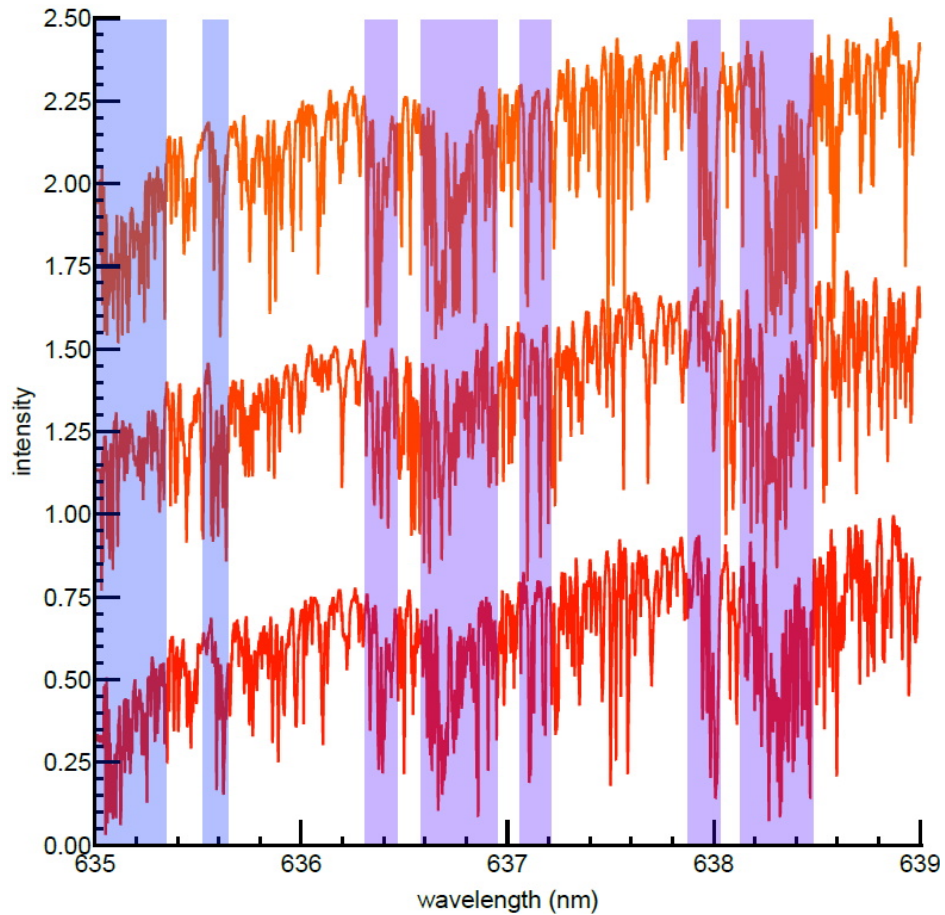


Figure 3.4: Transmission spectra taken for three different taper polarisations, showing differences in individual modes but the same overall pattern of larger combined “depressions” at ~ 635.1 , 636.6 , and 638.1 nm. The shaded blue lines highlight regions where the modes converged into the larger “dips” in each spectrum. The data are offset for clarity.

In order to investigate the effect of the transmission polarisation, a fibre polariser was used to vary the polarisation in the taper. Some individual modes did change intensity as a result, but the overall features of the spectrum remained similar for every measurement (Figure 3.4). The same type of behaviour was observed for five different spheres that were tested—in all cases there was a forest of modes merging into broader dips that corresponded reasonably well with the fluorescence WGMs, as discussed below, with local differences but showing large scale similarities for various transmission polarisations.

We next focus on an analysis of the emission resonances within the range of 635–639 nm (Figure 3.5), corresponding to the scan range over which the bare cavity modes could be measured. To avoid additional spectral complication we focus on the TE polarisation (electric field perpendicular to the WGM propagation plane) since these modes produced more intense emission, and compare the result to the calculated mode spectrum for a 33.5 μm diameter sphere with a polymer bilayer, corresponding to the observed microsphere size. Since there was no practicable way to determine the polymer bilayer thickness for the model calculations, we used an estimate of 100 nm per layer based on the thickness observed for the same polymer-solvent solutions dried inside capillaries with a channel radius similar to that of the microsphere, since these could be cleaved and cross sectioned for scanning electron microscopy (SEM) (while approximate, this method should at least give an order of magnitude estimate). The dominant calculated resonances are the first-order radial modes ($n = 1$) with an FSR of ~ 1.4 nm [Figure 3.5(a)].

The emissions (fluorescence and lasing) and the cold-cavity spectra are compared in Figure 3.5(b). The fluorescence peaks were skewed toward longer wavelengths, with apparent Q-factors of ~ 500 (as discussed in more detail later). In contrast, lasing within each (apparently) individual fluorescence WGM was split into several lasing modes with Q-factors near 6000, possibly limited by the spectrometer resolution. The lasing modes occurred at various

locations within the broader fluorescence WGMs. The cold-cavity spectrum is strikingly different again, showing a vast number of closely spaced modes with Q-factors of the order of 10^5 . Although the sphere and fibre taper were in contact and hence overcoupled, the Q-factor did not appear to be limited by taper-induced losses since a plain sphere demonstrated Q-factors up to 10^7 by this method. The deepest transmission dips occurred in groups near where one observes the main fluorescence WGMs. It is clear that not every one of this huge number of modes is lasing (otherwise there would be lasing modes literally all over the spectrum), and that the lasing appears to occur predominately where the overlapping mode “troughs” are deepest.

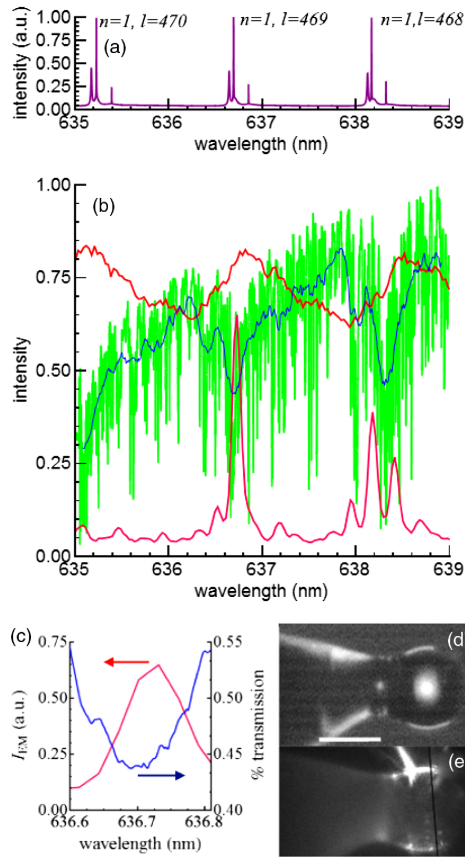


Figure 3.5: (a) Simulated mode structure for an $\sim 67 \mu\text{m}$ diameter microsphere with a polymer bilayer coating. (b) TE-polarised fluorescence and lasing WGMs (upper and lower red lines, offset for clarity), and a cold-cavity transmission spectrum (green) showing also a moving average (blue). (c) Zoom-in between 636.6 and 636.8 nm, showing the transmission spectrum (blue; moving average) and corresponding lasing mode (red). (d, e) Transmitted and lasing images of the same microsphere. The scale bar is $50 \mu\text{m}$.

The spectral density of resonances implies that the spectra are not simply the result of numerous overlapping radial mode orders [181]. Indeed, the simulation shows that only the first three radial orders are likely to appear

for an emissive layer on spheres of this size; the higher-order mode fields overlap only weakly with the dipole layer. Instead, the dense mode structure is likely due to symmetry breaking resulting from a slight eccentricity causing extensive m -order degeneracy lifting. For small distortion the eccentricity is given by $e \approx l \cdot \Delta\nu/\nu = 0.003$ for a typical mode spacing of ~ 4 pm as observed in the transmission spectra. While such a small eccentricity is impossible to observe in the images (it yields radii differences close to one pixel) the effect is enhanced by the relatively low cold-cavity Q-factors of $\sim 10^5$, which causes extensive mode overlap.

Over the course of the experiments, some samples were aged in air for a period of several weeks to a few months. For these samples the fluorescence WGMs were weaker and a higher excitation power was required to observe lasing. However, the lasing and fluorescence spectra were quite different from one another in all of the aged samples (Figure 3.6). In each case, the spectrum was taken with the entrance slit near the equator of the microsphere (see Figure 3.1; the image of the microsphere is projected onto the entrance slit and aligned with it by moving the microscope stage). Whereas the fluorescence spectra were mainly the same as in fresh samples, albeit weaker, there were significantly more lasing WGMs. The lasing modes were still fairly evenly spaced, but the apparent FSR was much smaller than the original one.

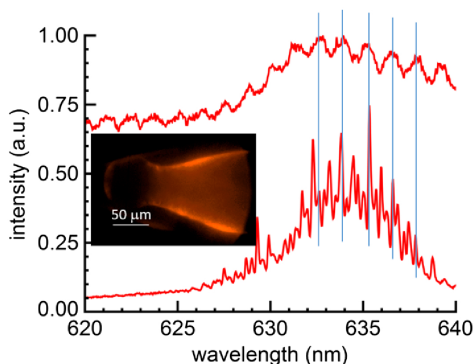


Figure 3.6: TE-polarised fluorescence and lasing spectra taken from the equator of the microsphere whose lasing image is shown in the inset. The lasing modes are more numerous and closely spaced than the fluorescence peaks.

The origin of this effect appears to be related to the origin of the lasing itself. In fresh samples, lasing mainly originated within the microsphere, which appeared very bright [Figure 3.5(e)]; whereas in the aged samples under pulsed excitation the emission came dominantly from the taper region where the polymer films were thickest (Figure 3.6, inset). The dye molecules embedded within thicker polymer films along the taper are better protected from oxidation; thus, only this region may be able to exceed the lasing threshold after the sample has been exposed to air for a prolonged period.

The geometry of the samples can be approximated as a cone merged into a sphere, as represented in Figure 3.2(a). Whereas in fresh samples lasing comes mainly from the spherical part leading to standard spherical WGMs, in aged samples, although the measurement is still near the equator of the sphere, the lasing originates on the cone. Previous investigations of conical fluorescence [182] or lasing modes [183] or “optical vortices” [184, 185] are relatively few. Here the situation is further complicated because the shape consists of a conical region leading to an injector (the neck) and then a spherical end region.

Several different effects can play a role in the emission spectrum. First, one can expect “replicas” or oscillations of each original mode to form a continuum of overlapping modes at shorter wavelengths in conical or tapered structures, depending on the cone angle [186]. Second, the conical modes have a nonzero axial component implying that these modes contain a mixture of TE (axial) and TM (radial) polarisations. Third, the injection of radiation into the interior region of the spherical part could preferentially excite WGMs of higher radial (or polar) orders in the microsphere, leading to the development of resonances that did not appear when the radiation was emitted at the outer edges.

In order to test these possibilities, a set of three-dimensional finite difference time domain (FDTD) simulations were carried out on a cone-sphere shape identical to that illustrated in Figure 3.2(a) closely matching the real sample. A dipole emitter producing a 20 fs sinusoidal pulse centred at 770 nm was placed in the cone region (this is not equivalent to lasing but rather mimics broadband fluorescence). The results showed that the combined structure does indeed have a much more complicated mode structure, with a higher density of main resonances (Figure 3.7), not too different from the experimental observations.

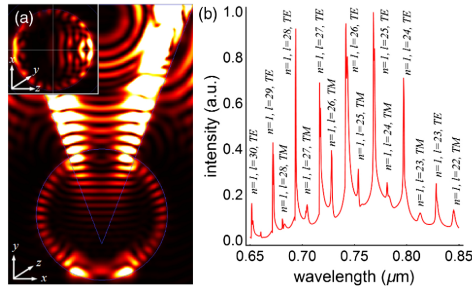


Figure 3.7: FDTD resonance power image and spectrum for a TM polarised (radial E-field) cone emitter with the detector at the sphere’s equator. In (a) the intensity of a TE mode (axial E-field) with $n = 1$ and $l = 26$ is shown in a plane that bisects the structure. The two strong antinodes at the tip of the sphere were frequently observed in samples showing this type of lasing spectrum. The inset depicts the same resonance in a cross section through the equator of the sphere. The TE-polarised spectrum is shown in (b); although the resonances are TE-polarised, smaller peaks are also observed at the expected TM resonant wavelengths.

Two main effects were observed in the simulations. First, consistent with the experimental observations, the mode spectrum observed at the sphere equator was denser for an emitter placed in the taper, as compared to the standard WGM structure obtained for the same emitter on the sphere’s equator. For a TM-polarised emitter, there was a TE-polarised emission component at the sphere equator (and vice versa), with resonances at wavelengths corresponding to both polarisations [Figure 3.7(b)]. This results in a greater number of observable emission modes. Second, the polar resonances (*i.e.*, modes with $m \neq l$) were much more effectively excited via the cone injection [Figure 3.7(a) shows one example]. Since the transmission data indicate a significant amount of degeneracy-breaking for modes of the same n and l but different m , the resulting emission spectra feature polar modes that are more efficiently excited via the taper.

The lasing of silica microspheres pumped through the taper (cone) appears to be controlled by the underlying cavity mode structure to produce unusually complicated lasing spectra. The lasing cone modes have to be coupled into the sphere, and only those that overlap with a sphere resonance should appear strongly in the equatorial emission spectrum. Since, as shown earlier, the sphere resonances consist of a set of overlapping modes forming broad dips in the transmission spectrum, it seems likely that at least some of the densely spaced cone modes will overlap with these sphere resonances. The idea was further tested by measuring the polarisation of the lasing modes, since according to the simulation the cone modes should contain both TE and TM components. In fact, there was a distinct lack of spectral features unique to any one lasing polarisation. Although somewhat weaker, all the lasing features in the TM spectra overlapped with those in the TE spectra, suggesting that, like in the simulation, the lasing resonances coupled into the sphere from the cone region contain components of both polarisations.

3.5 Interpretation and analysis

We have so far observed that the fluorescence, lasing, and transmission spectra in single microspheres are quite different. We believe these differences are enhanced due to a lack of perfect spherical symmetry and the interfering effects of the tapered part of the fibre attached to the microsphere. Here, we address some of the physical mechanisms that can be responsible for such significant spectral differences associated with fluorescence, lasing, and transmission WGM measurements.

The width of the fluorescence WGMs, as compared to the much narrower transmission modes, could be related to two effects: (i) the spectrometer resolution, and (ii) the emitter spectral bandwidth. In the first case, all the observed transmission modes would be emitting but are narrower than the linewidth resolution of the spectrometer, causing the sharp WGMs to appear “smeared” into a single broad peak. The spectrometer response function

was therefore obtained by measuring a HeCd gas laser line ($\Delta\nu \sim 3$ GHz). By fitting a Gaussian peak to the measured laser line, the half-width was found to be 63 pm (46 GHz), leading to a maximum resolvable Q-factor of $\sim 10^4$, which is lower than the measured transmission Q of $\sim 10^5$ but much higher than the observed fluorescence Q of ~ 500 , suggesting that these low observed Q-factors are not limited by the spectrometer response. To confirm this, we also performed a convolution of the transmission spectrum with the spectrometer response function to simulate the fluorescence spectrum; while clearly “smoothed,” there are still obvious resonances with Q close to the predicted value of 10^4 (Figure 3.8), *i.e.*, much higher than the observed fluorescence peaks.

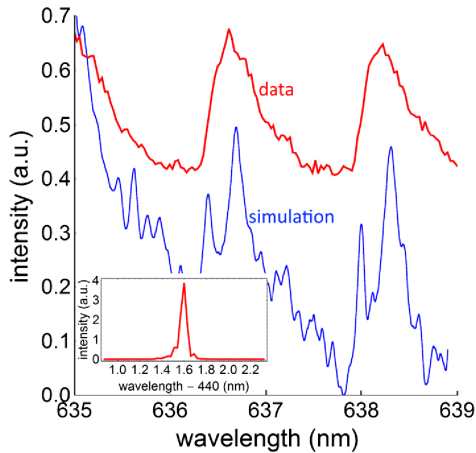


Figure 3.8: Simulated fluorescence spectrum (blue line) obtained by convolving the spectral system response (inset) with the transmission data shown in Figure 3.5. The experimental data (red line) is shown for comparison.

Thus we now examine the second option. The fluorescence spectrum is fundamentally related to the overlap of the cold cavity density of states and the spectral bandwidth of the emitters. Generally, the cavity decay rate is calculated via Fermi’s golden rule, with the assumption of a narrow emitter

linewidth. However, the luminescence Q-factor can be approximated with a more general form given by $Q_{lum} = \lambda_{cav}/(\Delta\lambda_{cav} + \Delta\lambda_{em})$, where $\Delta\lambda_{cav}$ is the cavity linewidth and $\Delta\lambda_{em}$ is the emitter's homogeneous linewidth [187]. Thus, although often assumed to be negligible in comparison to the cavity linewidth, the emitter linewidth can affect the measured fluorescence Q-factors. Rhodamine dyes are reported to have homogeneous linewidths of $\sim 100 \text{ cm}^{-1}$ (12 meV) at room temperature [188], which is in fact quite wide compared to the bare cavity linewidths measured here and would yield Q of ~ 100 according to the formula given above. Although this is even lower than the experimentally measured values, our estimate of 500 is in fact only an upper limit due to mode overlap (in other words, we measure the apparent half-width of significantly overlapping peaks). Thus, based on previous measurements of the homogeneous linewidths, the wide fluorescence peaks are caused mainly by the overlap of inherently low-Q modes, in which the fluorescence Q-factor appears limited by the emitter linewidth.

The lasing spectrum, on the other hand, is a complicated function of the spectral gain bandwidth (due to inhomogeneous broadening), saturation, mode competition, and the Q-factor of the available cavity modes. The observed lasing linewidths are quite possibly limited by the spectrometer response function, given an observed Q of ~ 6000 and a calculated upper resolution limit of $\sim 10,000$ with various uncertainties in the measurements. Given this limitation, it is not straightforward to show which specific cavity modes are responsible for the lasing, but we do observe that the lasing seems to predominate where the modes are most closely spaced, forming somewhat broader dips in the overall transmission spectrum. The preponderance of overlapping modes in these regions suggests that mode coupling may reduce the lasing threshold. There has been relatively little investigation of the effect of spectral and spatial mode overlap on lasing thresholds in WGM resonators, although it was shown theoretically that the formation of a lasing

“supermode” due to extensive mode overlap can lower the threshold [189], consistent with the observations reported here.

Finally, the observed lasing or fluorescence mode structure can depend to some degree on the measurement method [190, 191]; for example, the preferred polarisation has been shown to depend on the taper-sphere separation distance. Also, a taper preferentially excites modes in the equatorial plane, whereas in the emission situation all polar modes are excited at once [191]. Similar effects may exist here, since the transmission measurements were taken via an overcoupled fibre taper whereas the fluorescence and lasing spectra did not use any near-field coupling device.

However, it appears unlikely that the differences between the transmission and emission spectra could be due to the presence of the taper in the one case only. According to the above cited investigations, the mode structure should be simpler in the transmission measurement since fewer polar modes (*i.e.*, those with $m \neq 1$) are likely to be excited. In contrast, we observed a far more complicated spectrum for that case, due to the higher spectral resolution and the effect of the emitter linewidth on the emission spectra, as discussed previously. Furthermore, the emission spectra were analysed from the equatorial part of the microsphere specifically, similar to the transmission measurements. Although an even greater number of nondegenerate polar modes could contribute to the broad fluorescence WGMs than might technically appear in the transmission spectra, this effect does not affect the main conclusions concerning the significant differences in the three types of WGM spectra.

3.6 Conclusion

The fluorescence, lasing, and cold-cavity mode structures of a layered microsphere are quite different from one another. In fluorescence, one observes a fairly normal, periodic, WGM mode structure, although fairly weak, with low Q-factors and with a long-wavelength skewing that hints at a more com-

plicated underlying structure. In the lasing spectrum, modes that appeared as single WGMs in fluorescence appeared instead as clusters of several lasing resonances with Q-factors that were higher by an order of magnitude, possibly limited by the spectrometer resolution. The bare cavity structure measured by coupling light into the microsphere from a fibre taper was vastly more complicated, consisting of dense clusters of resonances with Q-factors of $\sim 10^5$. The fluorescence WGMs occurred where the cold-cavity mode structure was overall the densest and deepest, with the narrowest, deepest clusters often corresponding to a lasing mode. Thus, lasing preferentially occurs at wavelengths in which there are an abundance of closely spaced or overlapping cavity modes.

In microlasers with perfect spherical symmetry, these effects should not be observed and the lasing should consist of a simple structure that corresponds closely to the fluorescence resonances, both of which would represent the fundamental cavity mode structure. However, slight eccentricity caused by the fabrication process coupled with unavoidable irregularities in the coating result in a highly complicated cavity spectrum consisting of an abundance of densely spaced modes. When the emitter is located on the taper leading to the sphere, the observed mode structure near the sphere equator shows a completely different periodicity mainly related to the higher-order polar modes of both polarisations, which are much more effectively excited by light propagating down the taper and coupling into the sphere through the neck region. All of these effects combine to produce a far more complicated lasing spectrum than would be expected on the basis of a simple spherical symmetry.

4 Ultrabright Fluorescent and Lasing Microspheres from a Conjugated Polymer

*A slightly different version of this chapter was published in *Advanced Functional Materials*, 2018, 28, 1802759 by K. Gardner, M. Aghajamali, S. Vagin, J. Pille, W. Morrish, J. G. C. Veinot, B. Rieger, and A. Meldrum. In the version presented in this thesis, the references have been renumbered for consistency with the rest of the thesis.*

Abstract

Fluorescent microspheres are used for biomarkers, assay substrates, chemical diagnostics, flow cytometry, and biological imaging. These applications demand the highest fluorescence intensity achievable; however, concentration quenching limits the amount of dye that can be practically incorporated in conventional fluorescent microspheres. Conjugated polymers (CPs) can be less susceptible to concentration quenching, suggesting that they can be excellent candidates for a new class of light-emitting microspheres. Due to their long-chain-conjugated backbone, however, CPs can be resistant to forming smoothly curved or spherical structures. Here, strongly fluorescent CP microspheres as large as 100 μm in diameter are synthesised. Whispering gallery modes (WGMs) appear in the fluorescence spectra, and the microspheres show clear evidence of lasing above a threshold pump intensity. These conjugated polymer beads are up to 50 times larger than CP microspheres obtained by other methods, and they exceed the emission intensity of conventional fluorescent microspheres by more than an order of magnitude.

4.1 Introduction

Conjugated polymers (CPs) represent an especially attractive platform for fluorescent or even lasing devices [73, 118]. They feature semiconductor-like

optical and electronic properties due to the π - π^* energy gap that arises from the alternating single and double bonds in the carbon chain backbone. Although nonradiative decay pathways associated with interchain interactions are known to occur [192], these effects can be minimised in coiled chains to the point where CPs may be less susceptible to concentration quenching effects than organic chromophores [140]. They can have reasonably high photoluminescence quantum efficiencies [193, 194] and an appreciable Stokes shift, which limits reabsorption losses [117]. CPs are being widely explored for applications in organic light-emitting diodes (OLEDs) [195, 196], flexible electronics [86, 88], and plastic lasers [126]. CP microspheres would present a new class of luminescent or lasing polymer microspheres with potentially superior light-emission properties. Creating smooth spherical structures from conjugated polymers can be difficult, however, because the formation of grain boundaries through local ordering or crystallisation can often lead to fibrous or rough surfaces [159]. For this reason, there are no examples of large (*i.e.*, $>5\ \mu\text{m}$) CP microspheres. Only extremely small structures have been formed in a few cases of specifically designed CPs so far [160, 163], which significantly limits their potential applications. A viable route toward the fabrication of CP microspheres that can compete with those formed from conventional dye-doped polymers has not yet been achieved.

The polyphenylene-vinylene polymers (PPVs), including bis-alkoxy-substituted derivatives such as poly (2-methoxy-5-(2-ethylhexyloxy)-1,4-phenylene vinylene (MEH-PPV), can feature good mechanical stability [197] and can form reasonably smooth flat films when deposited by solution-based processes [198, 199]. In particular, the bis-alkoxy-substituted PPVs can be rendered soluble in a wide variety of organic solvents by an appropriate choice of the side groups. These polymers are well-suited for optical applications in solid state and in solution, and have the benefit of easy synthesis (*e.g.*, via the Gilch route [200]). They can be pumped both electrically and optically [201] and have been shown to lase in Fabry-Pérot cavities [202] and

distributed feedback lasers [203, 204]. They are one of the few classes of CPs able to produce $\approx 2 \mu\text{m}$ spherical structures [205] and can form smooth coatings on optical fibres [206]. Therefore, the PPVs appear to offer a viable route toward the formation of ultrabright CP microspheres with a significant potential for applications.

4.2 Results and discussion

MEH-PPV polymers of different molecular weights were prepared, as described in the Experimental Section. They yielded NMR spectra fully consistent with the MEH-PPV molecular structure (Figure 4.6, Supporting Information). The polymer appeared orange when dissolved in chloroform or reddish-orange when cast into a solid film. The fluorescence lifetime was ≈ 230 ps for MEH-PPV in solid and in the solution (Figure 4.1, inset), the latter of which also had an absolute quantum efficiency of 30%. In chloroform solution, the absorption peaked at 490 nm and the main fluorescence maximum was at 600 nm, with shoulders at 630 and 670 nm. The absorption and fluorescence spectra from the solid and dissolved MEH-PPV samples were similar, although the solid films yielded slightly redshifted fluorescence spectrum and a somewhat wider overall absorbance (Figure 4.1). This triple-peaked spectrum is attributed to vibronic states whose energy separation is consistent with the C=C stretching mode, while the observed fluorescence redshift upon solidification is due to polarisation interactions in adjacent chains [207]. At least some of the extended red tail is probably due to interchain interactions that are thought to form excimer or “exciplex” states, which are more prevalent in the solid form [207].

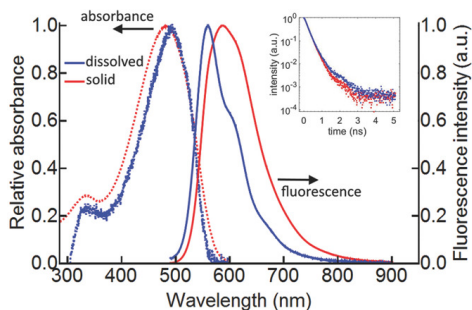


Figure 4.1: Normalised absorbance and fluorescence spectra for solid MEH-PPV films (red) and for MEH-PPV dissolved in toluene (blue). The inset shows the fluorescence decays using the same colour scheme. The very slight “bump” at ≈ 2 ns is probably a weak afterpulse from the PMT.

After the basic structural and luminescence properties of the MEH-PPV were determined, a modified nonsolvent emulsion method was used to produce large, smooth MEH-PPV microspheres suitable for lasing (see the Experimental Section). Forming high-quality MEH-PPV microspheres presents a fine balance between the molecular weight (M_N), solvent type, polymer concentration, emulsifier concentration, and polymer solubility. If M_N is too high, the polymer solubility in common organic solvents including chloroform is low, resulting in small, poorly formed microspheres. By using a relatively low molecular weight PPV ($M_N \approx 30 \text{ kg mol}^{-1}$, dispersity ≈ 4.7) obtained through a repeated cracking procedure (Figure 4.7, Supporting Information), and a high concentration of polyvinyl alcohol with propanol as a secondary surfactant in the aqueous phase, we generated smooth PPV microspheres from 5 to more than 100 μm in diameter. The surface roughness was much smaller than the wavelength of light (Figure 4.8, Supporting Information), except when there was significant subsurface structure, as discussed further below.

As synthesised, the microspheres ranged in diameter from 5 to 30 μm but microspheres as large as 100 μm (Figure 4.2a) could be produced by

changing the synthesis procedures slightly (specifically, without the addition of the secondary surfactant or by slowing the stirring speed). After filtering through a mesh net, the distribution narrowed such that most particles were in the range from 10 to 20 μm (Figure 4.2d,f), representing the largest CP microspheres reported so far. The tendency of some smaller microspheres to stick to the larger ones widened the size distribution beyond what would be expected from the filter sizes used after synthesis, although we found that this problem can be lessened by the addition of a salt such as sodium dodecylsulfate.

Different applications impose different requirements on the microsphere structure. For optical applications, and especially for lasing, the microspheres must be smooth and defect-free in the near-surface region. For drug delivery, hollow or porous microspheres are more desirable. Many of the as-synthesised MEH-PPV microspheres were smooth but a fraction appeared to feature small craters or depressions, suggesting the possibility of subsurface structure. Combined helium ion microscopy and focused ion beam cutting was therefore used to slice open the MEH-PPV microspheres and examine their interior structure. Depending on the preparation parameters, one can synthesise solid CP microspheres with fairly little internal structure (Figure 4.2b) or highly porous microspheres riddled with a network of voids (Figure 4.2c). One of the key parameters for reducing void production was the use of the secondary surfactant. The secondary surfactant (propanol) also prevented the formation of the largest microspheres, possibly by restricting the merger of liquid droplets during stirring. Control over the porosity could allow CP microspheres to be tailored for either optical or biomedical applications that could capitalise on the structural, chemical, or luminescent properties of conjugated polymers.

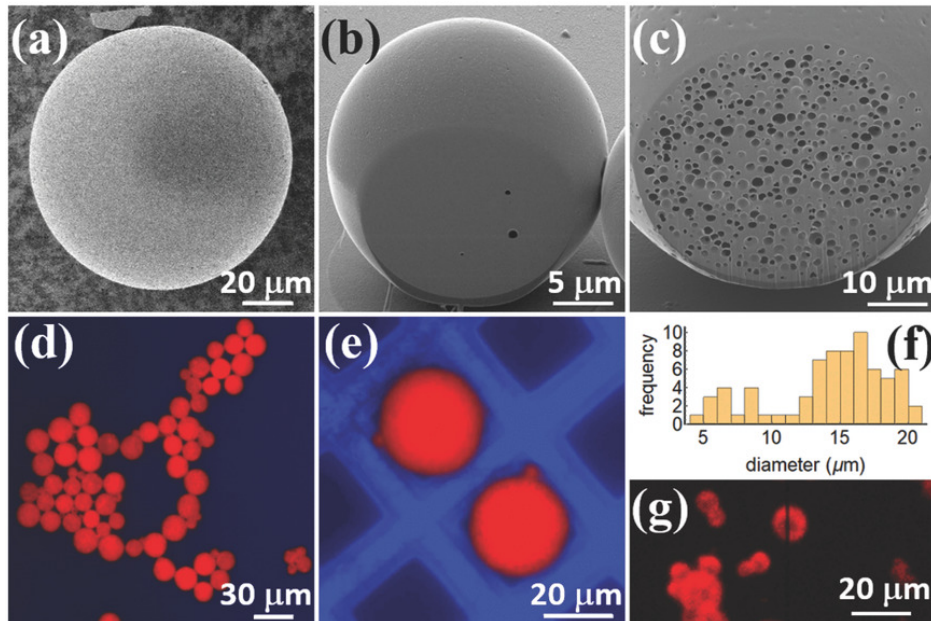


Figure 4.2: a) Helium ion microscopy image of a single gold-coated MEH-PPV microsphere over $100\ \mu\text{m}$ in diameter. b) Scanning helium microscope of a single sphere which has been sliced open by a focused ion beam. Three small voids are visible in the interior. c) A single large MEH-PPV microsphere containing a network of interpenetrating pores. d) Fluorescence image showing a small group of MEH-PPV microspheres. The violet background is from the excitation LED. e) Fluorescence image of two MEH-PPV microspheres of nearly the same size, resting in adjacent grid holes. Some smaller microspheres escaped the filtering procedure by sticking to the larger ones. f) Size distribution histogram for the sample shown in (d). The mean diameter is $14.3\ \mu\text{m}$. g) Fluorescence image showing a group of lasing MEH-PPV microspheres. The spectrometer entrance slit is visible running through the centre of the image.

The MEH-PPV microspheres emit an orange-red fluorescence under continuous-wave (CW) excitation with a laser or LED. Fluorescence spectra taken from individual low-porosity microspheres showed a set of whispering gallery modes (WGMs) with Q-factors of 200–300 (Figure 4.3a). The free

spectral range (FSR) from a 6.6 μm diameter microsphere was 11.1 nm, in reasonable agreement with the prediction of 11.0 nm given by the ray optics approximation, where $\Delta\lambda = \frac{\lambda^2}{2\pi a N}$, with $N = 1.8$ [208], $\lambda = 640$ nm, and $a = 3.3$ μm , confirming that these are WGMs. The WGM spectra are reminiscent of those from silica microspheres with dye-doped polymer coatings [209], suggesting that the underlying mode structure may consist of a complicated set of non-degenerate modes that arise from imperfect sphericity. The appearance of WGMs in the fluorescence spectra is important because it enables applications in a variety of sensing technologies, including biosensing [60, 61], chemical sensing [12], or the sensing of physical properties like pressure [62] and temperature [210].

Under 500 nm pulsed excitation, the emission behaviour changed drastically. Above a threshold excitation irradiance, a sharp line narrowing (Figure 4.3a) was observed, with individual modes yielding Q-factors up to 5000. The appearance of narrow, high-Q modes above a threshold is widely understood to indicate the onset of lasing [211, 212]. Lasing was observed in a number of spheres with diameters from 6 to 32 μm (Figure 4.3d). The lasing modes reversibly blueshifted with increasing pump power (Figure 4.3c). Most polymers have negative thermo-optic coefficients [213, 214]; assuming this is the case for MEH-PPV as well, then the lasing mode blueshift is due to a slight temperature increase upon higher-power excitation. By estimating the beam diameter from microscope images, measuring the average power, and using the nominal pump pulse length of 1 ns, we estimate a typical threshold pulse irradiance of 5.0×10^6 Wcm^{-2} . The lasing WGMs were found to be transverse magnetic (TM) polarised; indeed, only the TM modes (*i.e.*, electric field either radial or tangential to the equator) can propagate into the microscope objective, due to the geometry of the setup (see the Experimental Section).

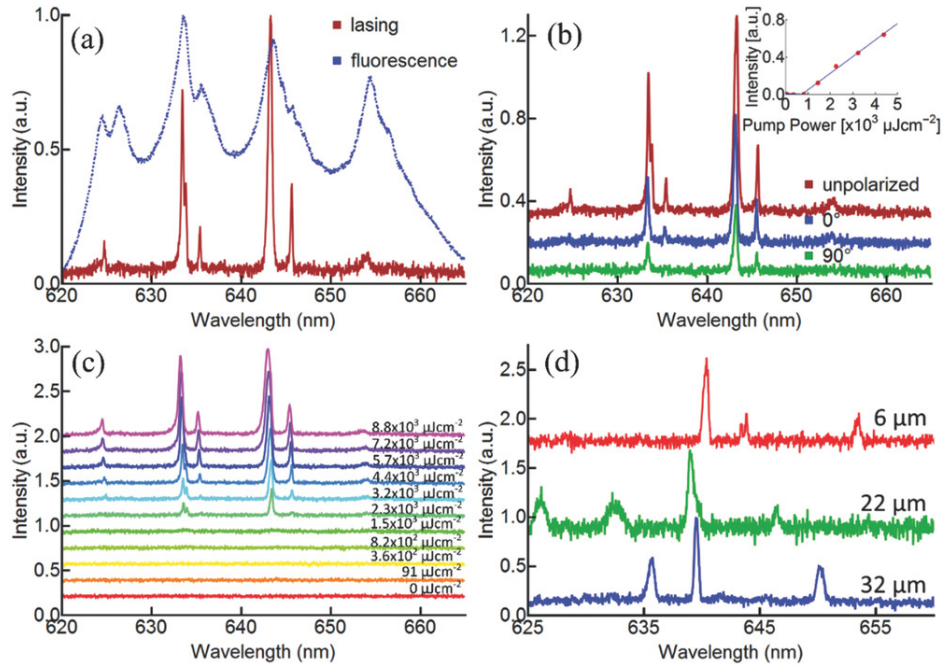


Figure 4.3: a) TM-polarised fluorescence spectrum (blue dashed line) from a single 6.6 μm diameter microsphere, showing a complicated whispering gallery mode structure. When pumped above a threshold of $\approx 800 \mu\text{J cm}^{-2}$, the WGMs narrowed drastically, suggesting the onset of lasing. b) Polarisation effects in the lasing WGMs. Only the tangential and radial electric fields can propagate to the microscope objective, which is consistent with the change only in intensity but not in lasing wavelength as the polariser is rotated through 90° . The threshold behaviour of the lasing is shown in the inset. c) Evolution of the emission spectrum as a function of pump power. d) Lasing spectra for microspheres of differing diameters.

The fluorescence intensities of conventional dye-doped polystyrene microspheres were compared with that of the CP microbeads synthesised in this work. For this purpose, a set of nominally 7.5 μm diameter “Suncoast Yellow” fluorescent microspheres were purchased from a commercial supplier [215]. These microspheres have emission and absorption spectra similar to those of MEH-PPV and therefore allow for a reasonably direct comparison. The

fluorescence of the similarly sized MEH-PPV microspheres was ≈ 20 times more intense than the commercial microspheres, using either a 532 nm CW laser or a 405 nm LED as the excitation source (Figure 4.4). Under pulsed excitation conditions, the MEH-PPV beads lased, whereas no sign of lasing was evident from any of the dye-doped microspheres. Thus, CP microspheres show outstanding fluorescence properties that exceed the capability of standard fluorescent microbeads.

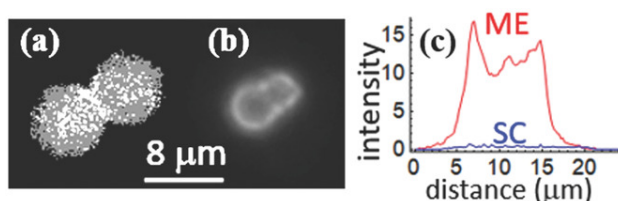


Figure 4.4: a,b) Grayscale images of a pair of Suncoast Yellow (SC) and slightly smaller MEH-PPV (ME) microspheres, respectively. Both the images were taken using a 405 nm LED operated under identical conditions. The image intensities have been scaled differently; otherwise the SC spheres are nearly impossible to see. c) Raw (unscaled) intensity profiles taken across the sphere pairs. The ME spheres, although smaller, have an integrated intensity 23 times greater than that of the SC microspheres.

There are currently some limiting factors as well. First, dry MEH-PPV microspheres show evidence of photobleaching and colour change under CW excitation in air and a gradual bleaching over several minutes under lasing conditions. This effect was slower in water or methanol and negligible when the spheres were encapsulated in resin, suggesting that this issue is likely due to photo-oxidation, which can be minimised by methods such as surface coating. Second, prolonged storage in air or water gradually degraded the ability of the microspheres to lase. Samples kept in water at room temperature for several weeks still appeared bright in fluorescence but the lasing threshold increased and ultimately exceeded the damage threshold, at which

point lasing could no longer be induced. Finally, void formation needs to be kept to a minimum in order to preserve sufficiently high-quality WGMs for lasing to occur.

4.3 Conclusion

In summary, large, smooth MEH-PPV microspheres up to 100 μm in diameter were synthesised by a modified nonsolvent emulsification method. This is nearly two orders of magnitude larger than the only previously known spherical CP structures, bringing conjugated polymer microspheres into the size regime of conventional fluorescent beads. The microspheres can be made minimally to highly porous, depending on the processing parameters and microsphere size. The fluorescence intensity was ≈ 20 times higher than that of comparably sized dye-doped polystyrene microspheres, and the MEH-PPV microspheres showed clear indications of lasing above a threshold at which conventional beads indicated no sign of lasing. This presents another advantage over conventional polymer beads, since microsphere lasers are desirable for a variety of sensing applications [122, 124] and possibly for micro-lasers [216, 217]. These results indicate a route toward the development of a new class of ultrahigh-brightness microspheres for diagnostics, imaging, and drug delivery. The methods could be expanded to include other CPs in order to obtain a wider range of emission colours. For these reasons, we believe that conjugated polymer microspheres could in future replace conventional dye-doped microspheres in many optical, biochemical, and sensing applications in which ultrahigh-intensity fluorescence or even lasing is desirable.

4.4 Experimental section

All the solvents and starting materials for synthesis were purchased from commercial sources. Tetrahydrofuran (THF) for MEH-PPV synthesis was purified using M Braun solvent purification system. The synthesis of monomer

precursor and its polymerisation were performed according to a slightly modified version of the recipe reported recently [218]. For polymerisation, method B in ref. [218] was chosen, where the monomer precursor was slowly added into solution of potassium tert-butoxide in THF without any additional chain transfer reagent. Under completely oxygen-free conditions, orange gels were formed which were then transferred into methanol. The precipitate was filtered off and washed by resuspension in methanol several times until the neutral reaction of pH indicator. The air-dried product was poorly soluble in THF, toluene, or chloroform at room temperature.

The polymer was subjected to cracking in toluene as follows: 0.5 g of MEH-PPV was refluxed in 300 mL toluene in an air-open apparatus under protection from light and the aliquots were taken every 24 h for gel permeation chromatography (GPC) analysis of the molecular weight (Figure 4.6, Supporting Information). GPC analysis relative to polystyrene standards was performed on Varian GPC-50 plus chromatograph using PLgel-Mixed-B columns and chloroform as eluent. When the desired molecular weight was achieved, the solution was concentrated on a rotary evaporator, poured into 10 volumes of methanol with vigorous stirring, and isolated by filtration or centrifugation. Finally, ^1H NMR spectra were recorded on Bruker AV III 300 MHz or Bruker AV III HD 500 MHz in deuterated chloroform and the signals were referenced to the residual solvent peak (Figure 4.7, Supporting Information).

Microspheres were fabricated using an oil-in-water (O/W) emulsification method. Poly(vinyl alcohol) (PVA: Mw \approx 13 000–23 000, 98% hydrolysed, Sigma-Aldrich) was used as an emulsifier. A solution of PVA in deionised (DI) water (50 g L^{-1} , 10 mL) was prepared and added to a 20 mL glass vial. While being stirred with a magnetic stir bar at 400 rpm, 0.5 mL of 1-propanol (99.5%, high performance liquid chromatography Grade, Sigma-Aldrich) was added to the PVA solution. The MEH-PPV was dissolved in chloroform (99.8%, Sigma-Aldrich) at a concentration of 20 mg mL^{-1} and

then drawn into a 1 mL syringe. An ≈ 10 cm length of polytetrafluoroethylene tubing with an inner diameter 1.1 mm was attached to the needle and then filled almost to the end with the MEH-PPV solution. The tubing was then submerged in the PVA solution and secured so that the open end was ≈ 0.5 cm above the stirrer bar and close to, but not touching, the side of the vial. The syringe was connected to a syringe pump and 0.5 mL of MEH-PPV solution was dispensed at a rate of 0.5 mL min^{-1} . The tubing was then removed from the solution.

The solution was left to stir for 2 h so that all the chloroform evaporated, eventually leaving solid polymer spheres in an aqueous solution. The PVA was then removed by centrifuging the sphere-PVA solution so that the spheres settled to the bottom of the test tube and the solution on top could be removed and replaced with deionised water. This process was repeated 3 times to be sure that most of the PVA was rinsed off the spheres. For optical experiments, a 20 μL droplet of spheres dispersed in water was dropped onto a quartz slide. The slide was left in air until the water evaporated and only the polymer spheres remained on the slide. The remaining microspheres were stored in the dark in a sealed vial. Size selection was done by filtration in methanol through a set of square-array filters.

The surface of the microspheres was imaged using a helium ion microscope, within which a Ga focused ion beam (FIB) (30 kV) was used to “slice” individual microspheres in order to expose an interior cross-section for imaging. Samples were coated in ≈ 100 nm thick gold before imaging and exposure to the FIB.

Absorption spectroscopy was performed by measuring the transmittance using an Ocean Optics USB 2000 spectrophotometer. Quantum efficiency measurements were made on a home-made integrating sphere setup, using a 405 nm light-emitting diode as the excitation source. Fluorescence imaging and spectroscopy of individual microspheres used a 5 mW continuous-wave 532 nm diode laser loosely focused into the microsphere. Time-resolved ex-

periments used a 405 nm pulsed picosecond laser (Alphas Gmbh) and a Becker & Hickl photomultiplier tube (PMT) with a response time of ≈ 100 ps. For lasing experiments, the excitation was switched to a pulsed dye laser operated at a wavelength of 500 nm, corresponding to the MEH-PPV absorption maximum. This laser has a nominally ≈ 1 ns pulse duration and a 20 Hz repetition rate, with an average (maximum) power of ≈ 1 mW ($50 \mu\text{J}$ per pulse). It was focused to an area of about $3 \times 10^{-4} \text{ cm}^2$. The pulse energy was adjusted using a pair of crossed Glan–Thompson polarisers, where one polariser could be rotated relative to the other. The sphere emission was collected through a $20\times$ objective with a numerical aperture of 0.40 and sent to a Santa Barbara Instruments Group imaging spectrometer for analysis. A diagram of the experimental setup is shown in Figure 4.5.

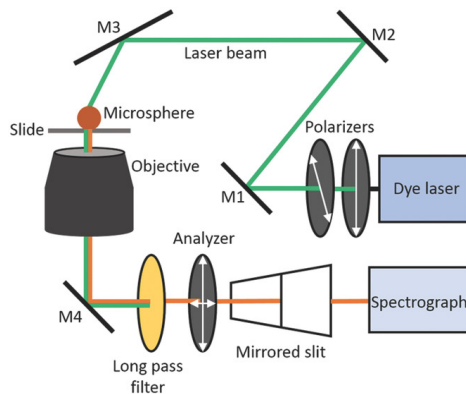


Figure 4.5: Diagram of the optical set up used to excite fluorescence and collect spectra from the microsphere.

4.5 Supplementary information

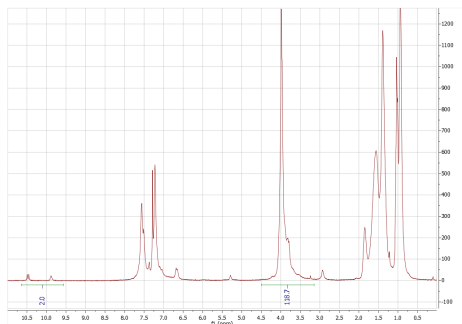


Figure 4.6: Sample ^1H NMR spectra of the MEH-PPV with M_n ca. 11 kg/mol. The signals of the aldehyde groups are clearly seen in the region 9.5 – 11 ppm. Assuming they are end-groups of the polymer chains, an average polymerisation degree of 24 can be calculated, which leads to $M_n =$ ca. 6 kg/mol. The overestimation of molecular weight by GPC measurements is due to the referencing to polystyrene (PS). Whereas PS tends to form a macro-conformation close to a random coil in chloroform solution, MEH-PPV macro-conformation is closer to linear, more like a rigid rod. Thus MEH-PPV macromolecules have lower molecular weight than PS with the same mean hydrodynamic radius. The peak at 5.3 ppm is not common for MEH-PPV and is not observed in the as-synthesised product. It is characteristic of a vic-diol functionality which comes from an unaccomplished cracking reaction (an oxidised but not yet cleaved double bond). This reduces the effective conjugation in the macromolecules and explains a shift of the polymer colour from red to orange-red compared to the samples with higher molecular weight.

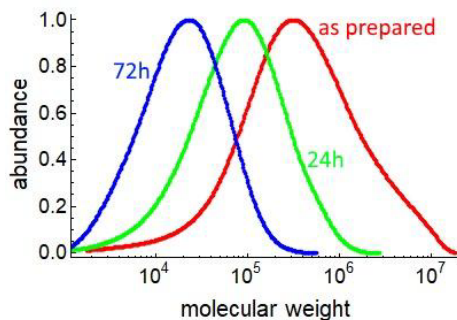


Figure 4.7: Molecular weight distribution measured by gel permeation chromatography (see experimental section) in the as prepared MEH-PPV polymer, and after 24 or 72 hours cracking in toluene. The MEH-PPV as-synthesised has M_n ca. 110 kg/mol and M_w ca. 1000 kg/mol, after 24 hours cracking it yields M_n ca. 30 kg/mol and M_w ca. 140 kg/mol, and after 72 hours cracking: M_n ca. 11 kg/mol and M_w ca. 31 kg/mol. Note that the number-averaged (M_n) and weight-averaged (M_w) molecular weights are distinctly different from the peak values.

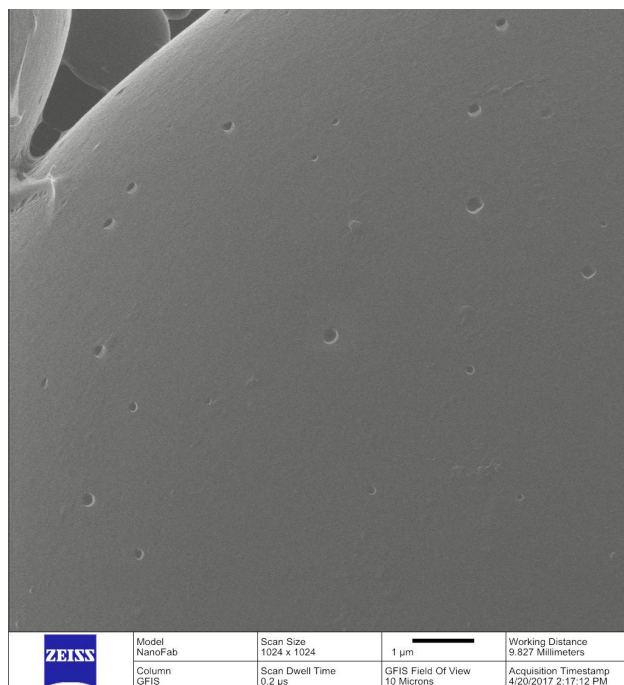


Figure 4.8: High magnification view of an uncoated MEH-PPV microsphere. The field of view is $10\ \mu\text{m} \times 10\ \mu\text{m}$. Some cratering is apparent on the surface, likely due to the subsurface void structure as reported in the main MS. However, with this exception, the surface of the microsphere is much smoother than the wavelength of light and very few irregularities can be observed. Some material, possibly PVA, can be seen to form an attachment to a neighbouring microsphere.

5 Monodisperse arrays of large, high-brightness conjugated polymer microspheres

K. Gardner, L. Zhang, S. Vagin, W. Morrish, P. Tsai, A. Meldrum

This chapter is a preliminary draft of a paper we plan to complete and submit once the COVID-19 pandemic has subsided and we are permitted back in the lab.

5.1 Introduction

Conjugated polymers (CPs) are characterised by a long-chain molecular backbone consisting of alternating single and double carbon bonds. The overlapping p-orbitals result in the formation of the bonding and antibonding orbitals with a characteristic energy gap between them – in other words, CPs are the organic equivalent of a conventional semiconductor [219]. Various sidegroups can be attached to the main CP chain in order to establish specific functionalities or to sterically minimise intra-chain electronic interactions, which otherwise can have significant and often deleterious effects on the electronic or fluorescence properties [207]. CPs are under widespread development for numerous applications, including organic light emitting displays (OLEDs) [220], photovoltaics [221], and sensors [222].

Fluorescent microspheres have extensive applications in biomedicine, including flow cytometry [69], biomedical diagnostics [70], imaging [223], and as visible carriers for drug delivery [66]. They are also used as signallers for contamination and leaks in drilling and other instrumentation [71]. The market associated with these applications for fluorescent microspheres is projected to see significant growth in the next decade [224], with many well-known chemical companies involved in development and sales.

Commercial microspheres are based on a conventional polymer, such as polystyrene or polyethylene, doped with a fluorescent dye. The doping procedure typically involves an entrapment method [225], in which a hydrophobic

dye is placed in a good-solvent bad-solvent mixture along with the pre-made polymer microspheres. The dye diffuses into the microsphere surface as the good solvent evaporates. While this method is widely used and produces high-quality fluorescent microspheres [211], the achievable fluorescence efficiency is limited by concentration quenching, which restricts the entrapped dye concentrations to around 1% in commercial microspheres [226]. In contrast, CP microspheres would have some major advantages, including the key fact that the entire structure is made from an inherently fluorescent polymer without the need for entrapment.

Due to their long-chain conjugated backbone, CPs do not easily form smooth surfaces by conventional microsphere synthesis methods and the resulting structure can depend extensively on the selection of the solvent [207]. Methods used to form CP microspheres include in-situ droplet polymerization [227, 228, 229, 230, 231], vapour diffusion [160, 232], and emulsion mixture techniques [160, 233]. The latter two methods employ the formation of good-solvent droplets hosted in a bad-solvent “continuous phase”. The CPs are dissolved in organic solvents (which are hydrophobic) that form droplets of good solvent in an aqueous (hydrophilic) continuous phase. A surfactant is used to prevent the droplets from merging. Narrow size dispersions require control over the droplet size, which can be achieved by microfluidic methods [234, 235] or specialised step-growth dispersion polymerization processes [228]. While these methods have been successful, the resulting micro-particles tend to be small ($< 5 \mu\text{m}$ in diameter) which limits the potential applications. There have been few investigations of the single-particle or coupled-particle fluorescence behaviour, and few comparisons with conventional dye-doped particles.

Large CP microspheres have not previously been reported, except in one recent study by our group (here, we define “large” as $10 \mu\text{m}$ - $200 \mu\text{m}$ in diameter) [233]. Fluorescent microspheres of this size are important for the development of whispering gallery resonances (*e.g.*, for sensing and lasing ap-

plications in which a high quality factor is required) [32], drug delivery [236], and generally in situations demanding a stronger overall fluorescence intensity. In this work, we demonstrate a simple and accessible microfluidic method to achieve large and highly monodisperse red-, green-, and blue-emitting CP microspheres. The materials start from highly-ordered arrays of monodisperse droplets, which themselves show coupled particle interactions and evidence of lasing. We then follow the evolution of these droplets as the solvent evaporates to leave size-controlled and monodisperse solid CP microspheres up to 100 μm in diameter.

5.2 Results and Discussion

The three conjugated polymers (red: poly[2-methoxy-5-(2-ethylhexyloxy)-1,4-phenylene-vinylene], MEH-PPV); green: suggested IUPAC name poly-((1E,1'E-(2,5-bis(2-ethylhexyloxy)-1,4-phenylene)bis(ethene-2,1-diyl))bis(2,5-dimethoxybenzene)-4,4'-diyl), EH-P(PVPVP); blue: poly[2-methoxy-5-(2-ethylhexyloxy)-p-phenylene], MEH-PPP) were synthesised at the Technical University of Munich, Germany, as described in the Experimental section at the end of this chapter. Their chemical structures are illustrated in Figure 5.1. The molecular weights were measured by gel permeation chromatography; for this work we used $M_N = 45$, $M_W = 200$ for MEH-PPV, $M_N = 7$ kg/mol, $M_W = 15$ kg/mol for EH-P(PVPVP), $M_N = 30$ kg/mol, $M_W = 150$ kg/mol for MEH-PPP. For the green polymer (EH-P(PVPVP)), the values used represent the highest molecular weights that could successfully be synthesised.

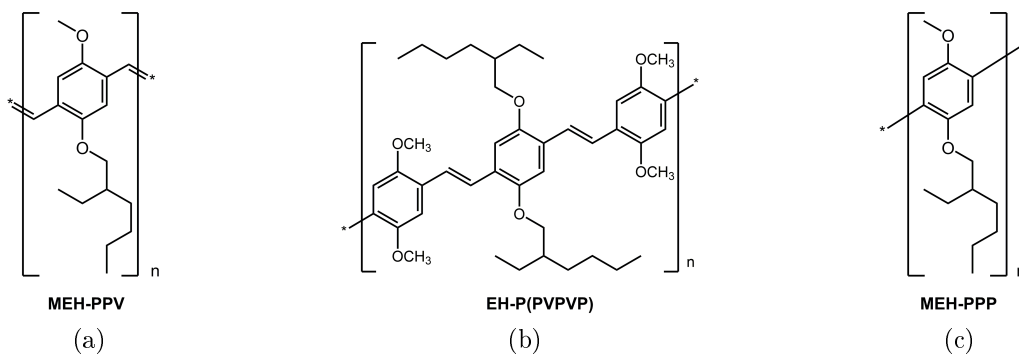


Figure 5.1: Stick diagrams of the three synthesised polymers. (a) MEH-PPV (Red). (b) EH-P(PVPVP) (Green). (c) MEH-PPP (Blue).

Each of the three polymers was strongly fluorescent in chloroform solution. The quantum efficiency was found to be 18%, 41%, and 56% for the red, green, and blue polymer, respectively. Fluorescence measurements of the red and green polymer solutions used 405 nm excitation, which is near the maximum of the absorption band of the green polymer and close to the edge of the red polymer absorption band; measurements of the blue polymer used 352 nm and 363 nm excitation lines, which are near the maximum absorption band of the blue polymer (Figure 5.2). The fluorescence spectrum of MEH-PPP is the narrowest of the three, and peaks at 405 nm with a slight shoulder at 455 nm. The fluorescence spectrum of EH-P(PVPVP) is wider than that of MEH-PPV and peaks at 505 nm with a shoulder at 540 nm. The fluorescence spectrum of MEH-PPV is the widest, peaking at 595 nm with shoulders at 640 nm and 710 nm and a red “tail” extending close to 900 nm.

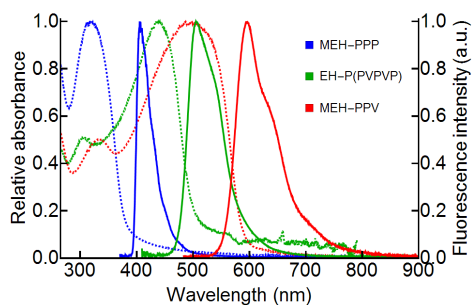


Figure 5.2: Absorption and fluorescence spectra for the three polymers in films. Dashed lines represent absorbance, solid lines represent fluorescence.

Polymer microparticles of each colour were synthesised using a microfluidics method to obtain a uniform droplet size. The setup consisted of a fluidic T-junction in which the polymer solution (20 mg/mL polymer in chloroform) was carried in one channel and a water-PVA-propanol solution was carried in the other channel. At the junction where the two channels met, droplets of the polymer solution formed. These droplets were carried in the water-PVA-propanol mixture, and finally ejected at a rate of ~ 15 Hz into a flat-bottomed beaker containing the same water-PVA-propanol mixture. Owing to the higher density of chloroform compared to water, the droplets sank to the bottom where they spontaneously assembled into a hexagonal close-packed array (Figure 5.3). The droplets were allowed to sit for 48 hours until the chloroform had completely evaporated and solid microspheres were formed.

Each liquid droplet had a diameter of ~ 300 μm and an almost negligible size dispersion (the droplets were all the same size to within ~ 10 pixels in the images; Figure 5.3). The MEH-PPV droplets emitted a bright orange fluorescence and their spectrum was consistent with that of the original solution, peaking at ~ 600 nm and showing the typical triple-peaked spectrum of dissolved MEH-PPV (Figure 5.2). These peaks are often attributed to vibronic levels and interchain interactions that cause the extended red emission [207].

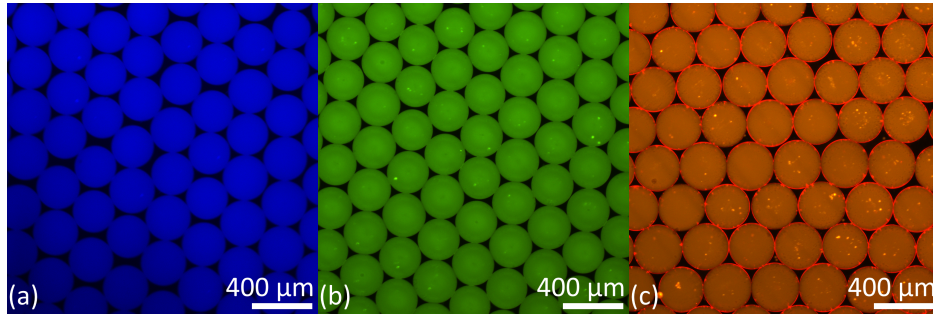


Figure 5.3: Fluorescence images of patterned droplets. (a) MEH-PPP (b) EH-P(PVPVP) (c) MEH-PPV.

The red polymer droplets showed signatures of lasing upon excitation with a 532 nm pulsed laser (Figure 5.4). While we cannot exclude the possibility that the green and blue droplets may also lase, only the red particles can be pumped directly into their absorption band at this excitation wavelength. At low excitation powers only a broad fluorescence typical of MEH-PPV could be observed. However, above a threshold pump power of $\sim 400 \text{ W/cm}^2$, a set of narrow resonances appeared in the long-wavelength part of the background fluorescence spectrum (Figure 5.4). We interpret the simultaneous appearance of these long-wavelength modes and the bright red equatorial band (Figure 5.4a) above a threshold pump power as a probable signature of lasing.

The free spectral range associated with the whispering gallery modes can be estimated from $\Delta\lambda_{FSR} = \lambda^2/(\pi DN)$ where λ is the central wavelength (610 nm), D is the droplet diameter (310 μm), and N is the refractive index ($N = 1.45$ for chloroform) yielding $\Delta\lambda_{FSR} = 0.26 \text{ nm}$ which is just larger than the nominal resolution of the spectrometer (0.22 nm). Thus, these modes overlap considerably, which can lead to the large apparent background in the spectrum. The resonance Q-factors were measured to be ~ 4000 , which is consistent with Q-factors reported in other liquid lasing microcavities [237, 158]. Because of the close-packed array structure, these modes were often observed to couple into adjacent spheres up to 2 spheres distant (Figure 5.4b).

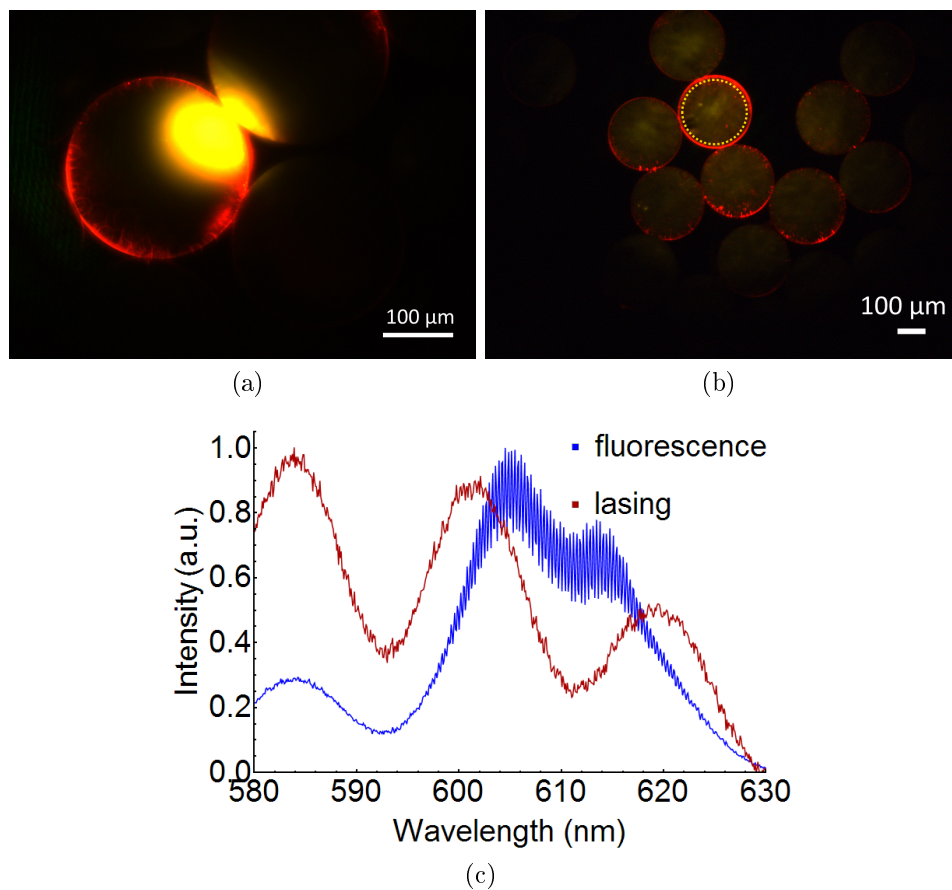


Figure 5.4: (a) Droplet lasing image. The yellow-green area is where the laser is incident on the spheres. (b) Image of multiple droplets. The position of the laser beam is indicated by the dashed yellow circle. Red equatorial bands can be seen even on microspheres that are not being directly pumped by the laser. (c) Droplet fluorescence and lasing spectra.

Liquid droplets of red polymer with mean diameter $161 \mu\text{m}$ and standard deviation $6 \mu\text{m}$ were allowed to slowly evaporate over a period of ~ 48 hours. (The nominal flow rates of the two solutions were 0.15 mL/min for the PVA solution and 0.05 mL/min for the MEH-PPV solution. However, a partial blockage was discovered afterwards which had been impeding the MEH-PPV

solution flow so these microspheres were slightly smaller than expected.) During this process, the chloroform gradually diffused through the water, shrinking the remaining droplet size and concentrating the polymer until it solidified. The PVA/water solution level remained roughly constant over this 48 hour period. This procedure resulted in a hexagonal array of highly monodisperse fluorescent MEH-PPV microspheres, where a solid microsphere remained near the centre of every original droplet (Figure 5.5). In Figure 5.5, we see that most of the solid microspheres are slightly below and to the right of the centre of the liquid droplet, implying that there was a small amount of drift over the 48 hour drying time. As all the spheres have moved in the same direction, this is possibly due to a very slight horizontal tilt of the beaker over the 48-hour drying period.

After drying, the mean microsphere diameter was 48 μm with a standard deviation of 2 μm , which is the narrowest size distribution observed so far for fluorescent CP microspheres larger than 5 μm in diameter. By comparing the volume of the original droplet with that of the solid polymer microsphere and using the known density of MEH-PPV (0.99 g/cm^3) and initial concentration (20 mg/mL), the spheres must be 28.6% hollow. In other words, the remaining solid MEH-PPV spheres are larger than if they were made of solid polymer, considering the known starting concentration.

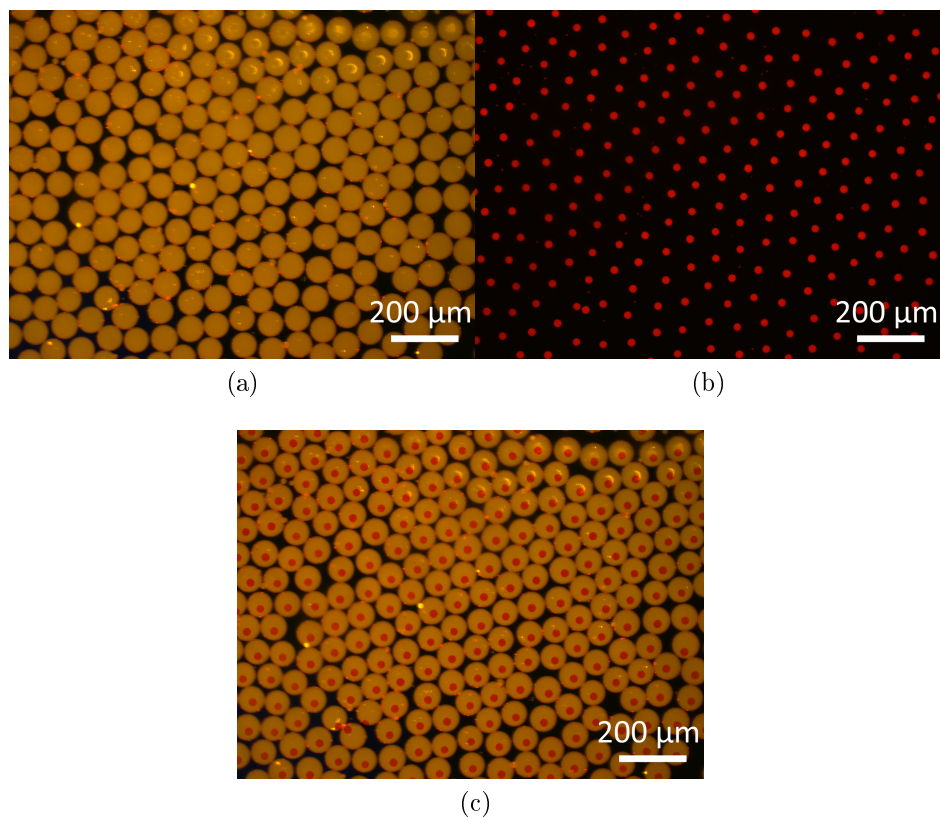


Figure 5.5: (a) Liquid droplets of the red polymer in a close-packed array. (b) Solid microspheres in a hexagonal pattern. (c) An overlay of images (a) and (b), showing that the solid microspheres form just below and to the right of the centre of the liquid droplets.

Control over the microsphere diameter could be achieved in two ways: 1) By changing the flow rate of the polymer, while keeping the other parameters the same and 2) By changing the polymer concentration in the dispersed phase. The first method resulted in a linear increase of droplet diameter with flow rate, as shown in Figure 5.6. By increasing the flow rate of the MEH-PPV solution from 0.01 mL/min to 0.05 mL/min, while keeping the PVA flow rate constant at 0.15 mL/min, the droplet diameter increased monotonically

from $D = 247 \pm 6 \mu\text{m}$ to $D = 313 \pm 9 \mu\text{m}$. All three samples had dispersities $\overline{D} \approx 0.001$. Dispersity is defined as $\overline{D} = (\sigma/\mu)^2$, where σ is the standard deviation of the particle diameter and μ is the mean diameter. Values of $\overline{D} < 0.1$ are considered to be monodisperse [238, 239].

The resulting solid microspheres also had a larger diameter as flow rate increased, although the dependence of diameter on flow rate was not linear as expected (see Figure 5.6), indicating that some microspheres were probably more hollow after drying than others. The mean diameters ranged from $D = 84 \pm 4 \mu\text{m}$ to $D = 118 \pm 5 \mu\text{m}$ and the solid microspheres had larger dispersities than those of the liquid microspheres, with $\overline{D} \approx 0.02$ for the solid microsphere samples. The increased dispersities and non-linear dependence of diameter on flow rate are both likely due to the fact that, in all three samples, the microspheres moved while drying. Some microspheres collected in bigger clusters while others were more dispersed, and the ‘lone’ microspheres solidified more quickly and appeared more rough in optical microscope images than the ‘clustered’ microspheres, which dried more slowly and were smoother. Movement during the drying process clearly results in different sizes and surface roughness in the final solid microspheres, even when they formed from the same monodisperse liquid droplets.

The second method is yet to be tested. It will result in liquid droplets of the same size but with different MEH-PPV concentrations; we expect that droplets with a lower concentration of MEH-PPV will yield smaller microspheres while maintaining a similar degree of monodispersity. However, there are limits to this. The maximum solubility of MEH-PPV in chloroform is $\sim 20 \text{ mg/mL}$, which will limit the upper microsphere size, and we know from earlier preliminary experiments that at low concentrations ($\sim 5 \text{ mg/mL}$), the droplets do not dry into microspheres but rather “collapse” into non-spherical particles.

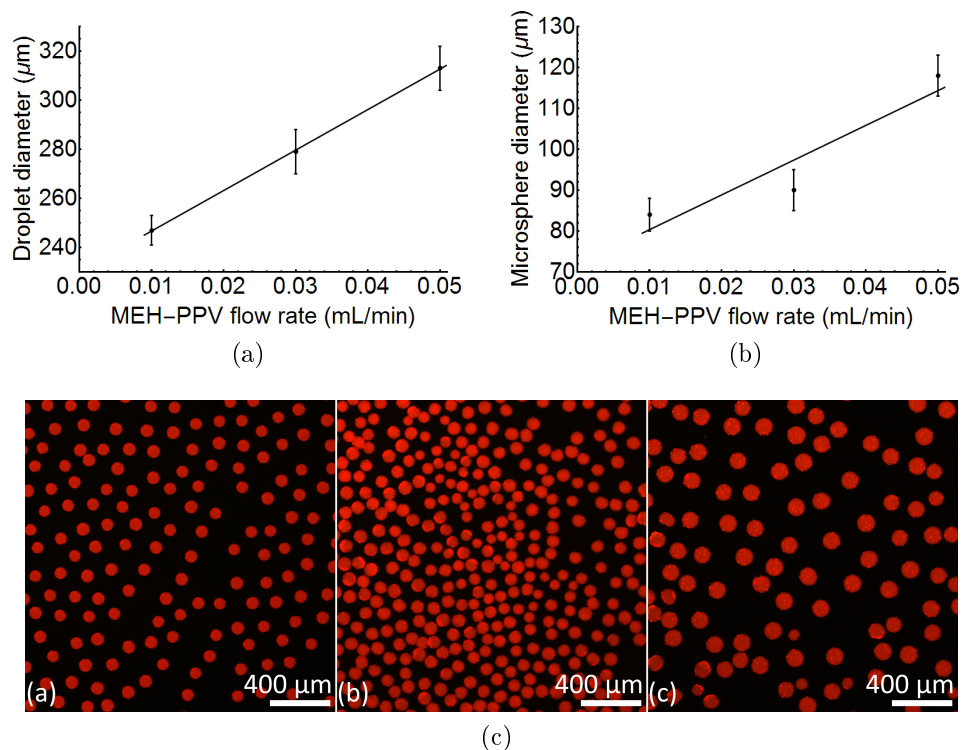


Figure 5.6: (a) Droplet diameter dependence on polymer flow rate. The diameter of the liquid droplets increases linearly with the MEH-PPV flow rate. (b) Solid microsphere diameter dependence on polymer flow rate. Although there are only three points, the diameter does not appear to increase linearly with flow rate. (c) Fluorescence images showing the 3 samples of differently sized PPV solid particles referred to in (b).

For the green and blue polymers, initial experiments showed that the microfluidics method also resulted in monodisperse microspheres. For both the green and blue microdroplets, the PVA flow rate was 0.15 mL/min. The flow rate of the green polymer was 0.05 mL/min and the flow rate of the blue polymer was 0.01 mL/min. This lower flow rate was used for the blue polymer because larger MEH-PPP microdroplets tended to dry into non-

spherical structures, but smaller microdroplets tended to form microspheres. The green microspheres had a mean diameter of $101\ \mu\text{m}$ with a standard deviation of $4\ \mu\text{m}$ and a dispersity $\overline{D} \approx 0.002$. The blue microspheres had a mean diameter of $67\ \mu\text{m}$ with a standard deviation of $3\ \mu\text{m}$ and a dispersity of $\overline{D} \approx 0.001$.

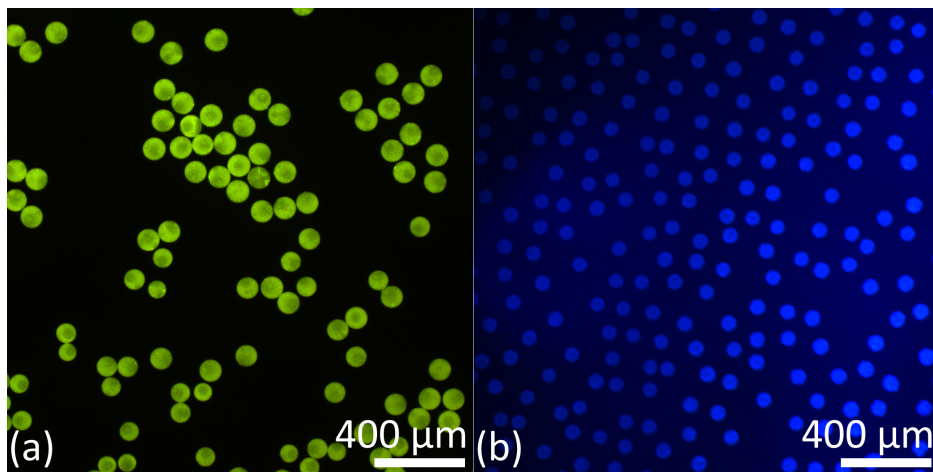


Figure 5.7: Fluorescence image showing green and blue monodisperse microspheres.

The formation of the particles depends strongly on the choice of the dispersed phase and the continuous phase, and their relative solubilities in one another [240]. If the polymer solvent has a relatively high solubility in the continuous phase then the kinetics of the droplet formation proceed more quickly and the resulting microstructure tends toward nonspherical aggregates. If the continuous phase is reasonably soluble in the polymer solvent, then one ends up with precipitation in a 3-phase non-equilibrium droplet, leading to rough, cratered, or nonspherical particles [240]. In this work, chloroform (the polymer solvent) is slightly soluble (0.8%) in water (the continuous phase), which favours spherical particle formation. Water is soluble

only at low concentrations (0.05%) in chloroform, which should also favour spherical particles with relatively few voids.

Nevertheless, significant structural features were observed in all the particles. The qualitative “order of sphericity” (where we define higher sphericity to mean smoother surfaces and fewer obviously non-spherical particles present in a sample) was MEH-PPV > EH-P(PVPVP) > MEH-PPP. This order might depend on both molecular weight and polymer structure. The slightly higher molecular weight of the MEH-PPV used compared to that of the MEH-PPP meant that, at the concentrations used (20 mg/mL), the MEH-PPV solution was more viscous than the MEH-PPP solution and was possibly then more resistant to deformation and the formation of surface structures while drying. The EH-P(PVPVP) had the lowest molecular weight and was the least viscous of all three solutions, but it is possible that its bulkier structure helped to maintain a spherical shape while drying, so these particles had a higher sphericity than the MEH-PPV particles.

5.3 List of Experiments to be completed

As this work was cut short by the requirement to cease all non-essential research, a few experiments remain to complete this work for publication. They are listed below with estimates of the time required to complete. Allowing for various problems and potential mishaps, less than one month of work would be required, including completing the final manuscript revisions.

- Helium ion microscope imaging of samples of monodisperse red, green and blue microspheres.
- Fabrication and optical microscope imaging of red, green and blue microspheres fabricated by the emulsification method.
- Repeat fabrication and optical microscope imaging of red, green and blue microspheres formed by the microfluidics method, with careful

control over the drying conditions - in particular the density of microspheres in the beaker (which seemed to impact the rate of chloroform diffusion) and also with care taken to keep the beaker level during drying.

- Fabrication and optical microscope imaging of alternating-coloured arrays. These arrays will be made by using a double T-junction set up, which has already been assembled.

5.4 Experimental Section

Materials synthesis:

All polymers were prepared by Dr. Sergey Vagin at the Technical University of Munich. MEH-PPV of the desired molecular weight was prepared as described in our previous publication [233]. Comparison of UV-Vis spectra of prepared samples with previous batches confirmed their identity. MEH-PPV with an absorption maximum at ca. 490 nm in a chloroform solution was utilised for fabrication of spheres. The molecular weights were measured with gel permeation chromatography (GPC) in THF relative to polystyrene and they ranged within $M_N \approx 30\text{-}50$ kg/mol and $M_W \approx 140\text{-}220$ kg/mol.

MEH-PPP was prepared in accordance with the common Grignard metathesis (GRIM) polymerisation route starting from a monomer precursor 1,4-dibromo-2-(2-ethylhexyloxy)-5-methoxybenzene (see Scheme 1), which was available through a literature procedure [241]. The degassed monomer precursor **1** (2.2 g, 5.4 mmol) was dissolved in 5 mL of dry degassed THF and 5.4 mL of 1M Turbo-Grignard reagent $i\text{PrMgClLiCl}$ in THF was added. The light brown solution was left for 20 h with stirring at room temperature. 2.3 mg (0.05%) of a catalyst $[\text{NiBr}_2(\text{PPh}_3)(\text{iPr})]$ (**2**) (prepared according to the literature procedure [242]) in 0.2 mL THF was added; the solution colour changed to a more intense brown-yellowish. After several hours, a clear solution became turbid and obviously more viscous. After five days the reaction

mixture turned to a turbid highly viscous mass, which was then transferred into acidified methanol (ca. 100 mL with 10 droplets of concentrated HCl) and stirred vigorously for few minutes. The precipitate was allowed to settle down followed by decantation and addition of a fresh portion of methanol. The suspension was stirred for a few hours, decanted and treated with a fresh portion of methanol. The mixture was stirred overnight, decanted and washed with several 50 mL portions of acetone in a similar way to remove any low molecular weight byproducts. After drying, the yield was approximately 0.9 g (67%) with slight batch-to-batch variations. The molecular weights of the obtained MEH-PPP measured with GPC in THF relative to polystyrene were typically in the range $M_N \approx 26\text{-}30$ kg/mol, $M_W \approx 56\text{-}150$ kg/mol for various batches of monomer precursor 1, Turbo-Grignard reagent, as well as reaction solvent.

EH-P(PVPVP) was prepared following the GRIM polymerization procedure (Scheme 3). First, the monomer precursor (compound 5) was prepared by the Horner-Wadsworth-Emmons reaction of tetraethyl ((2,5-bis((2-ethylhexyl)oxy)-1,4-phenylene)bis(methylene))bis(phosphonate) (3) with commercially available 4-bromo-2,5-dimethoxy-benzaldehyde (4) (see Scheme 2). Compound 3 was prepared according to the literature procedure [243]. For the synthesis of 5, 3 g of 3 was mixed with 10 mL of anhydrous tert-butanol followed by the addition of 1.6 g (3 equivalent) of potassium tert-butoxide in 30 mL of anhydrous tert-butanol. Compound 4 (2.5 g, 2.14 equivalent) was dissolved in 25 mL of dry THF and added to the reaction solution. The reaction mixture was heated at 60°C overnight. After cooling, the reaction volume was reduced to 1/3 by partial removal of the solvent under vacuum, leading to a formation of a fine crystalline precipitate. This was filtered off, washed with methanol and dried in vacuo to yield 2.2 g (57%) of a bright yellow solid. The filtrate was diluted with 300 mL of water and left overnight, then decanted and the viscous orange residue was left to dry in air. It was taken up into 30 mL diethyl ether,

then 1 grain of iodine was added and diluted with 40 mL ethanol. The solution was heated overnight at 80°C allowing the diethyl ether to slowly evaporate. Then vacuum was applied to concentrate the solution until the formation of a precipitate. After cooling, it was filtered off and washed with methanol to give 0.63 g of a yellow-orangeish product. The filtrate was further concentrated to remove the methanol and heated overnight at 80°C. Leaving the solution for two weeks resulted in the formation of a yellow precipitate (0.32 g), giving 81% overall yield of the reaction.

For the synthesis of EH-P(PVPVP), the monomer precursor (compound 5) (407 mg, 0.5 mmol) was dissolved in 1.5 mL of dry THF and 0.5 mL (1 equivalent) of 1M-Turbo-Grignard reagent $i\text{PrMgClLiCl}$ in THF was added. The solution was protected from light and stirred overnight at room temperature and the colour of the solution became orange. Then, 0.6 mg (0.14%) of $[\text{NiBr}_2(\text{PPh}_3)(\text{iPr})]$ (2) in 0.2 mL THF was added. An immediate change of colour to dark orange was observed. After stirring for 24 hours at room temperature, the colour of the solution became light orange and some increase in viscosity could be observed. The reaction mixture was quenched by 15 mL methanol with a few droplets of concentrated HCl and decanted. A fresh portion of methanol was added to the solid residue and stirred for 3 days. During this procedure, the initially formed solid block became homogenised. The suspension was filtered, the solid was extracted with 20 mL ethanol, filtered off and dried, giving 220 mg of yellow powder. According to GPC analysis, this crude material contained noticeable amount of monomeric and dimeric species. They were extracted with several 20 mL portions of pentane over 24 hours, leaving 120 mg of EH-P(PVPVP) after drying. The molecular weights of the resulting polymer measured with GPC in THF relative to polystyrene were typically $M_N \approx 7 \text{ kg/mol}$, $M_W \approx 15 \text{ kg/mol}$.

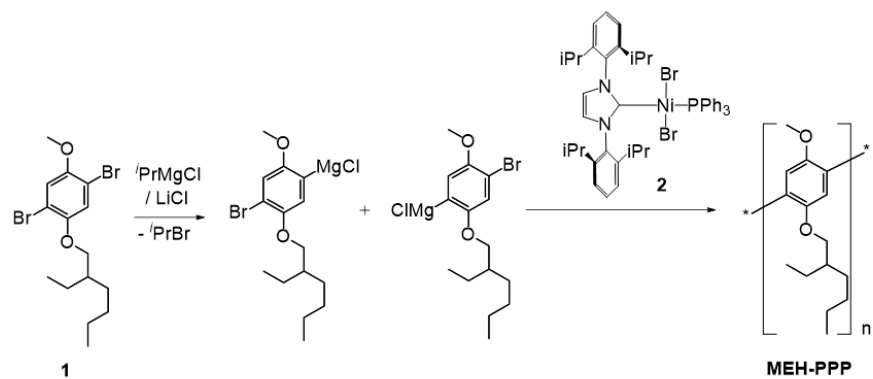


Figure 5.8: Scheme 1: Synthesis of MEH-PPP.

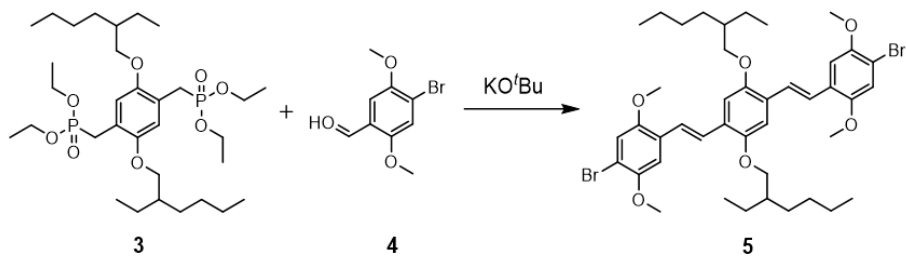


Figure 5.9: Scheme 2: Synthesis of the monomer precursor of EH-P(PVPVP).

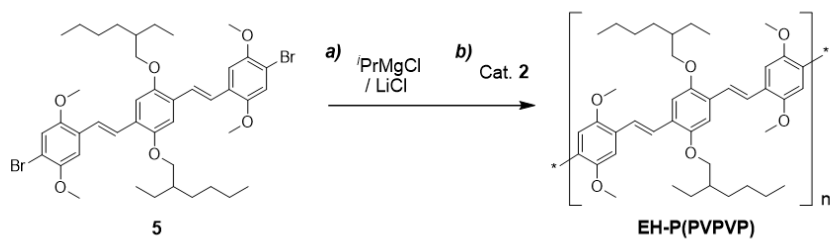


Figure 5.10: Scheme 3: Synthesis of EH-P(PVPVP).

Microfluidics

The polymers were dissolved into chloroform at a concentration of 20 mg/mL (solution 1). Investigations with various concentrations showed that reasonably large microspheres can be formed at this concentration. Separately, a solution of deionised water was prepared with 5 wt.% polyvinyl alcohol (PVA) as a surfactant and 5 vol.% 1-propanol as a secondary surfactant (solution 2). The solutions were injected into each arm of a microfluidic T-junction at a flow rate of 0.01 to 0.05 mL/min (solution 1) and 0.15 mL/min (solution 2). This produced droplets of the dissolved polymer carried in the water/surfactant “continuous phase”. The droplets were injected into a flat-bottomed beaker of the same water-PVA solution, where they quickly fell to the bottom due to the higher density of chloroform and spontaneously self-assembled into a hexagonal close-packed array. The array of droplets was then left standing for 48 hours to allow the chloroform to evaporate, concentrating and drying the residual polymer. This resulted in a (non-close-packed) hexagonal array of fluorescent CP microspheres of a uniform size.

Fluorescence microscopy and spectroscopy

Fluorescence microscopy was performed on a Nikon TE2000e inverted epifluorescence microscope. A 365 nm LED was used as the excitation source for the blue polymer, and a 405 nm LED was used for the green and red polymers. Fluorescence images were captured with either a Retiga EX fluorescence camera or a Sony a6400 consumer camera interfaced to the microscope. A 409-nm dichroic filter (Iridian) and 400-nm longpass filter (Thorlabs) were used to block the 365 nm LED light and pass the fluorescence of the blue polymer. A 550-nm dichroic filter (Iridian) and 550-nm longpass filter (Thorlabs) were used to block the 405 nm LED light and pass the fluorescence of the green and red polymers. Fluorescence spectroscopy was performed using an

intensity-calibrated Ocean Optics 2000+ miniature spectrometer interfaced to a fibre-optic collection system.

Acknowledgements

The authors thank DFG (German Research Foundation, project number 245845833, IRTG 2022) and NSERC (CREATE grant 463990-2015) for financial support of the Alberta/Technische Universität München Graduate School for Functional Hybrid Materials (ATUMS) and Future Energy Systems.

6 Conclusion

Main results and contributions

My first project focused on characterising the lasing properties of dye-doped microspheres, with the aim of understanding the lasing behaviour and improving the lasing characteristics, including stability and mode selection. To this end, I made silica microspheres with a dye-doped polymer bilayer coating. We then performed fluorescence and lasing measurements in our lab, partnered with Dr. Y. Zhi from Peking University to do cold-cavity measurements, and also performed simulations in order to compare the experimental results with theory. Previously, there had been few studies that examined the mode structure of lasing microspheres using a combination of all of these techniques. Our research showed that the complex lasing structure which is sometimes observed in fluorescent microspheres is due to a dense forest of bare-cavity modes, which themselves arise from symmetry-breaking in spheres with small ellipticity and various inhomogeneities in the polymer coating. These two effects will likely be present in almost all methods of microsphere fabrication and are of relevance to future understanding of lasing spectra from polymer microspheres.

The second project was to create fluorescent polymer microspheres from a conjugated polymer and investigate the fluorescence and lasing behaviour of such microspheres, as well as to achieve control over their surface structure and internal structure. We discovered that the key to making large, smooth CP microspheres is to use a low molecular weight CP which can be more easily dissolved at high concentrations in a hydrophobic, organic solvent. We were successful in creating MEH-PPV microspheres up to 100 μm in diameter (10 to 50 times larger than CP microspheres fabricated previously by other methods) which were 20 times brighter than commercially available dye-doped microspheres and exhibited lasing, which was not seen in the commercially prepared microspheres that we used for comparison. The work

demonstrated the outstanding fluorescent properties of CP microspheres and a route toward the development of a new class of ultra-bright microspheres for diagnostics and imaging.

Many applications of fluorescent microspheres require them to be uniform and have narrow size distributions. The previous work successfully produced bright CP microspheres but the size distribution was wide. The final project of this thesis was to fabricate monodisperse CP microspheres and demonstrate size-control over individual batches. To accomplish this, I built a microfluidics system which allowed control over the size of the microspheres by changing the flow rates of the polymer and aqueous solutions, resulting in microspheres with very low dispersities of $\mathcal{D} \leq 0.02$. The liquid microdroplets initially formed close-packed lattices and individual microdroplets exhibited evidence of lasing. I fabricated arrays of solid microspheres from three different CPs, resulting in red-, green- and blue-emitting monodisperse microspheres. The results imply that this method is likely applicable to a wide variety of CPs and could be used in the future to fabricate monodisperse microspheres from a range of different-coloured fluorescent polymers.

Outstanding problems and possible solutions

During the course of this work, one of the biggest problems we encountered was the photobleaching of the fluorophores due to photooxidation. In both the dye-doped polymer microspheres and the conjugated polymer microspheres, photobleaching was obvious in a matter of minutes and stopped the lasing of the microspheres, often causing obvious colour changes to the microspheres which we interpreted as oxidative damage to the polymer. We have to some degree circumvented this problem by encasing the microspheres in protective layers; silica microspheres attached to a stem were dip-coated in a protective polymer coating, and free standing CP microspheres were embedded in a resin layer. However, for the CP microspheres, embedding them in a layer is an imperfect solution as, by definition, they are then no

longer free standing and cannot be removed for use. It would be better if, during the fabrication process, an extra step could be added to coat each sphere individually in a protective layer. This might be achieved with a more complex microfluidic system in which, after the initial (hydrophobic) liquid polymer droplet forms, it is then passed through another junction which adds a (hydrophilic, immiscible) liquid layer of an oxygen-impermeable polymer around it. The final, solid microsphere would then be a core-shell structure, protected from photooxidation but still free-standing.

Another problem I encountered is that the size and structure of the microspheres produced by the microfluidics method are very sensitive to even small changes in the drying conditions, with the result that there can be variability even within the same batch of microspheres. In particular, if the microspheres move while drying so that some collect in bigger clusters while others are more dispersed, the ‘lone’ microspheres solidify more quickly than the ‘clustered’ microspheres, resulting in different sizes and sphericity even though they all formed from the same monodisperse liquid droplets. So far, the spheres have been left to dry in a relatively ‘uncontrolled’ environment: on a shelf in a low-traffic area. More consistent results could potentially be achieved if I used a specific ‘drying-stage’ on which the samples could dry horizontally and without room vibrations. The spheres would then not move, and would dry more consistently.

Suggestions for future research.

The initial motivation for producing lasing microspheres was for their superior brightness, making them promising candidates for sensing applications. To this end, future work could explore the sensing capabilities of lasing microspheres in air and in water, and demonstrate their suitability for biosensing. Another interesting direction would be to use the microfluidics system to produce microspheres of mixed conjugated polymers. Various morphologies should be possible, *e.g.* homogeneously mixed, core-shell, or Janus-type con-

jugated polymer microspheres. One other option is to investigate the lasing behaviour of liquid and solid microsphere arrays, where the optical resonances should couple between different microspheres that are in contact with one another, possibly leading to interactive lasing behaviour including mode selection and filtering.

In general, this was the first work that produced large fluorescent and lasing microspheres, and then solved the polydispersity problem. Thus, there are many future directions one could take to refine the structural properties, establish emission colour control, and evaluate the potential applications of fluorescent microspheres with strongly enhanced emission intensity.

References

- [1] J. W. S. Rayleigh, “The problem of the whispering gallery,” *Philosophical Magazine* **20**, pp. 1001–1004, Dec. 1910.
- [2] K. Volyanskiy, P. Salzenstein, H. Tavernier, M. Pogurmirskiy, Y. K. Chembo, and L. Larger, “Compact optoelectronic microwave oscillators using ultra-high Q whispering gallery mode disk-resonators and phase modulation,” *Optics Express* **18**, pp. 22358–22363, Oct. 2010.
- [3] A. Schweinsberg, S. Hocdé, N. N. Lepeshkin, R. W. Boyd, C. Chase, and J. E. Fajardo, “An environmental sensor based on an integrated optical whispering gallery mode disk resonator,” *Sensors and Actuators B: Chemical* **123**, pp. 727–732, May 2007.
- [4] G. Lin, B. Qian, F. Orucevic, Y. Candela, J.-B. Jager, Z. Cai, V. Lefèvre-Seguin, and J. Hare, “Excitation mapping of whispering gallery modes in silica microcavities,” *Optics Letters* **35**, pp. 583–585, Feb. 2010.
- [5] L. He, Y.-F. Xiao, C. Dong, J. Zhu, V. Gaddam, and L. Yang, “Compensation of thermal refraction effect in high-Q toroidal microresonator by polydimethylsiloxane coating,” *Applied Physics Letters* **93**, p. 201102, Nov. 2008.
- [6] P. Bianucci, J. R. Rodríguez, C. Clements, C. M. Hessel, J. G. C. Veinot, and A. Meldrum, “Whispering gallery modes in silicon nanocrystal coated microcavities,” *physica status solidi (a)* **206**, pp. 973–975, May 2009.
- [7] K. J. Rowland, A. François, P. Hoffmann, and T. M. Monro, “Fluorescent polymer coated capillaries as optofluidic refractometric sensors,” *Optics Express* **21**, pp. 11492–11505, May 2013.

- [8] I. M. White, H. Oveys, and X. Fan, “Liquid-core optical ring-resonator sensors,” *Optics Letters* **31**, pp. 1319–1321, May 2006.
- [9] M. V. Maximov, N. V. Kryzhanovskaya, A. M. Nadtochiy, E. I. Moiseev, I. I. Shostak, A. A. Bogdanov, Z. F. Sadrieva, A. E. Zhukov, A. A. Lipovskii, D. V. Karpov, J. Laukkanen, and J. Tommila, “Ultrasmall microdisk and microring lasers based on InAs/InGaAs/GaAs quantum dots,” *Nanoscale Research Letters* **9**, p. 657, Dec. 2014.
- [10] M. L. Gorodetsky, A. A. Savchenkov, and V. S. Ilchenko, “Ultimate Q of optical microsphere resonators,” *Optics Letters* **21**, pp. 453–455, Apr. 1996.
- [11] N. M. Hanumegowda, C. J. Stica, B. C. Patel, I. White, and X. Fan, “Refractometric sensors based on microsphere resonators,” *Applied Physics Letters* **87**, p. 201107, Nov. 2005.
- [12] F. Vollmer and S. Arnold, “Whispering-gallery-mode biosensing: label-free detection down to single molecules,” *Nature Methods* **5**, pp. 591–596, July 2008.
- [13] J.-P. Laine, *Design and applications of optical microsphere resonators*. PhD thesis, Helsinki University of Technology, Espoo, 2003. OCLC: 58339452.
- [14] L. He, S. K. Özdemir, and L. Yang, “Whispering gallery microcavity lasers,” *Laser & Photonics Reviews* **7**, pp. 60–82, Jan. 2013.
- [15] M. Kuwata-Gonokami, “Laser emission from dye-doped polystyrene microsphere,” in *Proceedings of LEOS '93*, pp. 300–301, Nov. 1993.
- [16] G. Righini, Y. Dumeige, P. Feron, M. Ferrari, G. Nunzi Conti, D. Ristic, and S. Soria, “Whispering gallery mode microresonators: Fundamentals and applications,” *La Rivista del Nuovo Cimento* **34**, pp. 435–488, June 2011.

- [17] J. Ward and O. Benson, “WGM microresonators: sensing, lasing and fundamental optics with microspheres,” *Laser & Photonics Reviews* **5**, pp. 553–570, July 2011.
- [18] Y. Panitchob, G. S. Murugan, M. N. Zervas, P. Horak, S. Berneschi, S. Pelli, G. N. Conti, and J. S. Wilkinson, “Whispering gallery mode spectra of channel waveguide coupled microspheres,” *Optics Express* **16**, pp. 11066–11076, July 2008.
- [19] V. Lefèvre-Seguin, “Whispering-gallery mode lasers with doped silica microspheres,” *Optical Materials* **11**, pp. 153–165, Jan. 1999.
- [20] H. P. Weber and R. Ulrich, “A Thin-Film Ring Laser,” *Applied Physics Letters* **19**, pp. 38–40, July 1971.
- [21] M. Gomilsek, “Whispering gallery modes.” University of Ljubljana, Ljubljana, Slovenia, 2011.
- [22] T. J. A. Kippenberg, *Nonlinear Optics in Ultra-high-Q Whispering-Gallery Optical Microcavities*. PhD thesis, California Institute of Technology, 2004.
- [23] J. R. Buck and H. J. Kimble, “Optimal sizes of dielectric microspheres for cavity QED with strong coupling,” *Physical Review A* **67**, p. 033806, Mar. 2003.
- [24] P. T. Kristensen, C. V. Vlack, and S. Hughes, “Generalized effective mode volume for leaky optical cavities,” *Optics Letters* **37**, pp. 1649–1651, May 2012.
- [25] A. F. Koenderink, “On the use of Purcell factors for plasmon antennas,” *Optics Letters* **35**, pp. 4208–4210, Dec. 2010.

- [26] K. Srinivasan, P. E. Barclay, M. Borselli, and O. Painter, “Optical-fiber-based measurement of an ultrasmall volume high-Q photonic crystal microcavity,” *Physical Review B* **70**, p. 081306, Aug. 2004.
- [27] V. Sandoghdar, F. Treussart, J. Hare, V. Lefèvre-Seguin, J. M. Raimond, and S. Haroche, “Very low threshold whispering-gallery-mode microsphere laser,” *Physical Review A* **54**, pp. R1777–R1780, Sept. 1996.
- [28] J. D. Jackson, *Classical Electrodynamics*, John Wiley & Sons, 2007.
- [29] F. Vollmer and L. Yang, “Review: Label-free detection with high-Q microcavities: a review of biosensing mechanisms for integrated devices,” *Nanophotonics* **1**, pp. 267–291, Jan. 2012.
- [30] P. Bianucci, X. Wang, J. G. C. Veinot, and A. Meldrum, “Silicon nanocrystals on bottle resonators: Mode structure, loss mechanisms and emission dynamics,” *Optics Express* **18**, pp. 8466–8481, Apr. 2010.
- [31] C.-A. Bunge, M. Beckers, and B. Lustermann, “Basic principles of optical fibres,” in *Polymer Optical Fibres*, pp. 47–118, Elsevier, 2017.
- [32] I. Agha, J. Sharping, M. Foster, and A. Gaeta, “Optimal sizes of silica microspheres for linear and nonlinear optical interactions,” *Applied Physics B* **83**, pp. 303–309, May 2006.
- [33] R. D. Kekatpure and M. L. Brongersma, “Fundamental photophysics and optical loss processes in Si-nanocrystal-doped microdisk resonators,” *Physical Review A* **78**, p. 023829, Aug. 2008.
- [34] A. B. Matsko and V. S. Ilchenko, “Optical resonators with whispering-gallery modes-part I: basics,” *IEEE Journal of Selected Topics in Quantum Electronics* **12**, pp. 3–14, Jan. 2006.

- [35] “RefractiveIndex.INFO - Refractive index database.” <https://refractiveindex.info>.
- [36] B. Crist, M. E. Marhic, G. Raviv, and M. Epstein, “Optical absorption in polymer glasses by laser calorimetry,” *Journal of Applied Physics* **51**, pp. 1160–1162, Feb. 1980.
- [37] M. Kuwata-Gonokami, R. H. Jordan, A. Dodabalapur, H. E. Katz, M. L. Schilling, R. E. Slusher, and S. Ozawa, “Polymer microdisk and microring lasers,” *Optics Letters* **20**, pp. 2093–2095, Oct. 1995.
- [38] M. Kuwata-Gonokami and K. Takeda, “Polymer whispering gallery mode lasers,” *Optical Materials* **9**, pp. 12–17, Jan. 1998.
- [39] S. V. Frolov, Z. V. Vardeny, and K. Yoshino, “Cooperative and stimulated emission in poly(p-phenylene-vinylene) thin films and solutions,” *Physical Review B* **57**, pp. 9141–9147, Apr. 1998.
- [40] S. V. Frolov, M. Shkunov, Z. V. Vardeny, and K. Yoshino, “Ring microlasers from conducting polymers,” *Physical Review B* **56**, pp. R4363–R4366, Aug. 1997.
- [41] Y. C. Cheng, “Effect of charge inhomogeneities on silicon surface mobility,” *Journal of Applied Physics* **44**, pp. 2425–2427, May 1973.
- [42] D. W. Vernooy, V. S. Ilchenko, H. Mabuchi, E. W. Streed, and H. J. Kimble, “High-Q measurements of fused-silica microspheres in the near infrared,” *Optics Letters* **23**, pp. 247–249, Feb. 1998.
- [43] M. Djiango, T. Kobayashi, E. Bouron, W. J. Blau, Y. Suzuki, and T. Kaino, “Operating characteristics of near-infrared self-assembled polymer microlasers,” *Optics Letters* **32**, pp. 1375–1377, June 2007.

- [44] C. Tapalian, J.-P. Laine, and P. A. Lane, “Thermo-optical switches using coated microsphere resonators,” *MRS Online Proceedings Library Archive* **694**, 2001. Publisher: Cambridge University Press.
- [45] S. Soria, F. Baldini, S. Berneschi, F. Cosi, A. Giannetti, G. N. Conti, S. Pelli, G. C. Righini, and B. Tiribilli, “High-Q polymer-coated microspheres for immunosensing applications,” *Optics Express* **17**, pp. 14694–14699, Aug. 2009. Publisher: Optical Society of America.
- [46] C. Sinturel, M. Vayer, M. Morris, and M. A. Hillmyer, “Solvent Vapor Annealing of Block Polymer Thin Films,” *Macromolecules* **46**, pp. 5399–5415, July 2013.
- [47] J. Vogelsang, J. Brazard, T. Adachi, J. C. Bolinger, and P. F. Barbara, “Watching the Annealing Process One Polymer Chain at a Time,” *Angewandte Chemie International Edition* **50**, pp. 2257–2261, Mar. 2011.
- [48] C.-Y. Chao and L. J. Guo, “Thermal-flow technique for reducing surface roughness and controlling gap size in polymer microring resonators,” *Applied Physics Letters* **84**, pp. 2479–2481, Apr. 2004. Publisher: American Institute of Physics.
- [49] C.-Y. Chao, W. Fung, and L. Guo, “Polymer microring resonators for biochemical sensing applications,” *IEEE Journal of Selected Topics in Quantum Electronics* **12**, pp. 134–142, Jan. 2006. Conference Name: IEEE Journal of Selected Topics in Quantum Electronics.
- [50] A. B. Matsko, A. A. Savchenkov, D. Strekalov, V. S. Ilchenko, and L. Maleki, “Review of Applications of Whispering-Gallery Mode Resonators in Photonics and Nonlinear Optics,” p. 51, Aug. 2005.
- [51] D. Sarid, P. J. Cressman, and R. L. Holman, “High-efficiency prism coupler for optical waveguides,” *Applied Physics Letters* **33**, pp. 514–515, Sept. 1978.

- [52] D. Sarid, “High efficiency input-output prism waveguide coupler: an analysis,” *Applied Optics* **18**, pp. 2921–2926, Sept. 1979.
- [53] R. Ulrich, “Theory of the Prism-Film Coupler by Plane-Wave Analysis,” *JOSA* **60**, pp. 1337–1350, Oct. 1970.
- [54] M. L. Gorodetsky and V. S. Ilchenko, “Optical microsphere resonators: optimal coupling to high-Q whispering-gallery modes,” *Journal of the Optical Society of America B* **16**, p. 147, Jan. 1999.
- [55] M. Cai, O. Painter, and K. J. Vahala, “Observation of Critical Coupling in a Fiber Taper to a Silica-Microsphere Whispering-Gallery Mode System,” *Physical Review Letters* **85**, pp. 74–77, July 2000.
- [56] M. Cai and K. Vahala, “Highly efficient optical power transfer to whispering-gallery modes by use of a symmetrical dual-coupling configuration,” *Optics Letters* **25**, pp. 260–262, Feb. 2000.
- [57] N. Dubreuil, J. C. Knight, D. K. Leventhal, V. Sandoghdar, J. Hare, and V. Lefèvre, “Eroded monomode optical fiber for whispering-gallery mode excitation in fused-silica microspheres,” *Optics Letters* **20**, pp. 813–815, Apr. 1995. Publisher: Optical Society of America.
- [58] M. Charlebois, A. Paquet, L. Verret, K. Boissinot, M. Boissinot, M. Bergeron, and C. N. Allen, “Toward Automatic Label-Free Whispering Gallery Modes Biodetection with a Quantum Dot-Coated Microsphere Population,” *Nanoscale Research Letters* **5**, p. 524, Feb. 2010.
- [59] J. W. Silverstone, S. McFarlane, C. P. K. Manchee, and A. Meldrum, “Ultimate resolution for refractometric sensing with whispering gallery mode microcavities,” *Optics Express* **20**, pp. 8284–8295, Apr. 2012.
- [60] H. T. Beier, G. L. Côté, and K. E. Meissner, “Whispering Gallery Mode Biosensors Consisting of Quantum Dot-Embedded Microspheres,” *Annals of Biomedical Engineering* **37**, pp. 1974–1983, Oct. 2009.

- [61] A. Francois and M. Himmelhaus, “Optical biosensor based on whispering gallery mode excitations in clusters of microparticles,” *Applied Physics Letters* **92**, p. 141107, Apr. 2008.
- [62] T. Ioppolo, M. Kozhevnikov, V. Stepaniuk, M. V. Ötügen, and V. Sheverev, “Micro-optical force sensor concept based on whispering gallery mode resonators,” *Applied Optics* **47**, pp. 3009–3014, June 2008.
- [63] S. Corbellini, C. Ramella, L. Yu, M. Pirola, and V. Fernicola, “Whispering Gallery Mode Thermometry,” *Sensors* **16**, p. 1814, Nov. 2016.
- [64] A. K. Mallik, D. Liu, V. Kavungal, Q. Wu, G. Farrell, and Y. Semenova, “Agarose coated spherical micro resonator for humidity measurements,” *Optics Express* **24**, pp. 21216–21227, Sept. 2016.
- [65] W. Wang, M.-J. Zhang, and L.-Y. Chu, “Functional Polymeric Microparticles Engineered from Controllable Microfluidic Emulsions,” *Accounts of Chemical Research* **47**, pp. 373–384, Feb. 2014.
- [66] Y. Li, H. L. Jiang, J. F. Jin, and K. J. Zhu, “Bioadhesive Fluorescent Microspheres as Visible Carriers for Local Delivery of Drugs. II: Uptake of Insulin-Loaded PCEFB/PLGA Microspheres by the Gastrointestinal Tract,” *Drug Delivery* **11**, pp. 335–340, Jan. 2004.
- [67] M. Schubert, A. Steude, P. Liehm, N. M. Kronenberg, M. Karl, E. C. Campbell, S. J. Powis, and M. C. Gather, “Lasing within Live Cells Containing Intracellular Optical Microresonators for Barcode-Type Cell Tagging and Tracking,” *Nano Letters* **15**, pp. 5647–5652, Aug. 2015.
- [68] S. E. A. Gratton, P. A. Ropp, P. D. Pohlhaus, J. C. Luft, V. J. Madden, M. E. Napier, and J. M. DeSimone, “The effect of particle design on cel-

- lular internalization pathways,” *Proceedings of the National Academy of Sciences* **105**, pp. 11613–11618, Aug. 2008.
- [69] L. Wang and R. A. Hoffman, “Standardization, Calibration, and Control in Flow Cytometry,” *Current Protocols in Cytometry* **79**(1), pp. 1.3.1–1.3.27, 2017.
- [70] R. J. Langenhorst, S. Lawson, A. Kittawornrat, J. J. Zimmerman, Z. Sun, Y. Li, J. Christopher-Hennings, E. A. Nelson, and Y. Fang, “Development of a Fluorescent Microsphere Immunoassay for Detection of Antibodies against Porcine Reproductive and Respiratory Syndrome Virus Using Oral Fluid Samples as an Alternative to Serum-Based Assays,” *Clinical and Vaccine Immunology* **19**, pp. 180–189, Feb. 2012.
- [71] A. Friese, J. Kallmeyer, J. A. Kitte, I. M. Martínez, S. Bijaksana, and D. Wagner, “A simple and inexpensive technique for assessing contamination during drilling operations,” *Limnology and Oceanography: Methods* **15**(2), pp. 200–211, 2017.
- [72] J. B. Edel, E. K. Hill, and A. J. d. Mello, “Velocity measurement of particulate flow in microfluidic channels using single point confocal fluorescence detection,” *Analyst* **126**, pp. 1953–1957, Nov. 2001. Publisher: The Royal Society of Chemistry.
- [73] I. D. W. Samuel and G. A. Turnbull, “Polymer lasers: recent advances,” *Materials Today* **7**, pp. 28–35, Sept. 2004.
- [74] H. Naarmann, “Polymers, Electrically Conducting,” in *Ullmann’s Encyclopedia of Industrial Chemistry*, pp. 295–314, Wiley-VCH Verlag GmbH & Co. KGaA, 2012.
- [75] J. Mei and Z. Bao, “Side Chain Engineering in Solution-Processable Conjugated Polymers,” *Chemistry of Materials* **26**, pp. 604–615, Jan. 2014.

- [76] D. Jeremic, "Polyethylene," in *Ullmann's Encyclopedia of Industrial Chemistry*, pp. 1–42, Wiley-VCH Verlag GmbH & Co. KGaA, Aug. 2014.
- [77] A. Sionkowska, "Current research on the blends of natural and synthetic polymers as new biomaterials: Review," *Progress in Polymer Science* **36**, pp. 1254–1276, Sept. 2011.
- [78] "Polymer Molecular Weight - An Overview." <https://www.sciencedirect.com/topics/engineering/polymer-molecular-weight>.
- [79] A. Rudin and P. Choi, *The Elements of Polymer Science and Engineering*, Elsevier, 2013.
- [80] R. W. Nunes, J. R. Martin, and J. F. Johnson, "Influence of molecular weight and molecular weight distribution on mechanical properties of polymers," *Polymer Engineering & Science* **22**(4), pp. 205–228, 1982.
- [81] D. van Krevelen, *Properties of Polymers*, Elsevier, 1997.
- [82] A. Shrivastava, "Polymerization," in *Introduction to Plastics Engineering*, pp. 17–48, Elsevier, 2018.
- [83] J. Brandrup, E. H. Immergut, E. A. Grulke, A. Abe, and D. R. Bloch, *Polymer Handbook*, vol. 89, Wiley New York, 1999.
- [84] J. E. Mark, ed., *Physical Properties of Polymers Handbook*, Springer, New York, 2nd ed., 2006.
- [85] "Young's Modulus - Tensile and Yield Strength for common Materials." https://www.engineeringtoolbox.com/young-modulus-d_417.html.
- [86] C. Liao, M. Zhang, M. Y. Yao, T. Hua, L. Li, and F. Yan, "Flexible Organic Electronics in Biology: Materials and Devices," *Advanced Materials* **27**, pp. 7493–7527, Dec. 2015.

- [87] M. C. McAlpine, H. Ahmad, D. Wang, and J. R. Heath, “Highly ordered nanowire arrays on plastic substrates for ultrasensitive flexible chemical sensors,” *Nature Materials* **6**, pp. 379–384, May 2007.
- [88] T. Yokota, P. Zalar, M. Kaltenbrunner, H. Jinno, N. Matsuhisa, H. Kitanosako, Y. Tachibana, W. Yukita, M. Koizumi, and T. Someya, “Ultraflexible organic photonic skin,” *Science Advances* **2**, p. e1501856, Apr. 2016.
- [89] M. Kaltenbrunner, M. S. White, E. D. Glowacki, T. Sekitani, T. Someya, N. S. Sariciftci, and S. Bauer, “Ultrathin and lightweight organic solar cells with high flexibility,” *Nature Communications* **3**, pp. 1–7, Apr. 2012.
- [90] M. S. White, M. Kaltenbrunner, E. D. Glowacki, K. Gutnichenko, G. Kettlgruber, I. Graz, S. Aazou, C. Ulbricht, D. A. M. Egbe, M. C. Miron, Z. Major, M. C. Scharber, T. Sekitani, T. Someya, S. Bauer, and N. S. Sariciftci, “Ultrathin, highly flexible and stretchable PLEDs,” *Nature Photonics* **7**, pp. 811–816, Oct. 2013.
- [91] R. H. Kim, H. J. Kim, I. Bae, S. K. Hwang, D. B. Velusamy, S. M. Cho, K. Takaishi, T. Muto, D. Hashizume, M. Uchiyama, P. André, F. Mathevet, B. Heinrich, T. Aoyama, D.-E. Kim, H. Lee, J.-C. Ribierre, and C. Park, “Non-volatile organic memory with sub-millimetre bending radius,” *Nature Communications* **5**, pp. 1–12, Apr. 2014.
- [92] T. Someya, Y. Kato, T. Sekitani, S. Iba, Y. Noguchi, Y. Murase, H. Kawaguchi, and T. Sakurai, “Conformable, flexible, large-area networks of pressure and thermal sensors with organic transistor active matrixes,” *Proceedings of the National Academy of Sciences* **102**, pp. 12321–12325, Aug. 2005.
- [93] T. Someya, T. Sekitani, S. Iba, Y. Kato, H. Kawaguchi, and T. Sakurai, “A large-area, flexible pressure sensor matrix with organic field-effect

- transistors for artificial skin applications,” *Proceedings of the National Academy of Sciences* **101**, pp. 9966–9970, July 2004.
- [94] J. A. Rogers and Y. Huang, “A curvy, stretchy future for electronics,” *Proceedings of the National Academy of Sciences* **106**, pp. 10875–10876, July 2009.
- [95] P. R. Resnick and W. H. Buck, “Teflon® AF: A Family of Amorphous Fluoropolymers with Extraordinary Properties,” in *Fluoropolymers 2: Properties*, G. Hougham, P. E. Cassidy, K. Johns, and T. Davidson, eds., *Topics in Applied Chemistry*, pp. 25–33, Springer US, Boston, MA, 1999.
- [96] C.-J. Yang and S. A. Jenekhe, “Group Contribution to Molar Refraction and Refractive Index of Conjugated Polymers,” *Chemistry of Materials* **7**, pp. 1276–1285, July 1995.
- [97] E. K. Macdonald, J. C. Lacey, I. Ogura, and M. P. Shaver, “Aromatic polyphosphonates as high refractive index polymers,” *European Polymer Journal* **87**, pp. 14–23, Feb. 2017.
- [98] E. K. Macdonald and M. P. Shaver, “Intrinsic high refractive index polymers,” *Polymer International* **64**(1), pp. 6–14, 2015.
- [99] A. Yeniay, R. Gao, K. Takayama, R. Gao, and A. Garito, “Ultra-low-loss polymer waveguides,” *Journal of Lightwave Technology* **22**, pp. 154–158, Jan. 2004.
- [100] M.-C. Oh, H.-J. Lee, M.-H. Lee, J.-H. Ahn, S. G. Han, and H.-G. Kim, “Tunable wavelength filters with Bragg gratings in polymer waveguides,” *Applied Physics Letters* **73**, pp. 2543–2545, Nov. 1998.
- [101] K.-J. Kim, J.-W. Kim, M.-C. Oh, Y.-O. Noh, and H.-J. Lee, “Flexible polymer waveguide tunable lasers,” *Optics Express* **18**, pp. 8392–8399, Apr. 2010.

- [102] T. Higashihara and M. Ueda, “Recent Progress in High Refractive Index Polymers,” *Macromolecules* **48**, pp. 1915–1929, Apr. 2015.
- [103] B. Agnarsson, J. Halldorsson, N. Arnfinnsdottir, S. Ingthorsson, T. Gudjonsson, and K. Leosson, “Fabrication of planar polymer waveguides for evanescent-wave sensing in aqueous environments,” *Micro-electronic Engineering* **87**, pp. 56–61, Jan. 2010.
- [104] V. Venkatraman and B. K. Alsberg, “Designing High-Refractive Index Polymers Using Materials Informatics,” *Polymers* **10**, p. 103, Jan. 2018.
- [105] A. J. Heeger, S. Kivelson, J. R. Schrieffer, and W. P. Su, “Solitons in conducting polymers,” *Reviews of Modern Physics* **60**, pp. 781–850, July 1988.
- [106] Thompson J. M. T. and Cacialli Franco, “Organic semiconductors for the new millennium,” *Philosophical Transactions of the Royal Society of London. Series A: Mathematical, Physical and Engineering Sciences* **358**, pp. 173–192, Jan. 2000.
- [107] N. Karl, “Introduction,” in *Organic Electronic Materials: Conjugated Polymers and Low Molecular Weight Organic Solids*, R. Farchioni and G. Grosso, eds., *Springer Series in Materials Science*, pp. 215–239, Springer, Berlin, Heidelberg, Berlin, Heidelberg, 2001.
- [108] A. Pron and P. Rannou, “Processible conjugated polymers: from organic semiconductors to organic metals and superconductors,” *Progress in Polymer Science* **27**, pp. 135–190, Feb. 2002.
- [109] H. A. M. van Mullekom, J. A. J. M. Vekemans, E. E. Havinga, and E. W. Meijer, “Developments in the chemistry and band gap engineering of donor-acceptor substituted conjugated polymers,” *Materials Science and Engineering: R: Reports* **32**, pp. 1–40, Feb. 2001.

- [110] J. L. Brédas, “Relationship between band gap and bond length alternation in organic conjugated polymers,” *The Journal of Chemical Physics* **82**, pp. 3808–3811, Apr. 1985.
- [111] M. Kertesz, C. H. Choi, and S. Yang, “Conjugated Polymers and Aromaticity,” *Chemical Reviews* **105**, pp. 3448–3481, Oct. 2005.
- [112] J. Roncali, “Synthetic Principles for Bandgap Control in Linear p-Conjugated Systems,” *Chemical Reviews* **97**, pp. 173–206, Feb. 1997.
- [113] S. Yang, P. Olishevski, and M. Kertesz, “Bandgap calculations for conjugated polymers,” *Synthetic Metals* **141**, pp. 171–177, Mar. 2004.
- [114] B. Tian, G. Zerbi, and K. Müllen, “Electronic and structural properties of polyparaphenylenevinylene from the vibrational spectra,” *The Journal of Chemical Physics* **95**, pp. 3198–3207, Sept. 1991.
- [115] M. Fox, *Optical Properties of Solids*, Oxford University Press, 2010.
- [116] V. Hernandez, C. Castiglioni, M. Del Zoppo, and G. Zerbi, “Confinement potential and pi-electron delocalization in polyconjugated organic materials,” *Physical Review B* **50**, pp. 9815–9823, Oct. 1994.
- [117] F. Hide, M. A. Díaz-García, B. J. Schwartz, and A. J. Heeger, “New Developments in the Photonic Applications of Conjugated Polymers,” *Accounts of Chemical Research* **30**, pp. 430–436, Oct. 1997.
- [118] M. D. McGehee and A. J. Heeger, “Semiconducting (Conjugated) Polymers as Materials for Solid-State Lasers,” *Advanced Materials* **12**, pp. 1655–1668, Nov. 2000.
- [119] J.-M. Nunzi, “Organic photovoltaic materials and devices,” *Comptes Rendus Physique* **3**, pp. 523–542, Jan. 2002.

- [120] N. C. Greenham, I. D. W. Samuel, G. R. Hayes, R. T. Phillips, Y. A. R. R. Kessener, S. C. Moratti, A. B. Holmes, and R. H. Friend, “Measurement of absolute photoluminescence quantum efficiencies in conjugated polymers,” *Chemical Physics Letters* **241**, pp. 89–96, July 1995.
- [121] I. D. W. Samuel, G. Rumbles, and C. J. Collison, “Efficient inter-chain photoluminescence in a high-electron-affinity conjugated polymer,” *Physical Review B* **52**, pp. R11573–R11576, Oct. 1995.
- [122] A. François, N. Riesen, H. Ji, S. Afshar V., and T. M. Monro, “Polymer based whispering gallery mode laser for biosensing applications,” *Applied Physics Letters* **106**, p. 031104, Jan. 2015.
- [123] U. Brackmann, *Lambdachrome Laser Dyes*. Lambda Physik AG, 3rd ed., Jan. 2000.
- [124] T. Reynolds, N. Riesen, A. Meldrum, X. Fan, J. M. M. Hall, T. M. Monro, and A. François, “Fluorescent and lasing whispering gallery mode microresonators for sensing applications,” *Laser & Photonics Reviews* **11**, p. 1600265, Mar. 2017.
- [125] M.-L. Zheng, W.-Q. Chen, C.-F. Li, X.-Z. Dong, and X.-M. Duan, “Optical Gain Enhancement Using a Carbosiloxane Dendrimer in Dilute Solution of Rhodamine B,” *ChemPhysChem* **8**, pp. 810–814, Apr. 2007.
- [126] A. J. C. Kuehne and M. C. Gather, “Organic Lasers: Recent Developments on Materials, Device Geometries, and Fabrication Techniques,” *Chemical Reviews* **116**, pp. 12823–12864, Nov. 2016.
- [127] K. H. Drexhage, “Structure and Properties of Laser Dyes,” in *Dye Lasers*, F. P. Schäfer, ed., *Topics in Applied Physics* **1**, p. 50, Springer, Berlin, Heidelberg, 1973.

- [128] R. F. Kubin and A. N. Fletcher, "Fluorescence quantum yields of some rhodamine dyes," *Journal of Luminescence* **27**, pp. 455–462, Dec. 1982.
- [129] G. Jones, W. R. Jackson, C. Y. Choi, and W. R. Bergmark, "Solvent effects on emission yield and lifetime for coumarin laser dyes. Requirements for a rotatory decay mechanism," *The Journal of Physical Chemistry* **89**, pp. 294–300, Jan. 1985.
- [130] "Fluorophores," in *Principles of Fluorescence Spectroscopy*, J. R. Lakowicz, ed., pp. 63–95, Springer US, Boston, MA, 2006.
- [131] F. Vogelbacher, X. Zhou, J. Huang, M. Li, K.-J. Jiang, Y. Song, K. Unterrainer, and R. Hainberger, "Material gain concentration quenching in organic dye-doped polymer thin films," *Optical Materials Express* **9**, pp. 1208–1222, Mar. 2019.
- [132] A. P. Green and A. R. Buckley, "Solid state concentration quenching of organic fluorophores in PMMA," *Physical Chemistry Chemical Physics* **17**(2), pp. 1435–1440, 2015.
- [133] A. M. Taleb, B. T. Chiad, and Z. S. Sadik, "Spectroscopic study of DCM as an active medium for luminescent solar concentrators," *Renewable Energy* **30**, pp. 393–398, Mar. 2005.
- [134] C.-T. Chen, "Evolution of Red Organic Light-Emitting Diodes: Materials and Devices," *Chemistry of Materials* **16**, pp. 4389–4400, Nov. 2004.
- [135] B. L. Van Duuren, "Effects of the Environment on the Fluorescence of Aromatic Compounds in Solution," *Chemical Reviews* **63**, pp. 325–354, Aug. 1963.
- [136] J. Huang, V. Bekiari, P. Lianos, and S. Couris, "Study of poly(methyl methacrylate) thin films doped with laser dyes," *Journal of Luminescence* **81**, pp. 285–291, June 1999.

- [137] “Quenching of Fluorescence,” in *Principles of Fluorescence Spectroscopy*, J. R. Lakowicz, ed., pp. 277–330, Springer US, Boston, MA, 2006.
- [138] I. B. Berlman, “General Information,” in *Handbook of Fluorescence Spectra of Aromatic Molecules*, pp. 47–66, Elsevier, 1971.
- [139] H. Rabbani-Haghighi, S. Forget, S. Chénais, A. Siove, M.-C. Castex, and E. Ishow, “Laser operation in nondoped thin films made of a small-molecule organic red-emitter,” *Applied Physics Letters* **95**, p. 033305, July 2009.
- [140] A. Penzkofer and Y. Lu, “Fluorescence quenching of rhodamine 6G in methanol at high concentration,” *Chemical physics* **103**, pp. 399–405, Apr. 1986.
- [141] F. Hide, B. J. Schwartz, M. A. Díaz-García, and A. J. Heeger, “Conjugated polymers as solid-state laser materials,” *Synthetic Metals* **91**, pp. 35–40, Dec. 1997.
- [142] J.-H. Hsu, W. Fann, P.-H. Tsao, K.-R. Chuang, and S.-A. Chen, “Fluorescence from Conjugated Polymer Aggregates in Dilute Poor Solution,” *The Journal of Physical Chemistry A* **103**, pp. 2375–2380, Apr. 1999.
- [143] D. T. McQuade, J. Kim, and T. M. Swager, “Two-Dimensional Conjugated Polymer Assemblies: Interchain Spacing for Control of Photophysics,” *Journal of the American Chemical Society* **122**, pp. 5885–5886, June 2000.
- [144] D. Beljonne, Z. Shuai, G. Pourtois, and J. L. Bredas, “Spin-Orbit Coupling and Intersystem Crossing in Conjugated Polymers: A Configuration Interaction Description,” *The Journal of Physical Chemistry A* **105**, pp. 3899–3907, Apr. 2001.

- [145] C. M. Marian, "Spin-orbit coupling and intersystem crossing in molecules," *Wiley Interdisciplinary Reviews: Computational Molecular Science* **2**(2), pp. 187–203, 2012.
- [146] A. A. Abdel-Shafi and D. R. Worrall, "Mechanism of the excited singlet and triplet states quenching by molecular oxygen in acetonitrile," *Journal of Photochemistry and Photobiology A: Chemistry* **172**, pp. 170–179, May 2005.
- [147] N. Notsuka, H. Nakanotani, H. Noda, K. Goushi, and C. Adachi, "Observation of Nonradiative Deactivation Behavior from Singlet and Triplet States of Thermally Activated Delayed Fluorescence Emitters in Solution," *The Journal of Physical Chemistry Letters* **11**, pp. 562–566, Jan. 2020. Publisher: American Chemical Society.
- [148] R. Schmidt, "Photosensitized Generation of Singlet Oxygen," *Photochemistry and Photobiology* **82**(5), pp. 1161–1177, 2006.
- [149] "Mechanisms and Dynamics of Fluorescence Quenching," in *Principles of Fluorescence Spectroscopy*, J. R. Lakowicz, ed., pp. 331–351, Springer US, Boston, MA, 2006.
- [150] J. U. Kim, I. S. Park, C.-Y. Chan, M. Tanaka, Y. Tsuchiya, H. Nakanotani, and C. Adachi, "Nanosecond-time-scale delayed fluorescence molecule for deep-blue OLEDs with small efficiency rolloff," *Nature Communications* **11**, p. 1765, Apr. 2020.
- [151] R. Zondervan, F. Kulzer, M. A. Kol'chenk, and M. Orrit, "Photobleaching of Rhodamine 6G in Poly(vinyl alcohol) at the Ensemble and Single-Molecule Levels," *The Journal of Physical Chemistry A* **108**, pp. 1657–1665, Mar. 2004.
- [152] R. F. Bianchi, D. T. Balogh, M. Tinani, R. M. Faria, and E. A. Irene, "Ellipsometry study of the photo-oxidation of poly[(2-methoxy-5-

- hexyloxy)-p-phenylenevinylene],” *Journal of Polymer Science Part B: Polymer Physics* **42**, pp. 1033–1041, Mar. 2004.
- [153] X. Fan and S.-H. Yun, “The potential of optofluidic biolasers,” *Nature Methods* **11**, pp. 141–147, Feb. 2014.
- [154] M. Humar and S. H. Yun, “Intracellular microlasers,” *Nature Photonics* **9**, pp. 572–576, Sept. 2015.
- [155] Y.-C. Chen and X. Fan, “Biological Lasers for Biomedical Applications,” *Advanced Optical Materials* **7**, p. 1900377, June 2019.
- [156] A. François, H. Schwefel, and T. M. Monro, “Using the lasing threshold in whispering gallery mode resonators for refractive index sensing,” in *Laser Resonators, Microresonators, and Beam Control XX*, **10518**, pp. 89 – 93, International Society for Optics and Photonics, Feb. 2018.
- [157] C.-Y. Chao and L. Guo, “Design and optimization of microring resonators in biochemical sensing applications,” *Journal of Lightwave Technology* **24**, pp. 1395–1402, Mar. 2006.
- [158] S. K. Y. Tang, Z. Li, A. R. Abate, J. J. Agresti, D. A. Weitz, D. Psaltis, and G. M. Whitesides, “A multi-color fast-switching microfluidic droplet dye laser,” *Lab on a Chip* **9**, pp. 2767–2771, Oct. 2009.
- [159] H. Wang, Y. Xu, X. Yu, R. Xing, J. Liu, and Y. Han, “Structure and Morphology Control in Thin Films of Conjugated Polymers for an Improved Charge Transport,” *Polymers* **5**, pp. 1272–1324, Dec. 2013.
- [160] S. Kushida, D. Okada, F. Sasaki, Z.-H. Lin, J.-S. Huang, and Y. Yamamoto, “Low-Threshold Whispering Gallery Mode Lasing from Self-Assembled Microspheres of Single-Sort Conjugated Polymers,” *Advanced Optical Materials* **5**, p. 1700123, May 2017.

- [161] P. N. Stavrinou, G. Ryu, M. Campoy-Quiles, and D. D. C. Bradley, “The change in refractive index of poly(9,9-dioctylfluorene) due to the adoption of the β -phase chain conformation,” *Journal of Physics: Condensed Matter* **19**, p. 466107, Oct. 2007. Publisher: IOP Publishing.
- [162] M. Gao, C. Wei, X. Lin, Y. Liu, F. Hu, and Y. Sheng Zhao, “Controlled assembly of organic whispering-gallery-mode microlasers as highly sensitive chemical vapor sensors,” *Chemical Communications* **53**, pp. 3102–3105, Feb. 2017.
- [163] K. Tabata, D. Braam, S. Kushida, L. Tong, J. Kuwabara, T. Kanbara, A. Beckel, A. Lorke, and Y. Yamamoto, “Self-assembled conjugated polymer spheres as fluorescent microresonators,” *Scientific Reports* **4**, pp. 1–5, May 2015.
- [164] N. A. Kuznetsova, O. L. Kaliya, and E. A. Lukyanets, “Photochemistry of laser dyes for the visible spectrum,” **2619**, pp. 161–166, International Society for Optics and Photonics, Aug. 1995.
- [165] B. Smit, P. a. J. Hilbers, K. Esselink, L. a. M. Rupert, N. M. v. Os, and A. G. Schlijper, “Computer simulations of a water/oil interface in the presence of micelles,” *Nature* **348**, pp. 624–625, Dec. 1990.
- [166] M. B. Einarson and J. C. Berg, “Electrosteric Stabilization of Colloidal Latex Dispersions,” *Journal of Colloid and Interface Science* **155**, pp. 165–172, Jan. 1993.
- [167] M. Wulff-Pérez, A. Torcello-Gómez, M. J. Gálvez-Ruíz, and A. Martín-Rodríguez, “Stability of emulsions for parenteral feeding: Preparation and characterization of o/w nanoemulsions with natural oils and Pluronic f68 as surfactant,” *Food Hydrocolloids* **23**, pp. 1096–1102, June 2009.

- [168] I. Aranberri, K. J. Beverley, B. P. Binks, J. H. Clint, and P. D. I. Fletcher, “How Do Emulsions Evaporate?,” *Langmuir* **18**, pp. 3471–3475, Apr. 2002.
- [169] “Solvent miscibility table.” <https://www.sigmaaldrich.com/chemistry/solvents/solvent-miscibility-table.html>.
- [170] H. A. Huckabay and R. C. Dunn, “Whispering gallery mode imaging for the multiplexed detection of biomarkers,” *Sensors and Actuators B: Chemical* **160**, pp. 1262–1267, Dec. 2011.
- [171] A. Weller, F. Liu, R. Dahint, and M. Himmelhaus, “Whispering gallery mode biosensors in the low-Q limit,” *Applied Physics B* **90**, pp. 561–567, Mar. 2008.
- [172] M. D. Baaske, M. R. Foreman, and F. Vollmer, “Single-molecule nucleic acid interactions monitored on a label-free microcavity biosensor platform,” *Nature Nanotechnology* **9**, pp. 933–939, Nov. 2014.
- [173] Y. Zhi, X.-C. Yu, Q. Gong, L. Yang, and Y.-F. Xiao, “Single Nanoparticle Detection Using Optical Microcavities,” *Advanced Materials* **29**, p. 1604920, Jan. 2017.
- [174] T. Reynolds, A. François, N. Riesen, M. E. Turvey, S. J. Nicholls, P. Hoffmann, and T. M. Monro, “Dynamic Self-Referencing Approach to Whispering Gallery Mode Biosensing and Its Application to Measurement within Undiluted Serum,” *Analytical Chemistry* **88**, pp. 4036–4040, Apr. 2016.
- [175] A. François, T. Reynolds, and T. M. Monro, “A Fiber-Tip Label-Free Biological Sensing Platform: A Practical Approach toward In-Vivo Sensing,” *Sensors* **15**, pp. 1168–1181, Jan. 2015.

- [176] K. Sasaki, H. Fujiwara, and H. Masuhara, “Optical manipulation of a lasing microparticle and its application to near-field microspectroscopy,” *Journal of Vacuum Science & Technology B: Microelectronics and Nanometer Structures Processing, Measurement, and Phenomena* **15**, pp. 2786–2790, Nov. 1997.
- [177] Y. Zhi, T. Thiessen, and A. Meldrum, “Silicon quantum dot coated microspheres for microfluidic refractive index sensing,” *JOSA B* **30**, pp. 51–56, Jan. 2013.
- [178] M. Cai, O. Painter, K. J. Vahala, and P. C. Sercel, “Fiber-coupled microsphere laser,” *Optics Letters* **25**, pp. 1430–1432, Oct. 2000.
- [179] J. M. M. Hall, T. Reynolds, M. R. Henderson, N. Riesen, T. M. Monro, and S. Afshar, “Unified theory of whispering gallery multilayer microspheres with single dipole or active layer sources,” *Optics Express* **25**, pp. 6192–6214, Mar. 2017.
- [180] G. Mi, C. Horvath, M. Aktary, and V. Van, “Silicon microring refractometric sensor for atmospheric CO₂ gas monitoring,” *Optics Express* **24**, pp. 1773–1780, Jan. 2016.
- [181] Y. Zhi, J. Valenta, and A. Meldrum, “Structure of whispering gallery mode spectrum of microspheres coated with fluorescent silicon quantum dots,” *JOSA B* **30**, pp. 3079–3085, Nov. 2013.
- [182] S. W. Schmitt, G. Sarau, and S. Christiansen, “Observation of strongly enhanced photoluminescence from inverted cone-shaped silicon nanostructures,” *Scientific Reports* **5**, pp. 1–12, Nov. 2015.
- [183] T. Grossmann, S. Schleede, M. Hauser, M. B. Christiansen, C. Vanahme, C. Eschenbaum, S. Klinkhammer, T. Beck, J. Fuchs, G. U.

- Nienhaus, U. Lemmer, A. Kristensen, T. Mappes, and H. Kalt, “Low-threshold conical microcavity dye lasers,” *Applied Physics Letters* **97**, p. 063304, Aug. 2010.
- [184] X. Cai, J. Wang, M. J. Strain, B. Johnson-Morris, J. Zhu, M. Sorel, J. L. O’Brien, M. G. Thompson, and S. Yu, “Integrated Compact Optical Vortex Beam Emitters,” *Science* **338**, pp. 363–366, Oct. 2012.
- [185] A. P. Porfirev, A. V. Ustinov, and S. N. Khonina, “Polarization conversion when focusing cylindrically polarized vortex beams,” *Scientific Reports* **6**, pp. 1–9, Dec. 2016.
- [186] M. Sumetsky, “Localization of light on a cone: theoretical evidence and experimental demonstration for an optical fiber,” *Optics Letters* **36**, pp. 145–147, Jan. 2011.
- [187] A. Meldrum, P. Bianucci, and F. Marsiglio, “Modification of ensemble emission rates and luminescence spectra for inhomogeneously broadened distributions of quantum dots coupled to optical microcavities,” *Optics Express* **18**, pp. 10230–10246, May 2010.
- [188] M. D. Barnes, W. B. Whitten, S. Arnold, and J. M. Ramsey, “Homogeneous linewidths of Rhodamine 6G at room temperature from cavity-enhanced spontaneous emission rates,” *The Journal of Chemical Physics* **97**, pp. 7842–7845, Nov. 1992.
- [189] E. I. Smotrova, T. M. Benson, P. Sewell, J. Ctyroky, and A. I. Nosich, “Lasing spectra and thresholds of supermodes in an active microdisk assisted with a passive microring in view of the mode overlap coefficients,” in *2008 10th Anniversary International Conference on Transparent Optical Networks*, **4**, pp. 242–245, June 2008.

- [190] P. Féron, “Whispering gallery mode lasers in erbium doped fluoride glasses,” in *Annales de la Fondation Louis de Broglie*, **29**, pp. 317–329, Fondation Louis de Broglie, 2004.
- [191] N. Riesen, T. Reynolds, A. François, M. R. Henderson, and T. M. Monro, “Q-factor limits for far-field detection of whispering gallery modes in active microspheres,” *Optics Express* **23**, pp. 28896–28904, Nov. 2015.
- [192] R. Jakubiak, L. J. Rothberg, W. Wan, and B. R. Hsieh, “Reduction of photoluminescence quantum yield by interchain interactions in conjugated polymer films,” *Synthetic Metals* **101**, pp. 230–233, May 1999.
- [193] L. Hou, S. Adhikari, Y. Tian, I. G. Scheblykin, and M. Orrit, “Absorption and Quantum Yield of Single Conjugated Polymer Poly[2-methoxy-5-(2-ethylhexyloxy)-1,4-phenylenevinylene] (MEH-PPV) Molecules,” *Nano Letters* **17**, pp. 1575–1581, Mar. 2017.
- [194] F. Marchioni, R. Chiechi, S. Patil, F. Wudl, Y. Chen, and J. Shinar, “Absolute photoluminescence quantum yield enhancement of poly(2-methoxy 5-[2'-ethylhexyloxy]-p-phenylenevinylene),” *Applied Physics Letters* **89**, p. 061101, Aug. 2006.
- [195] S. Reineke, “Phosphorescence meets its match,” *Nature Photonics* **8**, pp. 269–270, Apr. 2014.
- [196] S. Reineke, “Complementary LED technologies,” *Nature Materials* **14**, pp. 459–462, May 2015.
- [197] J. H. Burroughes, D. D. C. Bradley, A. R. Brown, R. N. Marks, K. Mackay, R. H. Friend, P. L. Burns, and A. B. Holmes, “Light-emitting diodes based on conjugated polymers,” *Nature* **347**, p. 539, Oct. 1990.

- [198] D. Bondarev, O. Trhlíková, J. Sedláček, and J. Vohlídal, “Stability of MEH-PPV: Poly{[2-methoxy-5-(2-ethylhexyloxy)-1,4-phenylene]vinylene} in solutions exposed to air in the dark and at daylight at laboratory temperature,” *Polymer Degradation and Stability* **110**, pp. 129–136, Dec. 2014.
- [199] G. Gustafsson, Y. Cao, G. M. Treacy, F. Klavetter, N. Colaneri, and A. J. Heeger, “Flexible light-emitting diodes made from soluble conducting polymers,” *Nature* **357**, pp. 477–479, June 1992.
- [200] T. Schwalm, J. Wiesecke, S. Immel, and M. Rehahn, “The Gilch Synthesis of Poly(p-phenylene vinylenes): Mechanistic Knowledge in the Service of Advanced Materials,” *Macromolecular Rapid Communications* **30**(15), pp. 1295–1322, 2009.
- [201] D. Braun and A. J. Heeger, “Visible light emission from semiconducting polymer diodes,” *Applied Physics Letters* **58**, pp. 1982–1984, May 1991.
- [202] N. Tessler, G. J. Denton, and R. H. Friend, “Lasing from conjugated-polymer microcavities,” *Nature* **382**, pp. 695–697, Aug. 1996.
- [203] G. A. Turnbull, T. F. Krauss, W. L. Barnes, and I. D. W. Samuel, “Tuneable distributed feedback lasing in MEH-PPV films,” *Synthetic Metals* **121**, pp. 1757–1758, Mar. 2001.
- [204] W. Holzer, A. Penzkofer, T. Pertsch, N. Danz, A. Bräuer, E. B. Kley, H. Tillmann, C. Bader, and H.-H. Hörhold, “Corrugated neat thin-film conjugated polymer distributed-feedback lasers,” *Applied Physics B* **74**, pp. 333–342, Apr. 2002.
- [205] S. Kushida, D. Braam, T. D. Dao, H. Saito, K. Shibasaki, S. Ishii, T. Nagao, A. Saeki, J. Kuwabara, T. Kanbara, M. Kijima, A. Lorke,

- and Y. Yamamoto, "Conjugated Polymer Blend Microspheres for Efficient, Long-Range Light Energy Transfer," *ACS Nano* **10**, pp. 5543–5549, May 2016.
- [206] J. Wang and K. Wong, "Polarization characteristics of a light-emitting polymer microring laser," *Applied Physics B* **87**, pp. 685–691, June 2007.
- [207] T.-Q. Nguyen, I. B. Martini, J. Liu, and B. J. Schwartz, "Controlling Interchain Interactions in Conjugated Polymers: The Effects of Chain Morphology on Exciton-Exciton Annihilation and Aggregation in MEH-PPV Films," *The Journal of Physical Chemistry B* **104**, pp. 237–255, Jan. 2000.
- [208] A. Boudrioua, P. A. Hobson, B. Matterson, I. D. W. Samuel, and W. L. Barnes, "Birefringence and dispersion of the light emitting polymer MEH-PPV," *Synthetic Metals* **111-112**, pp. 545–547, June 2000.
- [209] K. Gardner, Y. Zhi, L. Tan, S. Lane, Y.-F. Xiao, and A. Meldrum, "Whispering gallery mode structure in polymer-coated lasing microspheres," *JOSA B* **34**, pp. 2140–2146, Oct. 2017.
- [210] C.-H. Dong, L. He, Y.-F. Xiao, V. R. Gaddam, S. K. Ozdemir, Z.-F. Han, G.-C. Guo, and L. Yang, "Fabrication of high-Q polydimethylsiloxane optical microspheres for thermal sensing," *Applied Physics Letters* **94**, p. 231119, June 2009.
- [211] A. Francois and M. Himmelhaus, "Whispering gallery mode biosensor operated in the stimulated emission regime," *Applied Physics Letters* **94**, p. 031101, Jan. 2009.
- [212] V. D. Ta, R. Chen, and H. D. Sun, "Tuning Whispering Gallery Mode Lasing from Self-Assembled Polymer Droplets," *Scientific Reports* **3**, p. 1362, Mar. 2013.

- [213] M. B. J. Diemeer, “Polymeric thermo-optic space switches for optical communications,” *Optical Materials* **9**, pp. 192–200, Jan. 1998.
- [214] Z. Zhang, P. Zhao, P. Lin, and F. Sun, “Thermo-optic coefficients of polymers for optical waveguide applications,” *Polymer* **47**, pp. 4893–4896, June 2006.
- [215] “Fluorescent Microspheres.” <https://www.bangslabs.com/products/fluorescent-microspheres>.
- [216] M. Pelton and Y. Yamamoto, “Ultralow threshold laser using a single quantum dot and a microsphere cavity,” *Physical Review A* **59**, pp. 2418–2421, Mar. 1999.
- [217] Y. Huang, Y. Huang, P. Zhang, and C. Guo, “Ultralow-threshold laser and blue shift cooperative luminescence in a Yb³⁺ doped silica microsphere,” *AIP Advances* **4**, p. 027113, Feb. 2014.
- [218] C. J. Neef and J. P. Ferraris, “MEH-PPV: Improved Synthetic Procedure and Molecular Weight Control,” *Macromolecules* **33**, pp. 2311–2314, Apr. 2000.
- [219] P.-O. Morin, T. Bura, and M. Leclerc, “Realizing the full potential of conjugated polymers: innovation in polymer synthesis,” *Materials Horizons* **3**(1), pp. 11–20, 2016.
- [220] M. S. AlSalhi, J. Alam, L. A. Dass, and M. Raja, “Recent Advances in Conjugated Polymers for Light Emitting Devices,” *International Journal of Molecular Sciences* **12**, pp. 2036–2054, Mar. 2011.
- [221] G. Li, W.-H. Chang, and Y. Yang, “Low-bandgap conjugated polymers enabling solution-processable tandem solar cells,” *Nature Reviews Materials* **2**, pp. 1–13, July 2017.

- [222] B. Lakard, S. Carquigny, O. Segut, T. Patois, and S. Lakard, "Gas Sensors Based on Electrodeposited Polymers," *Metals* **5**, pp. 1371–1386, Sept. 2015.
- [223] F. J.-J. Toublan, S. Boppart, and K. S. Suslick, "Tumor Targeting by Surface-Modified Protein Microspheres," *Journal of the American Chemical Society* **128**, pp. 3472–3473, Mar. 2006.
- [224] Market Reports SKU ID: MMR-13386101.
- [225] A. Reisch and A. S. Klymchenko, "Fluorescent Polymer Nanoparticles Based on Dyes: Seeking Brighter Tools for Bioimaging," *Small* **12**(15), pp. 1968–1992, 2016.
- [226] Bangs Labs, *TechNote 103: Fluorescent/Dyed Microspheres*, Mar. 2013.
- [227] A. J. C. Kuehne, M. C. Gather, and J. Sprakel, "Monodisperse conjugated polymer particles by Suzuki-Miyaura dispersion polymerization," *Nature Communications* **3**, pp. 1–7, Sept. 2012.
- [228] S. Ciftci and A. J. C. Kuehne, "Monodisperse Conjugated Polymer Particles via Heck Coupling - A Kinetic Study to Unravel Particle Formation in Step-Growth Dispersion Polymerization," *Macromolecules* **48**, pp. 8389–8393, Nov. 2015.
- [229] T. Chen, H. Yin, Z.-Q. Chen, G.-F. Zhang, N.-H. Xie, C. Li, W.-L. Gong, B. Z. Tang, and M.-Q. Zhu, "Monodisperse AIE-Active Conjugated Polymer Nanoparticles via Dispersion Polymerization Using Geminal Cross-Coupling of 1,1-Dibromoolefins," *Small* **12**(47), pp. 6547–6552, 2016.
- [230] N. Anwar, T. Willms, B. Grimme, and A. J. C. Kuehne, "Light-Switchable and Monodisperse Conjugated Polymer Particles," *ACS Macro Letters* **2**, pp. 766–769, Sept. 2013.

- [231] J. B. t. Hove, J. Appel, J. M. v. d. Broek, A. J. C. Kuehne, and J. Sprakel, “Conjugated Polymer Shells on Colloidal Templates by Seeded Suzuki-Miyaura Dispersion Polymerization,” *Small* **10**(5), pp. 957–963, 2014.
- [232] S. Kushida, S. Okabe, T. D. Dao, S. Ishii, T. Nagao, A. Saeki, M. Kijima, and Y. Yamamoto, “Self-assembled polycarbazole microspheres as single-component, white-colour resonant photoemitters,” *RSC Advances* **6**, pp. 52854–52857, May 2016.
- [233] K. Gardner, M. Aghajamali, S. Vagin, J. Pille, W. Morrish, J. G. C. Veinot, B. Rieger, and A. Meldrum, “Ultrabright Fluorescent and Lasing Microspheres from a Conjugated Polymer,” *Advanced Functional Materials* **28**, p. 1802759, Aug. 2018.
- [234] D. Baah and T. Floyd-Smith, “Microfluidics for particle synthesis from photocrosslinkable materials,” *Microfluidics and Nanofluidics* **17**, pp. 431–455, Sept. 2014.
- [235] A. J. C. Kuehne and D. A. Weitz, “Highly monodisperse conjugated polymer particles synthesized with drop-based microfluidics,” *Chemical Communications* **47**, pp. 12379–12381, Nov. 2011.
- [236] N. K. Varde and D. W. Pack, “Microspheres for controlled release drug delivery,” *Expert Opinion on Biological Therapy* **4**, pp. 35–51, Jan. 2004.
- [237] H. Sun, H. V. Demir, R. Chen, S. Yang, T. He, V. D. Ta, and Y. Wang, “Reconfigurable Liquid Whispering Gallery Mode Microlasers,” *Scientific Reports* **6**, p. 27200, June 2016.
- [238] J. M. Hughes, P. M. Budd, A. Grieve, P. Dutta, K. Tiede, and J. Lewis, “Highly monodisperse, lanthanide-containing polystyrene nanoparticles

as potential standard reference materials for environmental nano fate analysis,” *Journal of Applied Polymer Science* **132**(24), 2015.

- [239] “Polydispersity - what does it mean for dls and chromatography.” <https://www.materials-talks.com/blog/2017/10/23/polydispersity-what-does-it-mean-for-dls-and-chromatography/>.
- [240] T. Ono, M. Yamada, Y. Suzuki, T. Taniguchi, and M. Seki, “One-step synthesis of spherical/nonspherical polymeric microparticles using non-equilibrium microfluidic droplets,” *RSC Advances* **4**, pp. 13557–13564, Mar. 2014.
- [241] Y.-H. Kim, J.-H. Ahn, D.-C. Shin, and S.-K. Kwon, “Synthesis and characterization of poly(terphenylenevinylene) derivatives containing alkoxy substituents and (or) phenyl pendant group,” *Polymer* **45**, pp. 2525–2532, Apr. 2004.
- [242] K. Matsubara, K. Ueno, and Y. Shibata, “Synthesis and Structures of Nickel Halide Complexes Bearing Mono- and Bis-coordinated N-Heterocyclic Carbene Ligands, Catalyzing Grignard Cross-Coupling Reactions,” *Organometallics* **25**, pp. 3422–3427, July 2006.
- [243] S. Chhatre, A. Ichake, K. Harpale, S. Patil, A. Deshpande, M. More, and P. P. Wadgaonkar, “Phenazine-containing poly(phenylenevinylene): a new polymer with impressive field emission properties,” *Journal of Polymer Research* **25**, p. 61, Mar. 2018.